UNIVERSITY OF CALIFORNIA
RIVERSIDE

First Measurements of Transverse Emittance Reduction in MICE Step IV

A Dissertation submitted in partial satisfaction
of the requirements for the degree of

Doctor of Philosophy

in

Physics

by

Christopher Wells Heidt

December 2017

Dissertation Committee:

Dr. Gail Hanson, Chairperson
Dr. Bill Gary
Dr. Hai-Bo Yu

The Dissertation of Christopher Wells Heidt is approved:

Committee Chairperson

University of California, Riverside

Acknowledgments

I am grateful to my advisor Dr. Gail Hanson, without whose help and support I would not have been provided the opportunity to perform this research.

I would also like to extend my gratitude to the Imperial College MICE group, with a special thanks to Professor Ken Long, who championed my cause to the British home office and kindly invited me into the Imperial College family.

Finally I would like to acknowledge the members of the FZX and νFZX collaborations for emotional support and advise.

To all my friends and family around the world. Thank you for sticking with me through this long and arduous transition. Your unconditional love and support has made this possible. I greatly look forward to over sharing and complaining all about this next great transition in my life.

ABSTRACT OF THE DISSERTATION

First Measurements of Transverse Emittance Reduction in MICE Step IV

by

Christopher Wells Heidt

Doctor of Philosophy, Graduate Program in Physics
University of California, Riverside, December 2017
Dr. Gail Hanson, Chairperson

The Muon Ionization Cooling Experiment (MICE) will provide the first demonstration of emittance reduction in transverse phase space without sacrifice of the longitudinal beam momentum in pure muon beam ($> 99.9\%$). The short lifetime of the muon (2.20 μs) requires the development of new techniques for beam cooling to meet the needs of future muon based research facility, such as the proposed Neutrino Factory and Muon Collider. MICE is a single particle experiment, in that emittance is calculated from an ensemble of single particle measurements as collected by two scintillating fiber trackers located at either end of the MICE cooling channel. Originally purposed as a six step experiment, allowing for systematics of the various components of the experiment to be studied independently, MICE Step IV provides the first opportunity to measure emittance reduction.

Presented here is an introduction to the history of Neutrino physics which serves as a motivation for the development of a high energy muon facility. Chapter 2 outlines some basic principles of accelerator physics leading into Chapter 3, which details the various subsystems that comprise MICE. Chapter 4 is dedicated to a discussion of the MICE Analysis

User Software (MAUS), developed by the experiment to handle the reconstruction of MICE data. The particular focus of this chapter will be on the implementation of the MAUS tracker software and Monte Carlo routines. In the final chapter data from the 2016/04 ISIS User cycle is analyzed. Two different techniques for performing particle identification are discussed and a final figure on total emittance reduction across a LiH absorber is presented.

Contents

List of Figures

List of Tables

Chapter 1

Introduction

1.1 Early Experiments

1.1.1 Discovery of the Neutrino and Muon

The neutrino was first purposed by Pauli in 1930 as a way to account for the spectrum of measured energies in the ejected electron in the charged current weak interaction of a beta decay[1]. In a beta decay it is observed that the atom undergoing decay positively increments its atomic number ($Z \to Z + 1$) which produces an exact change in the atom's mass $m_{(X^A_Z)} - m_{(Y^A_{Z+1})} \equiv m_\beta$. However, in every measurement the energy carried away by the beta electron was less than that of m_β. Pauli posit that this required the presence of a third particle, one whose nature makes it difficult to detect, responsible for carrying away some fraction of the energy in the beta decay. Hence the neutrino was born.

The first experimental observation of the neutrino had to wait 26 years until 1956. That year Frederick Reines and Clyde Cowan, with help from Los Alamos, exploited the

large flux of free anti-neutrinos from the nuclear reactor at the Savannah River Plant. The experiment consisted of two tanks containing a water and cadmium mix, which provided a large cross section for neutron interaction. Surrounding these tanks were three layers of scintillators, designed to detect gamma bursts from inverse beta decay. The detector was isolated from the reactor by a lead wall to prevent contamination from other particles in the reactor. Incident anti-neutrinos interact with the hydrogen in water as:

$$\bar{\nu} + p \rightarrow n + e^{+} \tag{1.1}$$

Positrons freed in this reaction quickly annihilate with electrons in the liquid producing the first gamma signal. The larger mean free path of the neutron compared to the positron causes a delay in the second gamma signal of about 2 μs. Both reactions are read in by the photomultiplier tubes sitting just outside the scintillating liquid. The difference between these two signals is characteristic of anti-neutrino capture. These results are shown in Fig 1.1 [2]

Contemporary to this research, in 1936 Seth Neddermeyer and Carl Anderson made the first observation of the muon[3]. While studying the energy of cosmic rays through a lead layer they noticed that certain penetrating particles had different radius of curvature in a magnetic field, given the same incident velocities. Presented with the necessity of purposing a new particle with a mass between the electron and proton or one with a unique charge to account for this discrepancy, they suggested that the former was the more likely.

The muon, like the electron (and as later discovered, the tau lepton), is a fundamental particle differentiated from the quarks in that they are not subject to the strong

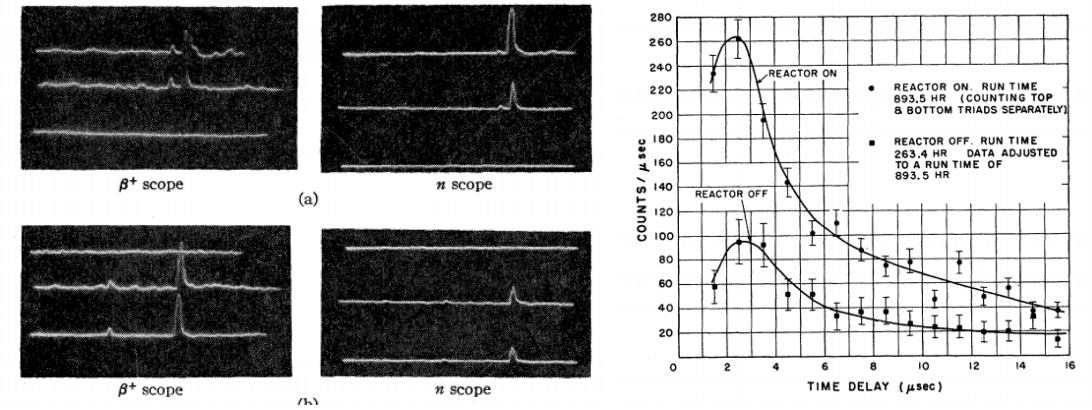

Figure 1.1: (Left) Signal from the Savannah River Experiment showing two events (top and bottom) the positron coincident signal shows up on the β detectors prior to the coincidence in the neutron detector. (Right) Distribution of time delay between coincident signals. [2]

interaction. A fundamental conservation in the weak interaction is that of the lepton flavor (e, μ, τ). Muon lifetime is on the order of $2.20\mu s$, the dominant primary decay of which is:

$$\mu^+ \rightarrow e^+ + \nu_e + \bar{\nu_\mu} \tag{1.2}$$

Similar to Pauli's postulation that the neutrino must exist due to the outgoing energy spectrum of a free electron from a beta decay, measurements of the energy in the released electron after a muon decay indicated the presence of the neutrinos.

Conservation of leptonic flavor and hence the existence of neutrino flavor was shown experimentally at the Brookhaven Alternating Gradient Synchrotron (AGS) in 1962[4]. The AGS provided a source of energetic protons, which when interacted with other hadrons produces pions. The dominate mode of pion decay is:

$$\pi^+ \rightarrow \mu^+ + \nu_\mu \tag{1.3}$$

Thick steel shielding was used to insure nothing but the neutrino produced from the pion decay penetrated to the detector. Should neutrinos be flavorless and flavor is not a conserved quantity then it would be expected that neutrinos passing through the shielding and captured in an inverse beta decay with the material in the detector should produce equal amounts of both muons and electrons. However, of the 29 events detected, all were of the type:

$$\bar{\nu} + p \rightarrow n + \mu^+ \tag{1.4}$$

With the addition of the tau, discovered at SLAC and announced in December of 1975[5], and the corresponding tau neutrino at Fermilab in July of 2000[6], all 12 of the currently known fermions of the Standard Model had been discovered. These fermions comprise three generations of charged leptons paired with the three neutral neutrinos, along with three generations of paired quarks as shown in Table 1.1.

1.1.2 Neutrino Helicity

The helicity of a particle describes the direction of its spin in relation to its momentum. Explicitly this can be written as

$$\mathcal{H} \equiv \frac{\sigma \cdot \mathbf{p}}{|\mathbf{p}|} \tag{1.5}$$

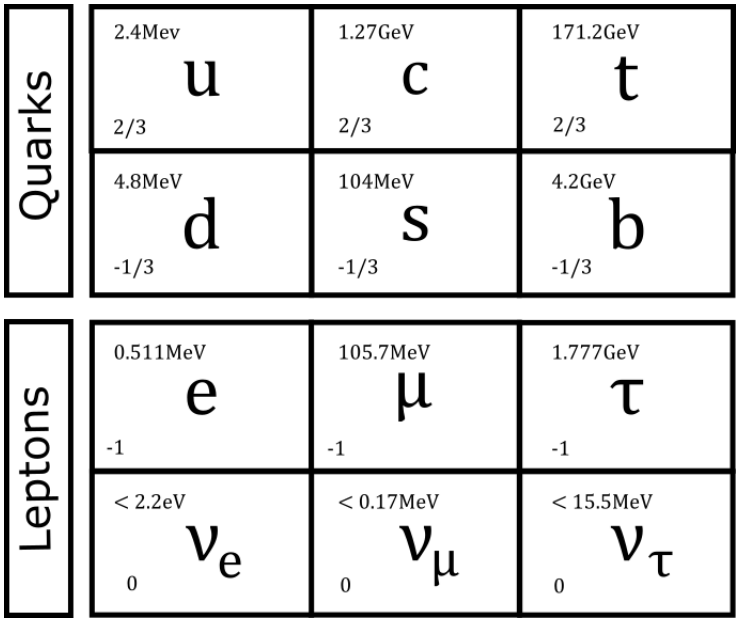

Table 1.1: Fermions of the Standard model. Particles shown with mass (top) and charge (bottom). In addition to what is shown here each particle, with the possible exception of the neutrinos, has an associated anti-particle, bringing the total to 21 or 24 fermions.

where $\boldsymbol{\sigma}$ denotes the particle's spin and p the momentum. Using this system a helicity of +1 corresponds to a right-handed system and as should be expected -1 produces a left-handed system. Helicity however is not an intrinsic quality of a particle. For a massive particle it is always possible to construct a reference frame such that the observer overtakes the observed particle changing the sign of the momentum and thus flipping the helicity. Rather an intrinsic property should be invariant under transformation, and in fact such a quantity can be defined, known as chirality. Chirality is related to helicity in such a way that for a massless particle chirality and helicity are always the same.

While helicity is not an intrinsic characteristic the helical right-handed neutrino (or left-handed anti-neutrino) has not been observed. The neutrino is a chiral left-handed particle in the massless neutrino assumption it would always have a left-handed helicity. However, the neutrino mass is not zero, but the large difference in masses between the neutrino and any other particle means the right-handed helical state is greatly suppressed. In effect the right-handed state is much more prohibited in the case of the neutrino than in other particles.

The first direct measurement of the helicity of the neutrino was carried out in 1957 by Goldhaber, et al. The group studied the decay of Europium into Samarium through orbital electron capture.

$$^{152}Eu + e^{-} \rightarrow ^{152} Sm^{*} + \nu_e \rightarrow ^{152} Sm + \gamma \tag{1.6}$$

The helicity and hence circular polarization of the gamma released from the excited Sm nucleus, using nothing more than conservation of angular momentum, should be identical

to that of the escaping neutrino. Experimentally the group expected that a polarization rate of 75% corresponded to 100% of neutrinos sharing the same helicity. What they found was a $68 \pm 14\%$ of incident gammas had a helicity of -1[7].

1.1.3 Neutrino Mixing

In 1968 Raymond Davis Jr., Don Harmer, and Kenneth Hoffman published their results on the first experimental results in the search for neutrinos originating from the sun. The Homestake experiment involved a 390,000 liter tank filled with tetrachloroethylene (C_2Cl_4) placed 4400m underground at the Homestake gold mine in Lead, South Dakota. Neutrino capture, in the form of inverse beta decay,

$$Cl^{37} + \nu_e \rightarrow Ar^{37} + e^- \tag{1.7}$$

occurs at 5.15 MeV above the Cl^{37} ground state which corresponds primarily to the predicted energy spectra of beta decaying boron atoms from the stellar interior.

It was expected that the neutrino cross section flux should produce on the order of 2 to 7 events per day given the experimental setup. Instead, what was found over the initial running period of 35 days, was a mere 11 ± 3 counts, less than .5 events per day[8]. Over a period of 24 years, from 1970 until 1994, the experiment achieved an average rate of 0.478 ± 0.030 captures per day[9] see Fig 1.2. The large difference between the predicted and observed number of solar neutrinos became known as the solar neutrino problem.

Later that same year Gibbov and Pontecorvo proposed a solution in the form of neutrino oscillation similar to that which had been observed in neutral kaon mixing. They proposed that the neutrino leptonic flavor was not conserved, rather the incoming neutrinos

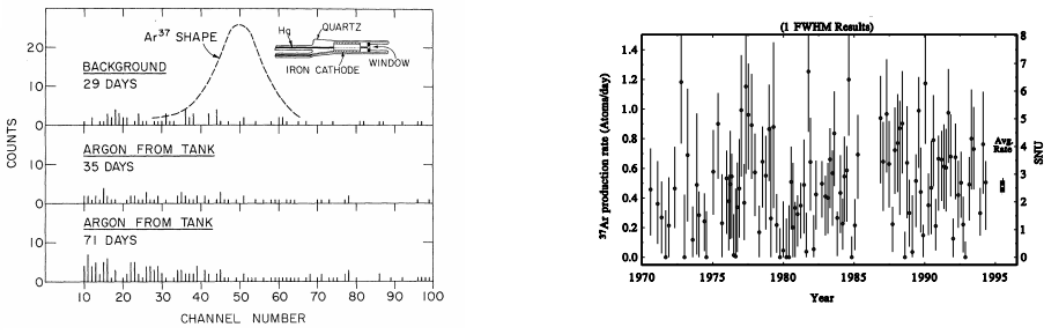

Figure 1.2: (left) Initial results from the Homestake experiment. Ar^37 produced in the inverse beta decay from neutrino capture decays at 2.8 keV, which is selected to be channel 50. Channel 50 and the 14 channels around it are considered events[8]. (right) Capture rates in atoms of Ar^37 per day for all 108 observations at the Homestake experiment from 1970 until 1994[9].

were not missing, but had transformed in flight to a different species of neutrino, which could not be detected by the Davis experiment.

Oscillations are a quantum mechanical effect that arises due to the difference between neutrino flavor and mass eigenstates. The two eigenstates are related through the unitary 3x3 Pontecorvo-Maki-Nakagawa-Sankata (PMNS) matrix[10], which has the form:

$$\begin{bmatrix} \nu_1 \\ \nu_2 \\ \nu_3 \end{bmatrix} = \begin{bmatrix} U_{e1} & U_{\mu 1} & U_{\tau 1} \\ U_{e2} & U_{\mu 2} & U_{\tau 2} \\ U_{e3} & U_{\mu 3} & U_{\tau 3} \end{bmatrix} \begin{bmatrix} \nu_e \\ \nu_\mu \\ \nu_\tau \end{bmatrix} \tag{1.8}$$

The PMNS matrix can be decomposed into four simpler matrices written in terms of three rotation angles θ_{12}, θ_{13}, θ_{23} and three charge parity (CP) violating phases δ, ϕ_2, and ϕ_3:

$$U = \begin{bmatrix} 1 & 0 & 0 \\ 0 & c_{23} & s_{23} \\ 0 & -s_{23} & c_{23} \end{bmatrix} \begin{bmatrix} c_{13} & 0 & s_{13}e^{-i\delta_{CP}} \\ 0 & 1 & 0 \\ -s_{13}e^{-i\delta_{CP}} & 0 & c_{13} \end{bmatrix} \begin{bmatrix} c_{12} & s_{12} & 0 \\ -s_{12} & c_{12} & 0 \\ 0 & 0 & 1 \end{bmatrix} \begin{bmatrix} 1 & 0 & 0 \\ 0 & e^{i\phi_2/2} & 0 \\ 0 & 0 & e^{i\phi_3/2} \end{bmatrix}, \tag{1.9}$$

where c_{ij} and s_{ij} are defined as $\cos(\theta_{ij})$ and $\sin(\theta_{ij})$ respectively. The CP violating variable ϕ_2 and ϕ_3 only take non-zero values in the case where neutrinos are their own particles (Majorana particles). While it is unknown at this time if neutrinos are indeed Majorana particles, and it is an active area of research, the question lies outside the domain of this thesis. Experiments to measure neutrino oscillations are not sensitive to measurements of these phase variables.

Formally writing out the relationship between the mass and flavor eigenstate in bra-ket notation[11]

$$|\nu_\alpha\rangle = \sum_{i,\alpha} U_{\alpha i} |\nu_i\rangle \tag{1.10}$$

where the i subscript denotes mass eigenstates ($i = 1, 2, 3$) and the α denotes flavor eigenstates ($\alpha = e, \mu, \tau$). Explicitly writing out the time and position evolution of the mass eigenstate

$$|\nu_i(x,t)\rangle = e^{ipx - iE_i t} |\nu_i(0,0)\rangle \tag{1.11}$$

Substituting Eq (1.11) into Eq (1.10) yields

$$|\nu_\alpha(x,t)\rangle = \sum_{i,\alpha} U_{\alpha i} e^{i(px - E_i t)} \, |\nu_i(0,0)\rangle \tag{1.12}$$

The amplitude of the initial state α in state β at time t is then given by

$$\langle \nu_\alpha(0,0)|\nu_\beta(x,t)\rangle = \sum_{k,\beta} \sum_{i,\alpha} U^\dagger_{\beta k} U_{\alpha i} e^{-i(px - E_i t)} \, \langle \nu_i(0,0)|\nu_k(0,0)\rangle \tag{1.13}$$

This can be simplified by firstly using the orthogonality of the mass eigenstates, which requires $\langle \nu_k|\nu_i\rangle = \delta_{ik}$. Further, the energy term can be expanded since the mass of the neutrino is minuscule compared to the momentum it carries, so that $E = \sqrt{p^2 + m^2} \approx p + \frac{m^2}{2p} \approx E + \frac{m^2}{2E}$. At some position L away from the neutrino source the probability of finding ν_β in state ν_α is

$$P_{(\nu_\alpha \to \nu_\beta)} = |\sum_{i,\alpha,\beta} U^\dagger_{\beta i} U_{\alpha i} e^{i(\frac{m_i^2}{2E} L)}|^2 \tag{1.14}$$

where the L in the energy dependent term arises from the observation that neutrinos travel at speeds near c. If we consider only the two dimensional case where a neutrino of one flavor is constrained to oscillate into that of another this can be further simplified as [12]

$$P_{(\nu_\alpha \to \nu_\beta)} \approx sin^2(\theta_{ij}) sin^2(1.27 \, \frac{\Delta m_{ij}^2}{2E} L) \tag{1.15}$$

From the above it is clear that it is the dependency on the Δm_{ki} term that necessitates that should neutrinos oscillate, as demonstrated through experimental observation, that neutrinos must posses mass, and further that neutrino mass eigenstates must be split.

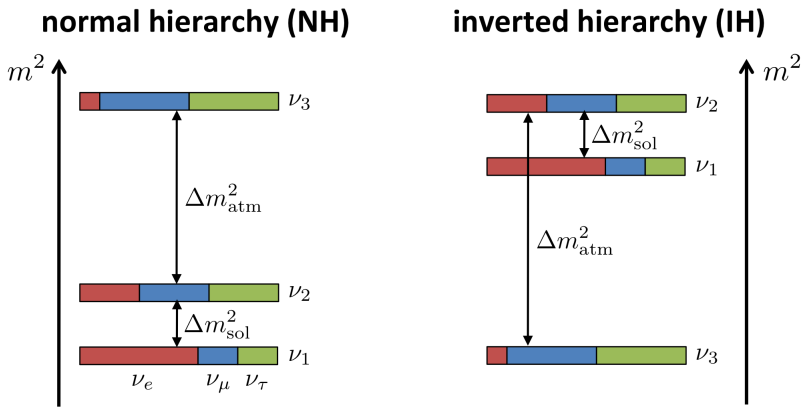

Figure 1.3: Allowable ordering of neutrino mass eigenstates[13]

Neutrino oscillation experiments are sensitive only to the difference of square masses. As a result the solar neutrino mass difference ($|\Delta m^2_{12}|$) and the atmospheric neutrino mass difference ($|\Delta m^2_{23}|$) have been measured, and thereby $|\Delta m^2_{13}|$ since we can expect the relation $\Delta m^2_{12} + \Delta m^2_{23} + \Delta m^2_{31} = 0$. However, the neutrino mass hierarchy and absolute masses remain outstanding problems in neutrino physics. A *Normal* hierarchy models neutrino masses analogous to the quark and lepton sectors with m_1 the lightest followed by m_2 and m_3 respectively. An *Inverted* hierarchy would see m_3 as the lightest mass eigenstate followed by m_1 then m_2. Figure 1.3 illustrates these configurations

The most accurate measurements made of these mass splittings and accompanying mixing angles come from the KamLAND experiment for solar neutrinos and T2K and MINOS for atmospheric neutrinos. While measurements of θ_{13} have been made from the Double Chooz, Daya Bay, and RENO experiments. Table 1.2 list the current best fit neutrino oscillation parameters and the 3σ range as provided by the PDG [14]

Parameter	best-fit	3σ
$\Delta m^2_{12}[10^{-5}eV^2]$	7.37	$6.93 - 7.97$
$\|\Delta m^2\|[10^{-3}\mathrm{eV}^2]$	2.50 (2.46)	2.37 - 2.63 (2.33-2.60)
$\sin^2\theta_{12}$	0.297	0.250 - 0.354
$\sin^2\theta_{23}, \Delta m^2 > 0$	0.437	0.379 - 0.616
$\sin^2\theta_{23}, \Delta m^2 < 0$	0.569	0.383 - 0.637
$\sin^2\theta_{13}, \Delta m^2 > 0$	0.0214	0.0185 - 0.0246
$\sin^2\theta_{23}, \Delta m^2 < 0$	0.0218	0.0186 - 0.0248
δ/π	1.35 (1.32)	(0.92 - 1.99)
		((0.83 - 1.99))

Table 1.2: The best-fit values and 3σ allowed ranges of the 3-neutrino oscillation parameters, derived from a global fit of the current neutrino oscillation data[15]. For the Dirac phase δ the 2σ range is given. Values correspond to NH hypothesis ($m_1 < m_2 < m_3$) values for the IH ($m_3 < m_1 < m_2$) are given in brackets[14]

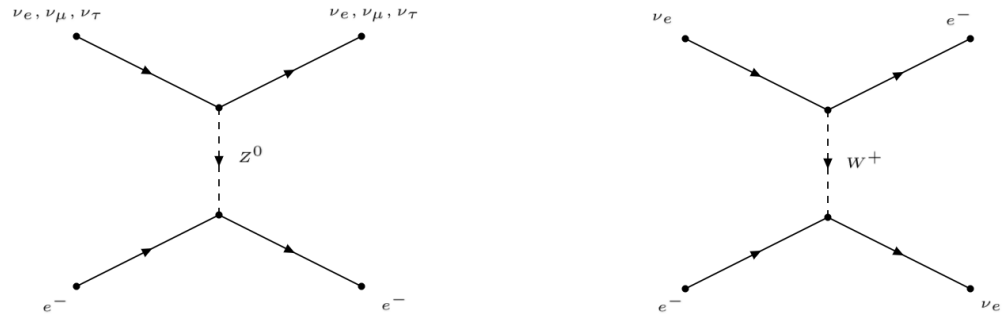

Figure 1.4: (left) Neutrinos of any flavor can interact with electrons in matter they traverse via an exchange of the Z^0 boson. (right) However W^+ exchanges are constrained to ν_e

1.2 New Physics

1.2.1 Mass Hierarchy and δ_{CP}

As discussed in Section 1.1.3 neutrino mixing angles in the absence of matter effects are functions only of the mass squared difference. This is true for neutrinos traversing matter as well; however an asymmetry in effective neutrino masses is introduced. All neutrinos have the ability to interact with surrounding matter via a Z^0 exchange; however, only the ν_e will interact via the charged current W^+ boson. The electroweak potential for the ν_e therefore undergoes a slight shift from that of the other flavor eigenstates (See Fig 1.4). The change in the potential is quantified as:

$$V_e = G_F \sqrt{2} N_e, \tag{1.16}$$

where G_F is the Fermi coupling constant and N_e is the local electron density. This leads to an effective change in ν_e mass relative to the other flavor eigenstates as:

$$\begin{aligned} m^2_{mat} &= (E+V)^2 \approx m^2_{vac} + 2EV_e \\ \Delta m^2 &= 2\sqrt{2} G_F N_e E \end{aligned} \tag{1.17}$$

Carrying out Eq 1.14 to include subleading terms and taking into account the above, we can state the probability of oscillations $P(\nu_\mu \rightarrow \nu_e)$ for neutrinos in matter is expressed as:

$$P(\nu_\mu \rightarrow \nu_e) \approx sin^2\, 2\theta_{13}\, T_1 \; - \; \alpha\, sin\, 2\theta_{13}\, T_2 \; + \; \alpha\, sin\, 2\theta_{13}\, T_3 \; + \; \alpha^4 T_4, \tag{1.18}$$

with the following definitions:

$$\begin{aligned} \alpha &= \frac{\Delta \mathrm{m}^2_{21}}{\Delta \mathrm{m}^2_{31}}, \qquad \Delta = \frac{\Delta \mathrm{m}^2{}_{23} L}{4E}, \qquad A = \frac{2\sqrt{2} e N_e G_F}{\Delta \mathrm{m}^2_{23}} \\ T_1 &= \sin^2\theta_{23} \frac{\sin^2[(1-A)\Delta]}{(1-A^2)}, \\ T_2 &= \sin\delta_{CP}\; \sin 2\theta_{12}\; \sin 2\theta_{23}\; \sin\Delta \frac{\sin(A\Delta)\sin[(1-A)\Delta]}{A(1-A)}, \\ T_3 &= \cos\delta_{CP}\; \sin 2\theta_{12}\; \sin 2\theta_{23}\; \cos\Delta \frac{\sin(A\Delta)\sin[(1-A)\Delta]}{A(1-A)}, \\ T_4 &= \cos^2\theta_{23}\; \sin^2 2\theta_{12} \frac{\sin^2(A\Delta)}{A^2} \end{aligned} \tag{1.19}$$

The sign on the second term of Eq 1.18 changes for antineutrinos, as $\delta_{CP} \rightarrow -\delta_{CP}$. Normal hierarchy is defined then as $\Delta m^2_{23} > 0$ and Inverted $\Delta m^2_{23} < 0$, which also induces a sign flip in the second term. Matter effects therefore allow for measurements of both δ_{CP} and a solution to the neutrino mass hierarchy problem. Currently the search for these parameters is being spearheaded at NOνA while future experiments such as the LBNF will continue to refine the measurements (see Sec 1.3).[16]

1.2.2 Sterile Neutrinos

The Standard Model neutrinos are constrained to interact with matter via the weak and gravitational forces, thus making them very difficult to detect. The hypothetical sterile neutrino, which carries no flavor nor a weak hypercharge, are further even further constrained. Such a particle would only interact with matter gravitationally, with a result that direct detection of would be prohibitively difficult. However, sterile neutrinos could be expected to mix with the other three mass eigenstates as an extending term to Eq 1.8. The signal this would produce could be in the form of anomalous appearance or disappearance of the Standard Model neutrino species beyond what is predicted by known oscillation wavelengths. The first tantalizing hints that additional mass states may exist beyond the three already established first appeared from the Liquid Scintillator Neutrino Detector (LSND) experiment which observed $\bar{\nu}_e$ in a beam of $\bar{\nu}_\mu$ and from the Mini Booster Neutrino Experiment (MiniBooNE), which found an excess of both ν_e and $\bar{\nu}_e$.[17]

One theory as to the nature of these particles has them as the right handed pair of the active neutrinos. As discussed in Section 1.1.2 to date only left handed neutrinos, or right handed antineutrinos have been observed. This is contrary to all other known fermions where both left and right chirality have been observed. The mass difference between the right-handed and left-handed neutrinos arises an alteration to the standard mass matrix in the form an additional massive term. Referred to as the Seesaw Mechanism, the new generalized neutrino mass is[18]:

$$M_{\nu l} = \begin{bmatrix} 0 & m_D \\ m_D & M_{RHN} \end{bmatrix}, \tag{1.20}$$

where:

$$m_{\nu l} << m_D << M_{RHN} \tag{1.21}$$

At high enough energy scales some as of yet undiscovered field is responsible for coupling these terms. This process is described by the eigenvalues of the matrix which produces two solution, one approximately equal to M_{RHN} and:

$$m_{\nu l} \approx \frac{m_D^2}{M_{RHN}}, \tag{1.22}$$

of the Standard Model left-handed neutrino.

The most comprehensive search for a sterile neutrino, was recently completed by the IceCube experiment. After a year long search of cosmic neutrinos the collaboration reported in August 2016 that they had found no evidence of for anomalous ν_μ or $\bar{\nu}_\mu$ disappearance, greatly constraining allowable masses for a sterile neutrino. These results however directly conflict observations from LSND and MiniBooNE. Constraints for sterile neutrino mass from IceCube are shown in Fig 1.5[19].

1.2.3 Neutrinoless Double-β ($\beta\beta_{0\nu}$) Decay

First purposed by Wendell Furry in 1939, $\boldsymbol{\beta\beta_{0\nu}}$ decay would provide direct evidence that the neutrino is a Majorana particle. First purposed in 1937 by Ettore Majorana,

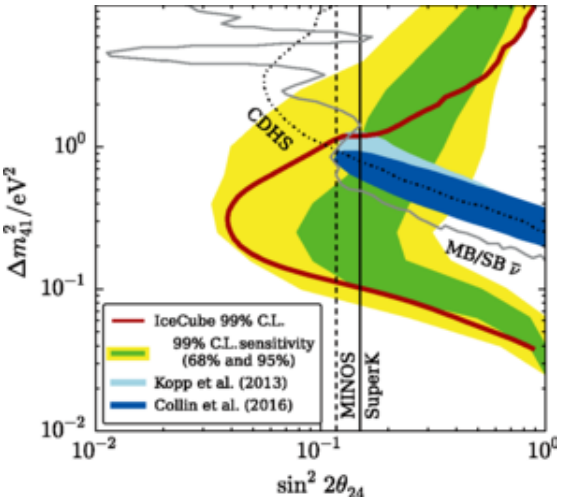

Figure 1.5: Results from IceCube search for sterile neutrinos, the area right of the red line shows the 99% CL exclusion area, data from MiniBooNE and LSND are also included in this figure, represented in the blue shaded area.

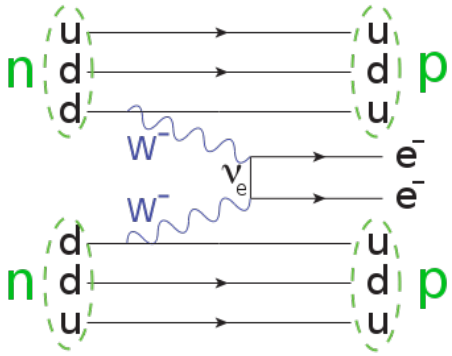

Figure 1.6: The Feynman diagram for $\beta\beta_{0\nu}$ decay, the branching ratio of this reaction is directly proportional to the square of the neutrino mass.[20]

a Majorana particle describes a fermion in which the particle and the antiparticle coincide in a single quantum field, as in the case of the photon[21]. $\beta\beta_{0\nu}$ decay, as depicted in figure 1.6, is described by the reaction:

$$(A, Z) \rightarrow (A, Z + 2) + 2e^{-} \tag{1.23}$$

As well as providing proof of the Majorana nature of the neutrino, experimental confirmation of $\beta\beta_{0\nu}$ decay would be evidence that lepton number is not a symmetry of nature. Study of the $\beta\beta_{0\nu}$ decay rates would also provide a tool for probing the absolute mass of the neutrino. The half life for $\beta\beta_{0\nu}$ decay is given by:

$$\lambda_{0\nu} = |m_{\beta\beta}|^2 |M^{0\nu}|^2 G^{0\nu}, \tag{1.24}$$

where $m_{\beta\beta}$ is:

$$m_{\beta\beta} = \sum_i U_{ei}^2 m_i \tag{1.25}$$

and the other terms (M, G) are worked out in detail in [22].

Experimentally it is challenging to differentiate the 0ν from the 2ν decay. Current searches are underway using measurements of the total kinetic energy from the resultant electrons in either decay. Each process should produce a characteristic energy. The challenge is designing an experiment with sufficient resolution so that it will be possible to separate these two reactions. Isolating the experiment from ionizing radiation background is a significant hurdle, as certain naturally occurring radio-isotopes can mimic the decay signal.

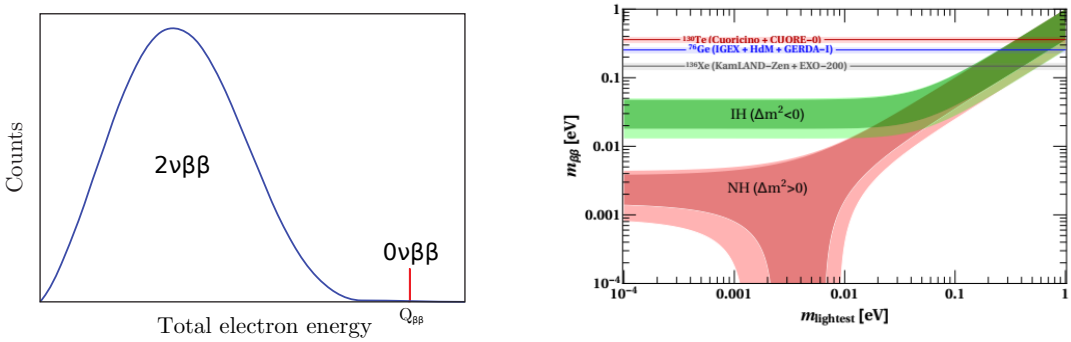

Figure 1.7: (left)Expected distribution in counts between $\beta\beta_{0\nu}$ and $\beta\beta_{2\nu}$ decay channels. (right) Predicted values for $m_{\beta\beta}$ as a function of the lightest neutrino mass within 3σ. The horizontal bands show experimental limits[23].

Additionally all isotopes that can undergo $\beta\beta_{0\nu}$ decays can potentially undergo $\beta\beta_{2\nu}$ decay as well. Energetically similar to the $\beta\beta_{0\nu}$ decay ($t_{1/2} \approx 10^{22-25}$), background from the 2 neutrino reaction ($t_{1/2} \approx 10^{20}$)[24] will overwhelm neutrinoless decay signal at low statistics. Achieving these statistics will require larger and more expensive experiments in the future. Current experimental limits are shown in Fig [23].

1.3 Current Experiments

As shown in eq. 1.15 in the design and placement of a neutrino oscillation experiment there are thee variables to take into consideration: the mass squared differences involved, the ratio L/E, and the neutrino mixing angle. As experimentalists we have direct control over is L/E, the ratio of the distance to the detector to that of the outgoing neutri-

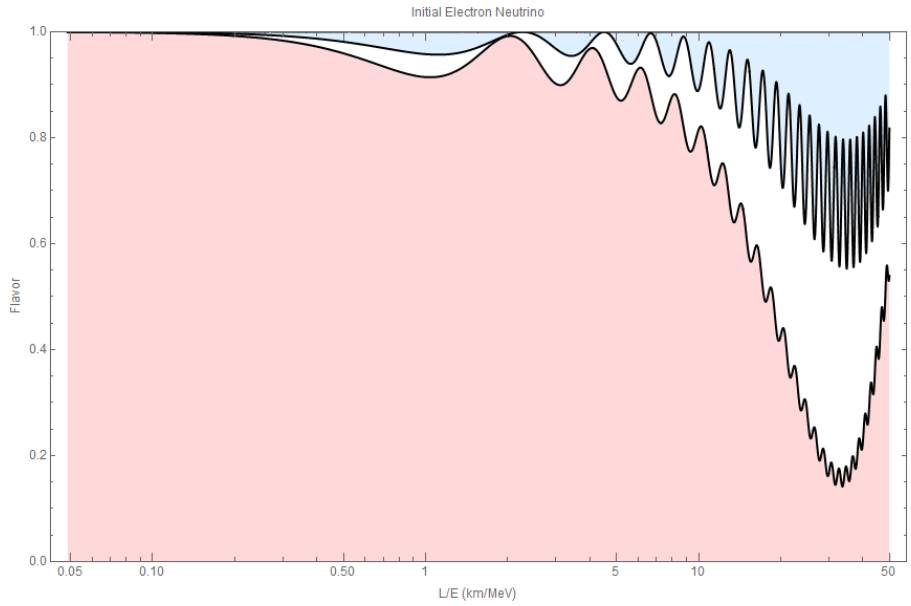

Figure 1.8: Neutrino mixing as a function of L/E for an initially purely e^- beam. The white area shows the fractional population of ν_μ while the blue shaded area ν_τ. Accepted best parameters used[14]. []

nos (see figure 1.8). To maximize the expected neutrino oscillation the detector should be placed such that:

$$L = \frac{E}{2.54\Delta m_{ij}^2}, \tag{1.26}$$

using the values for Δm_{ij} found in Table 1.2 and assuming a 10 MeV beam the expected maximum transmission for a beam of pure ν_e would then be near 33km for the $\nu_e \to \nu_\mu$ transmission and 800m for $\nu_e \to \nu_\tau$. The mixing angle determines the amplitude of the oscillation, with oscillations being maximized for $\theta_{ij} = \frac{\pi}{4}$ corresponding to total conversion

of a beam consisting of species i into that of j. Variance and measurement of incoming particles allows for the determination of Δ_m and θ.

The following is a brief review of three important neutrino experiments of the last 15 years.

KamLAND. Located down a mine shaft in the Japanese Alps near Toyama, Japan, is a liquid scintillator (LS) detector surrounded by 55 commercial nuclear reactors with an average baseline of 180km, KamLAND began data collection in March 2002. The detector consists of 1kt of purified LS contained in a 13m diameter nylon balloon. This detector is surrounded by a cylindrical water-Cherenkov detector, which serves to shield the LS and provides a veto for incident cosmic particles. The signal, from neutrino capture in the form of inverse beta decay, produces a characteristic energy spectrum and time constraints. Coupled with well understood neutrino production rates in nuclear reactors, KamLAND is able to produce highly precise measurements of ν_e oscillations parameters. [25]

Tokai to Kamioka (T2K). A long baseline beam experiment. Protons are accelerated at J-PARC, located near Tokai, Japan, where they collide with a graphite target producing pions and through the decay muon and muon neutrinos. T2K consists of two detectors, the first a near detector located 280m from the target, serves to measure beam direction and intensity. Super K, the far detector located near Kamioka, Japan, is located 295km from J-PARC and 1000m underground. Super K is a 22.5kt water Cerenkov detector, sensitive to differences in muon and electron signal patterns. Since ν_μ and ν_e will tend to produce their respective charged leptonic counterpart in any interaction this serves as evidence of neutrino passage[26].

Daya Bay Centered around 6 nuclear reactors the Daya Bay experiment utilizes 8 anti-neutrino detectors, four of which act as near detectors averaging 500m from the reactors. These detectors provide precision measurement of incoming neutrino flux. The four far detectors located an average of 1100m from the reactors. This configuration puts the far detectors near the expected wavelength of 1MeV atmospheric neutrinos, a local minimum for the survival probability of ν_e[27]. Both the near and far detectors consist of three cylindrical volumes, the innermost layer is 20t of Gd doped LS, which serves as the target. This is surrounded by 21t of un-doped LS for detecting escaping gamma rays. The outside layer is 37t of mineral oil used as a shield for the inner layers. These detectors are then covered with water Cherenkov detectors and muon detectors to veto noise[28]

NuMI Off-Axis ν_e Appearance (NOνA) Utilizes the Neutrinos at the Main Injector (NuMI) project at Fermilab as a 2 GeV neutrino source. NOνA consists of two detectors: a 330 metric-ton near detector located a kilometer from the NuMI source and a much larger 14 kiloton far detector located 14 mrad off axis and 810 km away in Ash River, Minnesota. The 344,064 liquid scintillator and reflective PVC channels of the far detector are arranged into 896 planes in layered orthogonal views to track particles created after a neutrino collision. The stated goals are to measure θ_{13} to high precision, $\delta_C P$, determine the octant of θ_{23}, and mass hierarchy via measurements of differences in the $\nu_\mu \rightarrow \nu_e$ vs $\bar{\nu_\mu} \rightarrow \bar{\nu_e}$ oscillations. Plans are to run for three years in ν mode then switch and run for three years in $\bar{\nu}$ mode. Current best fit measurements from 2017 representing 6.50×10^5 protons-on-target and 33 ν_μ candidates show two degenerate best fit point in the normal hierarchy: $\delta_{CP} = 1.48\pi$ and $sin^2(\theta_{23}) = .404$ or $\delta_{CP} = 0.74\pi$ and $sin^2(\theta_{23}) = .623$. [29][30]

1.4 Neutrino Factory

The current generation of accelerator based neutrino experiments (see Sec 1.3) produce beams from the decay of pions produced by the collision of high energy protons against a target. By the nature of this process the resultant neutrino beam is a spread of a spectrum of energies and positions while introducing uncertainties into the total flux of the beam. The Neutrino Factory(NF), which with its associated muon storage ring, solves this problem by collecting energetic pions and allowing them the time they need to decay and then collating the daughter muons into a well understood beam. This process has several advantages over current generation facilities:

- **Flux** Measurements of muons present in the beam are comparatively easy to make and muon decay is well understood. Muons are constrained to decay into electron/neutrino pairs reducing uncertainty in the total number of particles generated in the neutrino beam.

- **Luminosity** A collimated muon beam will deliver a greater proportion of generated neutrinos to the target. Detectors may also be placed further away from sources as the total angle subtended is reduced. The NF will for ultra long baseline baseline measurements, on the order of 3000km.

- **Energy** Muons may be momentum selected narrowing the energy spectrum of the outgoing neutrino beam producing more precise measurements.

Additionally the NF shares many of the same front end components as the proposed Muon Collider(MuC), which opens up the possibility of preforming lepton anti-lepton

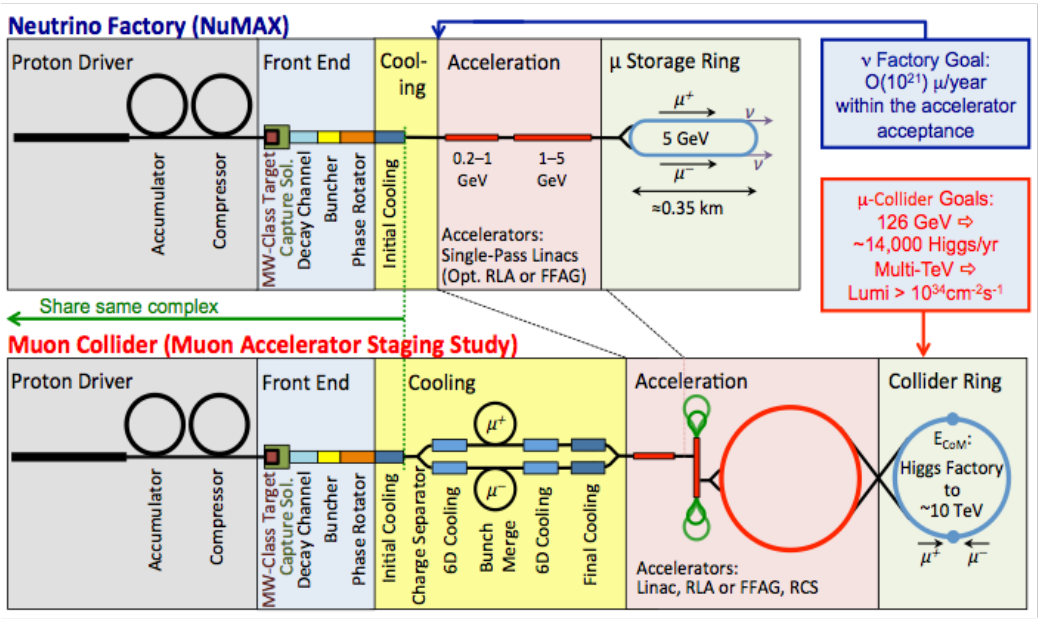

Figure 1.9: Simplified layout of proposed NF and MuC. Both facilities share much of the initial front end requirements only diverging after the initial cooling, shown here with the green dashed line. Beam cooling solutions for both facilities are currently being studied by the MICE collaboration[31]

collisions on the TeV scale. Both the NF and MuC could be built to share many of the same front end facilities (Fig 1.9). This includes the proton driver, decay channel, and initial cooling step. The two facilities diverge after this due to the much more stringent beam cooling requirements of the MuC. Muon beam cooling, defined as the reduction of the muon beam's emittance, or its divergence and dispersion, is studied by the Muon Ionization Cooling Experiment.

The following discussion on the specifics of the NF comes largely from the Feasibility Study-II of a Muon-Based Neutrino Source produced by The Neutrino Factory and Muon Collider Collaboration[32].

1.4.1 Proton Driver

Feasibility Study-II suggests two sites for the future proton driver the first of which envisions upgrades to BNL's Alternating Gradient Synchrotron (AGS). Initially off the shelf upgrades would be undertaken to increase the AGS repetition rate from 0.5Hz to 2.5Hz and increase the total proton rate by a factor of 40%. The net effect would be an increase in beam power to a total of 1MW. Once running, future upgrades would be planned with the aim of increasing total beam power up to 4MW. He^- ions would be accelerated through the synchrotron up to energies of 24GeV before being delivered to the target. Feasibility Study-II also proposes a new proton driver could be developed at FNAL with an initial beam power of 1.2MW with possible upgrades to 4MW, and beam energies of 16MW.

In addition to these sources mentioned in the study, the Front End Test Stand (FETS) at RAL is currently in development. A He^- ion source like the other drivers, FETS would replace ISIS's current 0.16MW driver with a 3MW beam at 50Hz and 60mA. The

initial beam would reach ISIS after traveling through a linear accelerator at around an energy of 10MeV[33]. At this range FETS would provide a beam capable of powering the NF.

1.4.2 Target

A novel free Hg jet target solution was envisioned for dealing with the large amount of heating imparted by a 4MW beam while meeting the requirement for high proton cross section to maximize pion production. Intense internal pressure waves produced by the interactions with the proton beam, which blow the jets apart, require the jets to be free as any piping used to direct the stream would be damaged. The requirement to meet the 50Hz rate of the proton driver additionally requires the jets to be propelled at speeds of 20m/s to clear the collision area before the next interaction.

The whole target apparatus is additionally encased in a superconducting solenoidal field that tapers from 20T down to 1.5T, which is used primarily in capturing and transporting newly produced pions to the decay channel. It also has the effect of increasing the stability of the Hg jets. Data collected from the MERIT experiment demonstrated the viability of this configuration in handling the needs of a 4MW beam[34].

More recently a granular waterfall model has been advanced which may also meet the needs of the NF. Simulation indicates this target configuration should be able to dissipate the heating of beams up to 15MW. The waterfall target chamber surrounds the beam, tungsten granules are dropped across the beam and then collected in a heat exchange before being sent back to the top of the chamber to repeat the cycle[35].

1.4.3 Decay Channel and Bunching

After passing through the target the resultant pions have a large spread in both energy and position. The pions travel through a drift chamber providing the time needed for them to decay to muons while also providing an opportunity for the beam to stretch out longitudinally. The phase rotator uses a series of linacs to effectively exchanging some of the beam's diffusion into momentum. This process speeds up lagging particles while slowing down those traveling more quickly. The buncher then cuts the beam up into smaller bunches though use of RF cavities. After traveling through the NF front end the freshly generated muon beam is directed toward the cooling channel.

1.4.4 Cooling

Beam cooling will be discussed in more detail in section 2.3

1.4.5 Acceleration and Storage Rings

Muons leaving the cooling section need to be rapidly sped up from 130MeV to energies on the GeV scale before entering the muon storage rings. This must be achieved in short order to minimize muon decay. A number of technologies have been purposed, including a series of high powered linacs either in a single pass configuration or a recirculating configuration that would direct muons through the accelerating chambers multiple times. Using a fixed-field alternating-gradient accelerator has also been discussed. Recent results from the EMMA experiment located at the Daresbury Laboratory in the UK has shown promise in the use of this technology[36].

Muons leave the accelerators to the storage rings where the neutrino beams are produced. This section is envisioned as a long race track with the straight sections pointed through the ground at far detectors. The exact distance of the detectors depends of the location selected for the NF, but should be in excess of 3000km. Neutrino beams are produced in the storage rings by providing the time necessary for a muon to decay to its resultant positron and neutrino pairs. Neutrino pass through the ring and continue on to the detector while electrons no longer fit kinematicly into the ring's magnetic lattice and are ejected.

Chapter 2

Accelerator Physics

This chapter will introduce some basic concepts in accelerator physics, particular concern is given over to concepts that directly play a role in MICE. Section 2.1 will cover how magnets are used to maintain and direct a sustainable beam, section 2.2 will discuss how a beam of particle can be defined and finally section 2.3 will discuss the topic of ionization cooling.

2.1 Magnetic Lattice

Magnetic fields are used in circular accelerators as the means to define the path of a beam of charged particles. Three types of magnets are typically used in accelerators these are: dipole, quadrupole, and super conducting solenoid magnets. The strength of these magnets and their placement within the accelerator is often referred as the optics of the beam or accelerator. To the first order the focusing of the beam through a FODO lattice,

comprised of focusing and de-focusing quadrupoles can be thought of as analogous to light moving through converging and diverging lens.

Quadrupole magnets are aligned in accelerators such that the field generated is transverse to the primary axis of the accelerator (Fig. 2.1). A particle traveling through a quadrupole will experience two forces, the first will push the particle toward the magnetic axis in one of the transverse directions, while the second pushes the particle away from the other axis. In this way any focusing of the beam along one axis is offset by a de-focusing of the beam along the other axis, in such a manner that the total spread of the beam is conserved.

The most common way of dealing with this is the FODO lattice which alternates the directions of the fields in successive quadrupole magnets. This can be viewed through the analogy of light traveling through converging and diverging lenses in 2D. When placed at the focal length of converging lens a diverging lens is essentially invisible to the ray traveling through its midpoint. A focal length for a quadrupole can be defined as [37]

$$f = \frac{1}{R\,l}\frac{dB_y}{dx} \tag{2.1}$$

where R is the rigidity of the magnet, given by the product of the radius a particle is deflected through in the magnet and the strength of the magnetic field R = Bρ. Additionally, l is the length of the magnet and dB$_y$/dx is the magnetic gradient of the quadrupole. In such a manner an optical lattice can be designed so that the de-focusing effects in one direction are minimized compared to the focusing effects in the other direction and a stable beam can be constructed.

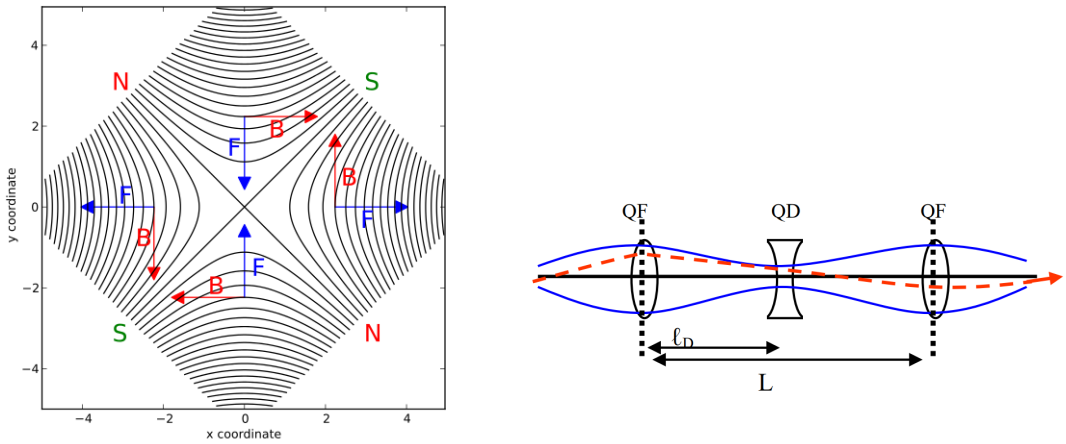

Figure 2.1: (left) Fields of a quadrupole magnet; direction of the force assumes a positive particle traveling into the page. (right) Schematic of simple FODO lattice, the blue line represents the beam envelope while the red line, a single particle trajectory[38].

Dipoles and superconducting coils are primarily used as a means of directing the beam along a circular path. The angle a beam is deflected in a uniform field is given as:

$$\sin\frac{\theta}{2} = \frac{lB}{2R} \tag{2.2}$$

Superconducting coils offer a large advantage over warm temperature dipoles when high magnetic fields are required. Provided the superconducting magnet can be cooled sufficiently, the apparent fact that superconductors do not dissipate the energy of a current provides significant cost savings and larger fields than dipoles.

In MICE dipole magnets and superconducting coils are used for secondary purposes. The large field in the superconducting decay solenoid is used merely to increase the path length of the beam. Both of the dipoles in MICE are used for selecting beam mo-

mentum while the superconducting spectrometer solenoids are used to help make precision measurements of momentum. Both of these make use of the the relation[37]:

$$p = \frac{B\rho}{3.3356}(GeV/c) \tag{2.3}$$

2.2 Defining a Beam

2.2.1 Canonical Definitions

A beam can be simply defined as a collection of particles within a closed contour. In most cases the distribution of particles about the beam axis can be described as an ellipse with a distribution of particles within the ellipse following a Gaussian distribution. In such a beam we define a quantity, emittance, denoted by ϵ, as the spread of the beam in phase space (x, p_x, y, p_y, t, E). In such a way the emittance of a beam encapsulates both the dispersion and divergence of the beam and describes a conserved quantity of the beam governed under Liouville's theorem, which states:

> 'In the vicinity of a particle, the particle density in phase space is constant if the particles move in an external magnetic field or in a general field in which the forces do not depend upon velocity.'

the ramification of which means that as the beam moves through the magnetic lattice of the accelerator the emittance of the beam stays constant.

To help define emittance quantitatively the concept of trace space will be used, in this system:

$$x' = \frac{p_x}{p_z} = \frac{dx}{dz} \tag{2.4}$$

$$y' = \frac{p_y}{p_z} = \frac{dy}{dz} \tag{2.5}$$

Trace space is defined by the vector (x, x′, y, y′, t, E). In this system the emittance is defined as:

$$\epsilon = \frac{1}{\pi} \int u' du = \frac{A}{\pi} \tag{2.6}$$

where u = (x, y ,t) and u′ = (x′, y′, E). The semi-major and semi-minor axis of the ellipse that describes this area in trace space is defined as:

$$u = \sqrt{\epsilon\beta} \tag{2.7}$$

$$u' = \sqrt{\epsilon\gamma} \tag{2.8}$$

where some care needs to be taken, β and γ are not the traditionally defined relativistic quantities, but rather along with the quantity α comprise the beam's Twiss parameters (see Fig 2.2). These values are described by the Courant and Snyder invariant as[37]:

$$\epsilon = \gamma u^2 + 2\alpha u u' + \beta u'^2 \tag{2.9}$$

Emittance defined in this form is not the invariant version that is desired, however. In order to solve for the invariant emittance it is necessary to transform out of the trace space this definition was derived in and back to Hamilton's phase space. This is done by introducing a normalization term dependent on the momentum of the beam.

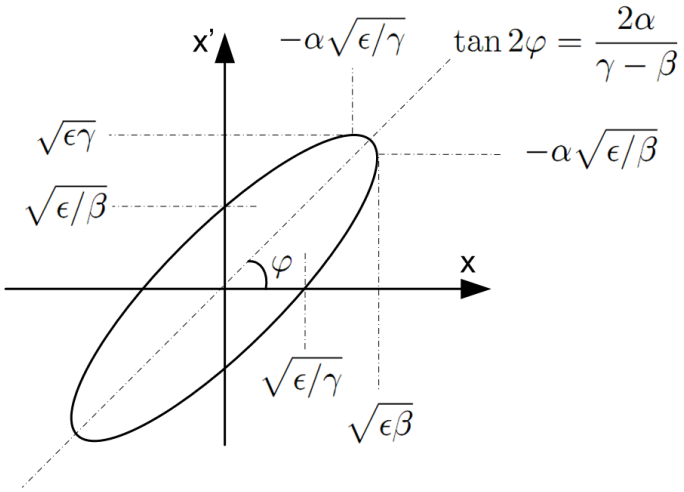

Figure 2.2: Physical meaning of the Twiss parameters as they relate to the beam contour in phase space.

$$\epsilon^* = (\beta\gamma)\epsilon \quad (\pi\ mm\ rad) \tag{2.10}$$

where β and γ here are the normal relativistic terms. This term, ϵ^* referred to as the normalized emittance is the conserved spread of the beam in phase space as given by Liouville's theorem.

2.2.2 MICE Definitions

In MICE the beam parameters are defined using a statistical approach. The area of an N dimensional ellipse of Gaussian distributed points can be described by the analysis of the covariance matrix as [39]:

$$\epsilon = \sqrt[N]{|\mathbf{V}|}, \tag{2.11}$$

where the covariance matrix, $\mathbf{V}$, has elements:

$$v_{ij} =< \sigma_i \sigma_j > - < \sigma_i >< \sigma_j >, \tag{2.12}$$

Using Eq. 2.10, the mass of the particle being studied, and the measured quantities (x, p_x, y, p_y) the normalized traverse emittance is:

$$\epsilon_{\perp}^{*} = \frac{\sqrt[4]{|\mathbf{V}|}}{m}. \tag{2.13}$$

Likewise using (t, E) and (x, p_x, y, p_y, t, E) the longitudinal and 6D emittance are respectively defined as:

$$\epsilon_{\parallel}^{*} = \frac{\sqrt[2]{|\mathbf{V}|}}{m}, \tag{2.14}$$

$$\epsilon^{*} = \frac{\sqrt[6]{|\mathbf{V}|}}{m}. \tag{2.15}$$

For completeness, the MICE beam Twiss parameters are defined as:

$$\beta_{\perp} = \frac{(< xx > + < yy >)p}{2m\epsilon_{\perp}}, \tag{2.16}$$

$$\alpha_{\perp} = \frac{< xp_x > + < yp_y >}{2m\epsilon_{\perp}}, \tag{2.17}$$

$$\gamma_{\perp} = \frac{< p_x p_x > + < p_y p_y >}{2pm\epsilon_{\perp}}. \tag{2.18}$$

2.3 Ionization Cooling

Beam cooling describes a technique to reduce the emittance of a beam. As stated in the previous section, under Liouville's theorem, emittance is a conserved quantity. Liouville's theorem does give us a loophole though: conservation of emittance is violated under a force that depends on the velocity of the beam. Reducing emittance is important for a number of factors, the most basic of which is a beam must actually physically fit in the size of the accelerator aperture! Beyond this, emittance cooling is important in any collider as a machine's luminosity goes as one over the interaction cross section, the tighter the beam, the better. An experiment designed to study neutrino oscillations can also benefit from a low emittance beam. Reduction in the dispersion of the beam will allow the detector to be placed further from the source.

As can be expected, many successful techniques currently exist for cooling a beam. A series of techniques known as stochastic cooling utilizes the individual dispersion of each single particle as it passes through an electrical pickup to drive a kicker further downstream in the beamline. This is done in a way that the signal from the pickup drives the kicker just as the particle travels through the kicker. After a sufficiently long time each particle in the beam develops its own damping force in a sea of much larger forces from the cumulative effect of the beam[40]. Other methods such adiabatic cooling just utilize the natural tendency of rotating particles to emit energy. The thing that all these techniques share is that they involve emittance reduction from motion, as Liouville's theorem requires, and they require more time than is available given the short lifetime of the muon.

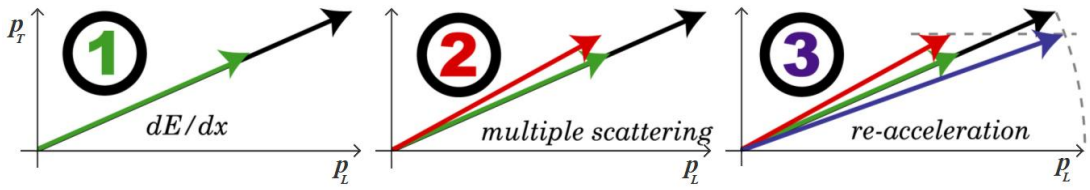

Figure 2.3: The premise of ionization cooling. As a beam crosses through a material (Step 1) ionization creates a uniform reduction in momentum while also (Step 2) increasing the momentum in the transverse direction. The final phase occurs when the beam enters an RF chamber and longitudinal momentum is restored (Step 3).

Ionization cooling offers a way forward for future muon based facilities. As the name implies, ionization from the passage of a particle through a material will exert a retarding force reducing the total momentum of the particle. After passing through the material the beam enters an RF cavity where momentum only along the longitudinal axis is reapplied. A simplified view of this can be seen in figure 2.3. Ionization cooling requires a balancing act, however, as multiple scattering within the material will add energy to the system, effectively heating the beam. The balancing act is described by eq. 2.19, the left hand term in the equation describes the ionization cooling while the right hand term heating via multiple scattering[41].

$$\frac{\epsilon_\perp}{ds} \approx -\frac{\epsilon_\perp}{E_\mu \beta^2} \left\langle \frac{dE}{ds} \right\rangle + \frac{\beta_\perp (13.6MeV)^2}{2\beta^3 E_\mu m_\mu X_0} \tag{2.19}$$

Once again we must be careful: here $\beta_\perp$ describes the beam's Twiss parameter while β is the normal velocity dependent term. Additionally E_μ is the energy of the particle as it enters the absorber, X_0 the radiation length, and dE/ds the average energy lost as per

unit of length. It is clear that to maximize the loss of emittance across the absorber is it important to minimize $\beta_\perp$ at the absorber while maximizing both the X_0 and $\left\langle \frac{dE}{ds} \right\rangle$ terms by selecting the proper absorbing material. MICE will use low-Z absorbers such as liquid hydrogen and lithium hydride to maximize the effect of the cooling term while focusing solenoids will be used as the particle enters the absorber to minimize the heating term.

Chapter 3

The Muon Ionization Cooling Experiment Step IV

3.1 Introduction

The purpose of the Muon Ionization Cooling Experiment (MICE) is to demonstrate the feasibility of ionization cooling in reducing the emittance, or spread, of a muon beam for use in future high energy muon research facilities. The major technical challenges are: overcoming the emittance growth factor of multiple scattering to achieve an overall reduction in emittance, doing this in the presence of high gradient RF fields which are required to restore momentum in the longitudinal direction, and doing this all in a time frame limited by the lifetime of the muon (2.20 μs). The original design envisioned MICE as a test of a single cooling cell, as proposed in the Feasibility Study II of a Muon Based Neutrino Source, of a much larger front end for a Muon Collider or Neutrino Factory.

MICE is a single particle experiment. The emittance measurement is built from a series of individual particle positional measurements as particles travel from one end of the cooling channel to the other. Twin trackers upstream and downstream placed in solenoid fields allow for precision measurement of position and momentum before and after a particle traverses the ionizing material absorber. A study of the absorber's ability to reduce emittance is performed on beams with incoming momenta of 140, 200, and 240 MeV/c and at initial emittances of 3, 6, and 10 π mm rad. Particle identification (PID) detectors located upstream and downstream are used to ensure beam purity below a 1:1,000 ratio. The experiment is located at the Rutherford Appleton Laboratory, UK, off the ISIS proton beamline.

The last few years have seen scaling back from the original goal due to budget considerations. Current design goals are shown in figure 3.1. As the goal of this thesis is the analysis of Step IV emittance data, this chapter will focus on the Step IV design. This includes a discussion of the ISIS beamline from which MICE produces its muon beam (section 3.2), upstream beamline elements (section 3.3), the cooling channel (section 3.4) and the various detectors (section 3.5).

3.2 ISIS

ISIS is an 800MeV proton synchrotron (Fig 3.2). The ISIS beam starts as hydrogen gas mixed with a cesium vapor that is ionized through a discharge plasma and attracted to a cathode surface. From here the H- ions are accelerated through 202.5 MHz, 665 keV RFQs, alternating gradient quadrupoles, which focus and accelerate the low velocity 35keV

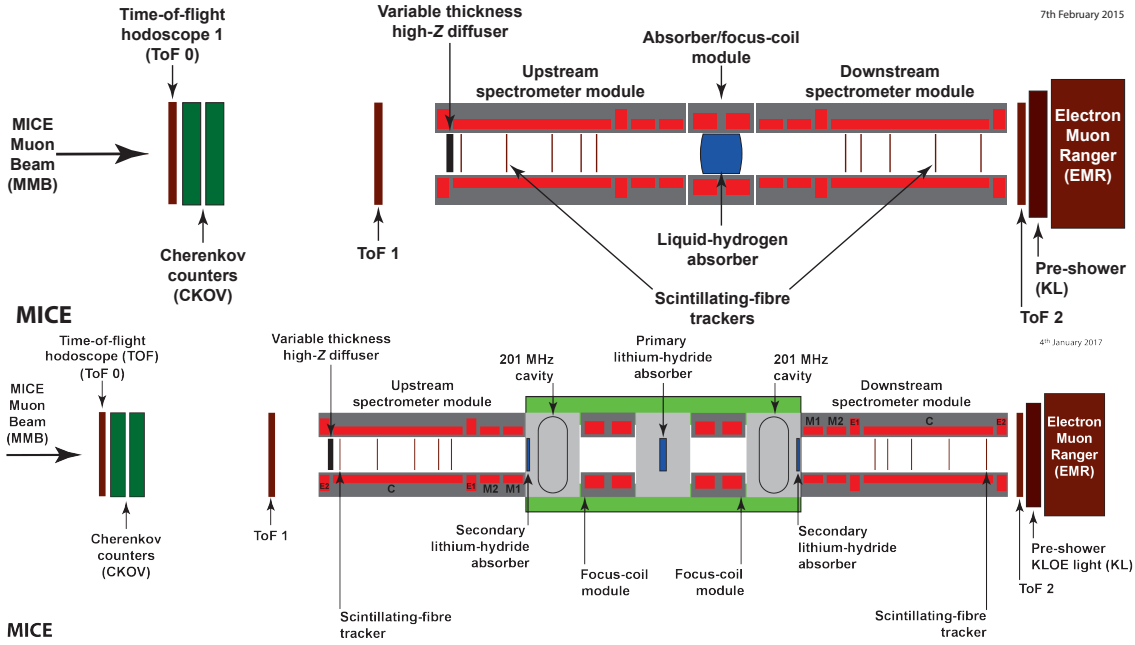

Figure 3.1: (top) the current layout, MICE Step IV and (bottom) the Demonstration of Ionization Cooling the expected final form of MICE.

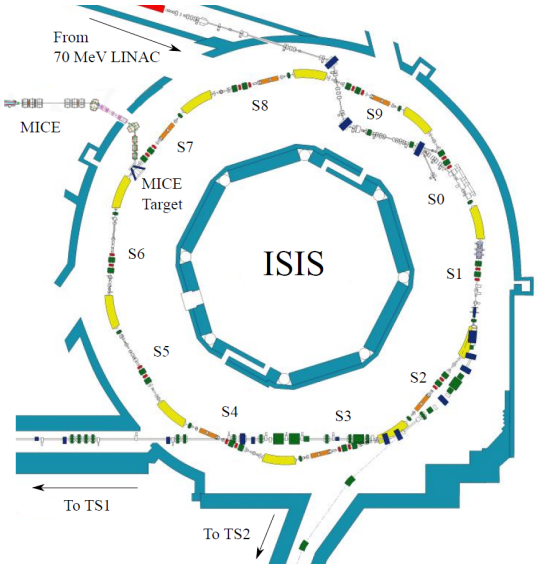

Figure 3.2: The ISIS beamline located at the Rutherford Appleton Laboratory in the UK. The MICE target and beamline are at the top left of the image

ions. Before the beam enters the synchrotron it is accelerated up to 70MeV in the linac which consists of a series of intense RF cavities and drift tubes.

The synchrotron is 52m across, utilizing 10 dipole bending magnets to maintain its circular shape. When the H- ions first enter the synchrotron they traverse a thin aluminum oxide foil to strip off any remaining electrons. Protons are allowed to accumulate over 130 rotations ($2.8\text{x}10^{13}$ protons per bunch or 4 μC) before injecting into a series of six RF cavities in the beamline. These cavities are synced with the changing magnetic field in the dipoles so that a stable beam orbit is maintained and the beam is accelerated to 800MeV over an additional 10,000 rotations. This whole acceleration cycle is repeated 50 times every second[42].

3.3 Beamline

As stated above MICE is located off axis from the ISIS proton beamline. The MICE beamline (see Fig 3.3) begins with the dipping of a titanium target into the ISIS beam and the resultant spray of pions from that collision and ends with a muon beam passing through a diffusing iris and into the cooling channel. Along the way the beam is measured by a host of devices, purged of proton contamination, selected for input momentum, and undergoes a transformation from a beam primarily composed of pions to one primarily of muons. This section will discuss how this is done leaving out only the time of flight (TOF) detectors which will be discussed in section 3.5.

3.3.1 Target

The MICE target is a titanium rod which is inserted directly into the ISIS beam at a rate of 1 Hz or 1 out of every 50 ISIS pulses (Fig 3.4). Because the MICE beam is parasitic to the ISIS beam, the requirements on the target are rather strict. Muons gained by the MICE beam are protons lost by the ISIS beam, and too great of a disruption to the ISIS beam can mean anything from a loss of beam for other ISIS users to a shut down of the beam due to de-coherence of the beam or damage of the facility caused by radiation dispersion. As such the target must be tightly controlled.

The maximum beam radius of the ISIS beam is approximately 67mm; however, by the time it reaches the MICE target that has been focused down to 48mm. The further into the beam the target dips the greater the ISIS beam loss. In order to produce the necessary flux of muons, a beam penetration depth of about 5mm is required, which means the target

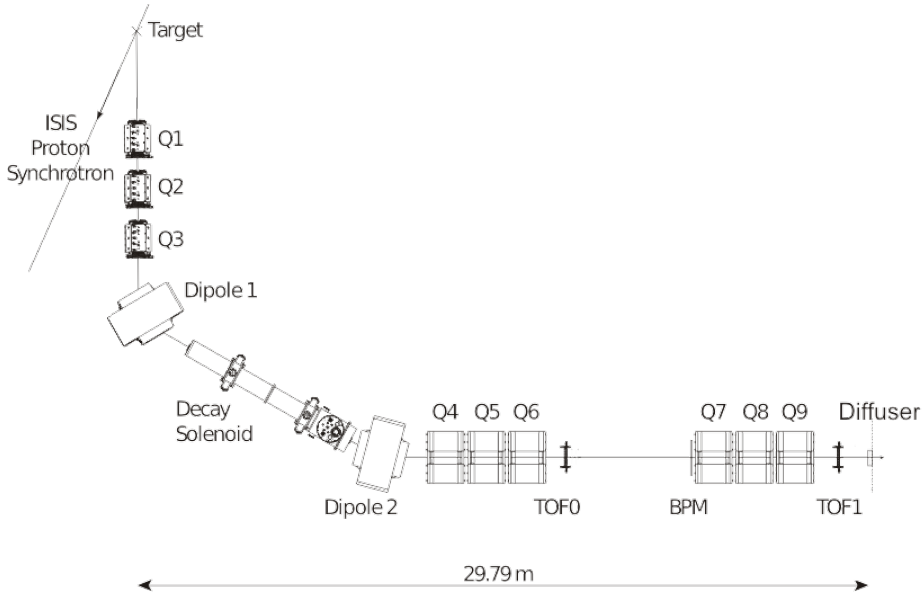

Figure 3.3: The MICE Beamline. Absent from this images is the Luminosity Monitor which placed at the same spot as the first dipole magnet, but reflected about the ISIS beamline and the GVA scintillating counter between the decay solenoid and the second dipole magnet and two beam profile monitors the first upstream of D2 and the second downstream of Q7-9.

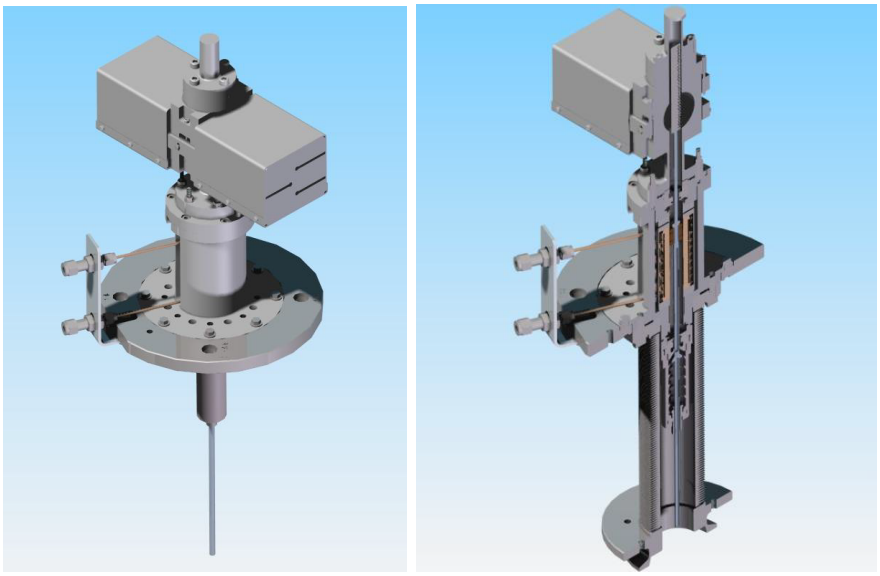

Figure 3.4: MICE target assembly

must travel 24mm. It must do this over the course of about 1 to 2 ms which corresponds to the window in which the protons are near their maximum energies, and must exit the beam again before the next pulse approaches [43]. This is complicated further by both long term and short term drifting in beam position and timing, so that the target must be adaptable to changing beam conditions.

In order to meet these requirements, the target must accelerate on the order of $780 m/s^2$ or about 80g. A linear electromagnetic drive was implemented to overcome these challenges. Permanent magnets on the target shaft are surrounded, held, and then accelerated by a stator consisting of current carrying coils cooled by a water system. Should power be lost to the coils the whole target assembly is on a frame which can be raised completely out of the ISIS beam.

3.3.2 Beamline Magnets

The beamline magnets consist of nine focusing quadrupoles broken into three groupings of three magnets, two bending dipole magnets and a 5T decay solenoid (DS) (see Fig 3.3). The initial pion spray from the target is captured by the first of the three sets of quadrupole magnets (Q1-3) which transport the pions to the first dipole magnet (D1). The beam is then momentum selected by adjusting the current through D1. Pions outside of the selected momentum range will fail to be transported to the DS.

The purpose of the DS is to increase the path length of the beam and provide the additional time needed for pions to decay to muons. Used in combination with D2 it allows MICE to run in two different settings: a high purity muon beam and a more heterogeneous beam consisting of a mix of muons, pions, and electrons. These beams are achieved by selecting for either backward decaying muons (high purity muon beam) or forward decaying (heterogeneous beam). While the high purity muon beam is desired for data taking, the heterogeneous beam allows for the calibration of MICE's PID detectors (see Fig 3.5)[44].

The final two sets of quadrupoles, Q4-6 and Q7-9, are used to maintain the beam as it travels unto the cooling channel.

3.3.3 Proton Absorber

When running with a positive beam protons from ISIS can enter the MICE beam. While these can be easily identified from TOF it is better to remove them from the beam so that they don't overwhelm the readout electronics. Protons will lose significantly more

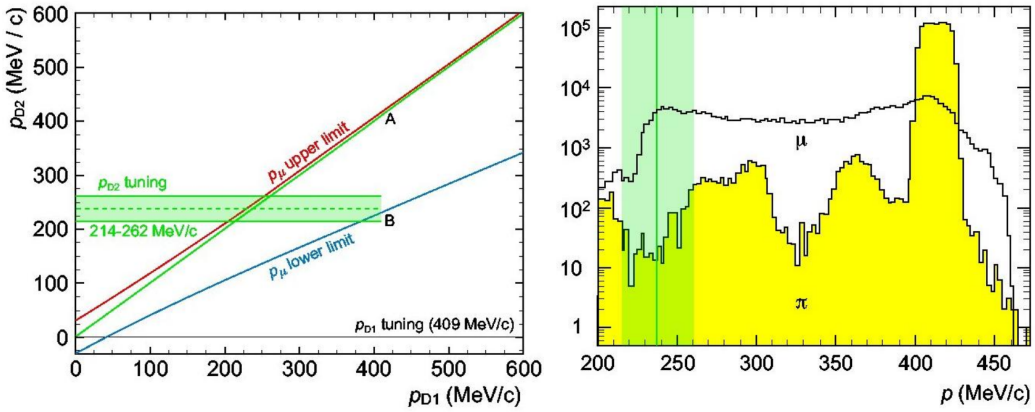

Figure 3.5: Momentum tuning in the selection of the composition of the MICE beam. (left) The kinematic limits of muons produced in pion decay. More forward decaying muons are kinematicly similar to the pions they decay from. (right) Simulation showing pion and muon spectra at the end of the decay solenoid. The green band shows the acceptance of D2 for a muon beam[44].

energy traveling through material than either pions or muons, however, so to remove this source of contamination the proton absorber was commissioned. The proton absorber is a series of four plastic sheets of different thickness (15mm, 29mm, 49mm, and 59mm) which can be lowered into the beam. Different thicknesses are used depending on the input beam momentum, so as to have as little impact on the beam as possible while still completely removing proton contamination.

3.3.4 Diffuser

The diffuser is the final element of the MICE beamline (Fig 3.6). The diffuser is a series of four irises, two of brass (2.97 mm, 0.2 X_0, and 5.94 mm, 0.4 X_0 thick) and two tungsten (2.80 mm, 0.8 X_0, and 5.60 mm, 1.6 X_0) that allow for a maximum of $3X_0$ in $0.2X_0$ steps[44]. The diffuser is located just outside the spectrometer solenoids and in the presence of a large magnetic field, which precludes the use of a motor to drive the iris petals. To compensate the irises are driven by an air-driven actuator and monitored by optical sensors. The diffuser allows for a study of a range of initial beam emittances.

3.3.5 Scaler Detectors

The MICE beamline also has a host of scaler detectors or counters. These detectors were, at first, designed to be temporary, to provide the collaboration with an early and easy means to verifying that the MICE beamline was performing as intended. However, despite the addition of more sophisticated detectors over time, these detectors have remained in

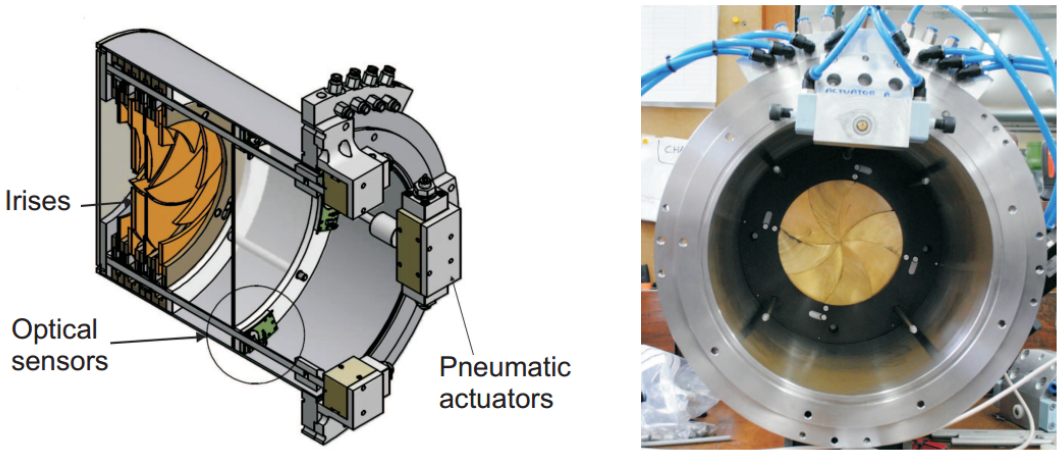

Figure 3.6: The MICE Diffuser selecting which set of 4 irises are open or close allows for a selection of input beam emittance[44].

the beamline, largely because of their simplicity and reliability. These detectors are: the luminosity monitor (LM), the GVA scintillator, and two beam profile monitors(BPM).

The LM sits within the radius of the ISIS synchrotron, located 10 meters from the MICE target and at an angle of 25° from the tangent of the ISIS beam at the target. It is placed such that the flux of particles through the LM is roughly equivalent to the flux captured by the Q1-3. The detector is designed so that coincidence between two sets of isolated scintillating box and PMTs are required for a signal count.

The GVA and BPMs are simpler devices than the LM. The LM consists of a single slab of scintillating material ($200 \times 200 \times 10$ mm^3) read out by a single PMT. The BPMs are formed of fibers of scintillating material arranged in two layers along the X and Y axes. Each layer is read out by a single PMT. BPM1 covers an area of 200×200 mm^2, consists of 192 fibers per layer while the larger BMP2 (450×450 mm^2) has 432 fibers per layer.

The positioning of these counting detectors allows for the monitoring of beam health as particles traverse the MICE beamline and for the identification of problems in any single element in that beamline up to Q7-9. In addition to these monitors the ISIS synchrotron is equipped with 39 beam loss monitors which measure the loss of particles as the ISIS beam travels around the synchrotron used by the MICE collaboration to verify the proper operation of the MICE target.

3.4 Cooling Channel

The cooling channel (Fig 3.7) hosts the ionizing absorber and three superconducting magnetic assemblies: two spectrometer solenoids, and the focusing coils around the absorber. The two scintillating fiber trackers are also present in the cooling channel, but they will be discussed in section 3.5

3.4.1 Spectrometer Solenoids

The two spectrometer solenoid (SS) modules provide a uniform 3T field necessary for the precise measurement of particle momentum. Each module consist of 5 Nb-Ti superconducting coils wound on a single aluminum mandrel[45]. The magnets of a SS are: two end coils, a center coil, and two matching coils. The 3T field is produced by the center and end coils. A scintillating fiber tracker, the detector responsible for position measurements, sits completely within the volume of each center coil. The two matching coils are located nearest the absorber. These magnets match the beam in the SS to the one in the absorber module.

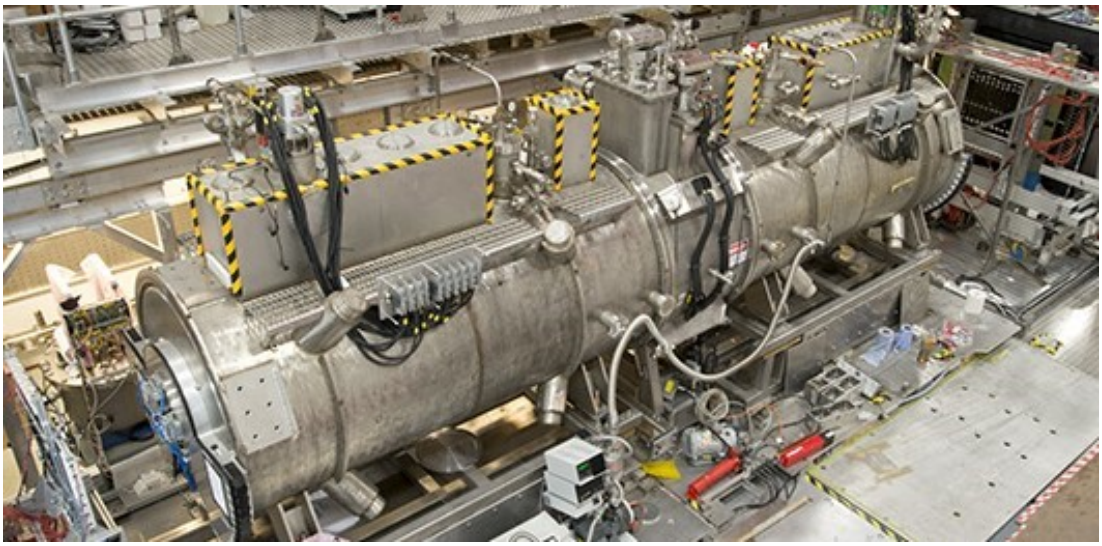

Figure 3.7: MICE cooling channel. The twin spectrometer solenoid modules located at either end of a single absorber focusing coil module before the instillation of the partial return yoke.

3.4.2 Absorber Focusing Coil Module

Step IV tests the performance of a single absorber focusing coil (AFC), while later the demonstration of cooling will use three AFC modules. The absorbing material, responsible for ionization cooling, is located at the center of the AFC module. The absorber is bookended by two superconducting solenoidal focusing coils. The purpose of these coils is to provide a powerful focusing field which will reduce the $\beta_\perp$ Twiss parameter of the beam as it moves through the absorbing material. Minimizing $\beta_\perp$ is a critical condition to minimizing ϵ_{equ} and maximizing $d\epsilon/dz$ as discussed in section 2.3. The focusing coils are designed to run in two modes, a solenoidal mode where the polarities of the two magnets are in the same direction and a 'flipped' mode were they are not. A potential cooling channel consisting of many AFCs will require flip mode running to minimize growth in angular momentum over time.

Step IV will study the material properties of lithium hydride (LiH) and liquid hydrogen(LH_2). These materials were identified as possible ideal absorbers due to their low atomic numbers. The LH_2 will be contained a 21 liter aluminum vessel while the LiH takes the form of 65 mm thick disk.

3.5 Particle Detectors and Trackers

MICE hosts a suite of particle identification (PID) detectors providing the experiment the tools needed to reject contamination and ensure data purity ($> 99.9\%$ muons). Upstream of the cooling channel are the first two of the experiment's two time of flight (TOF0 and TOF1) detectors which provide the initial particle species hypothesis as well

as serving in the role of experimental trigger for data collection. Downstream of the cooling channel TOF2 working with TOF0 and TOF2 further informs the particle hypothesis and provides important information on its evolution as it moves through the cooling channel. These detectors are particularly well suited for initial PID and in identifying pion contamination downstream of the cooling channel.

A second set of detectors located at the back end of the MICE hall at the end of the beam are the KLOE Light (KL) and Electron Muon Ranger (EMR) detectors, both of which are calorimeters. The KL, a single layer calorimeter consisting of a mixture of scintillating bars and lead, and the EMR a multi-layered totally active calorimeter. The KL makes an initial measurement and provides the material in the beam to induce a showering of the electron. The EMR generates tracks as particles move through its volume as well as recording energy loss of the particle along the path. The EMR takes advantage of the different penetration profiles of the wide yet shallow incident electron shower versus the tight and deeper penetrating muon track to identify electrons produced by muon decay which may have been missed by the TOFs

The final set of detectors are the trackers located within the spectrometer solenoids equally distant from the AFC. The trackers are responsible for performing the high precision measurement of position and momentum needed in determining the change in emittance as a particle traverses the cooling channel.

3.5.1 Time of Flight (TOF) Detectors

As stated above MICE uses three TOF detectors (TOF0-2). The sensitive area of each TOF is 40 $\times$ 40 cm^2, 42 $\times$ 42 cm^2, and 60 $\times$ 60 cm^2, for TOF0, TOF1, and TOF2

respectively. The TOFs are comprised of a number of scintillating slabs each of which is 6cm wide in TOF1 and TOF2 and 4cm wide, such that TOF0 and TOF2 consist of 10 slabs per layer and 7 slabs per layer in TOF1 (see Fig 3.8). The detectors contain two layers which run perpendicular to each other along the X-Y axes. This allows transverse position measurements with a resolution on the order of ten mm and utilizes the timing difference between the two PMTs on a single slab. Finally a coincidence requirement, hits in both PMTs in both X-Y slabs (total of 4 PMT readings) in TOF0 is commonly used as the triggering signal preparing the rest of the electronics in the experiment to start recording data.

The TOFs provide high precision time measurements with measured resolutions of 51ps, 58ps, and 52ps for TOF0, TOF1, TOF2 respectively[46]. This resolution is then sufficient for PID as the expected splitting of the time of flight between TOFs due to mass considerations is on the order of ns (Fig 3.8). In practice though PID through only time of flight is complicated due to particle scrapping, variations in path length through the various magnets in the experiments, and the possibility of muon or pion decay while in beam.

3.5.2 Electron Muon Ranger (EMR) and KLOE Light (KL)

The EMR and KL serve as the experiment's calorimeters, the primary function of which is to distinguish decay electrons that may have arisen from the spontaneous decay of muons while moving though the experiment. Electrons entering the experiment through the D2 magnet will produce a clear timing signature in the TOFs; however those that arise later through decay may exhibit kinematic signatures similar to the mother particle muon.

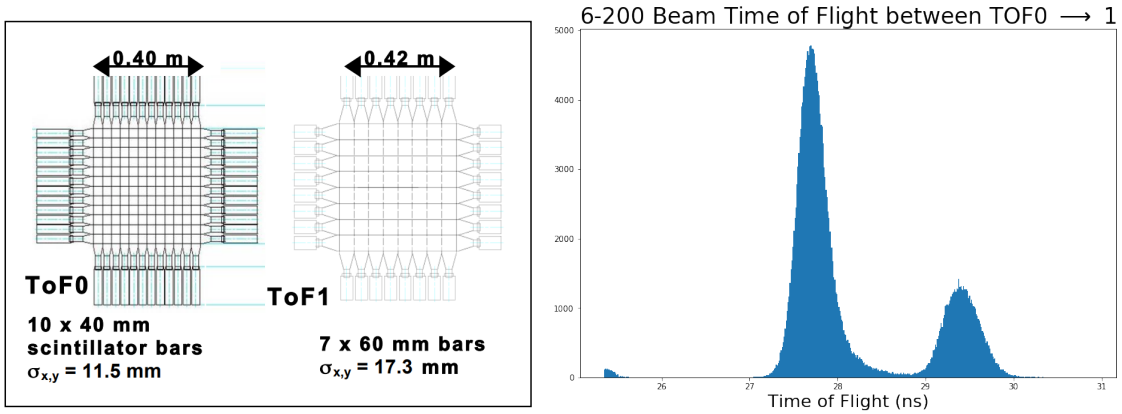

Figure 3.8: (left) Schematic view of upstream TOF0 and TOF1 showing the relative size and layout of the scintillating fibers and position of the PMTs[46]. (right) Separate electron, muon, and pion peaks evidenced by different flight times between TOF0 to TOF1.

In order to veto these events a dual detector solution has been implemented at the rear of the experiment.

The KL is a pre-showering sampling calorimeter. The KL is composed of an extruded lead base though which scintillating fibers run at a ratio of 2:1 lead to fiber (Fig 3.9). The fibers have a diameter of 1 mm, are separated from neighboring fibers by 1.35mm, and the distance between any two layers 0.98mm is displaced by half the fiber pitch. The total active volume of the KL is 93 $\times$ 93 $\times$ 4 cm^3 equivalent to a 2.5 X_0 thickness. This geometry is broken up into 21 cells and read out by 42 PMTs, one at either end of each cell[44].

The EMR is a totally active calorimeter consisting of 48 planes of 59 tessellated triangular scintillating bars per plane. The bars are placed such that each bar is rotated by 180° when compared to the bars next to it, so that there are no empty areas within the

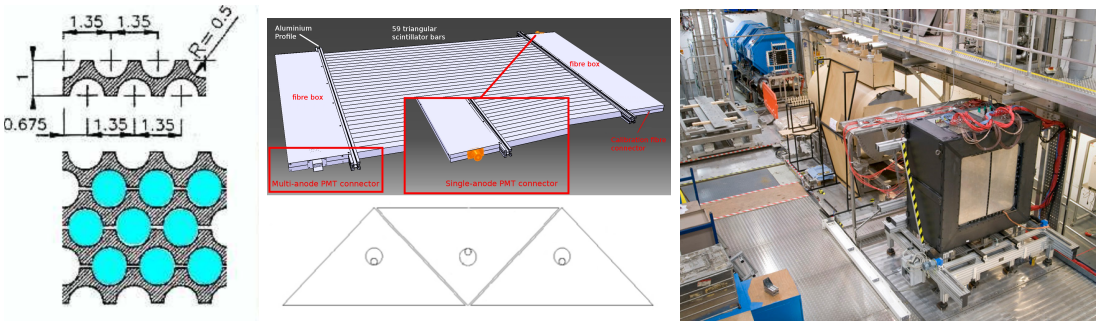

Figure 3.9: Schematic view of upstream of the (left) KL, (center) a single EMR plane and (right) the placement of the EMR in the hall with a mock up of the spectrometer solenoids and Q7-9.

EMR (Fig 3.9). The planes are each rotated by 90° with respect to the previous plane to present an X-Y view; each plane covers a square area of 1.21 m^2. Light produced by a plane is collected on one end of a plane by a single-anode PMT while on the other end an array each one of the bars is read out to a single pixel of a 64 channel multi-anode[47].

The KL is placed directly behind TOF2 and directly in front of the EMR. Electrons passing through the KL produce a particle shower which travel onwards to the EMR. The incident shower produces a markedly different characteristic profile than that of the muon which traverses the KL without inducing a similar shower. The granularity of the EMR allows the path of the particles to be tracked for PID analysis.

3.5.3 Scintillating Fiber Trackers

Emittance measurements in MICE are performed by two scintillating fiber trackers (Fig 3.10), one located on either side of the AFC. Measurements of the change in emittance

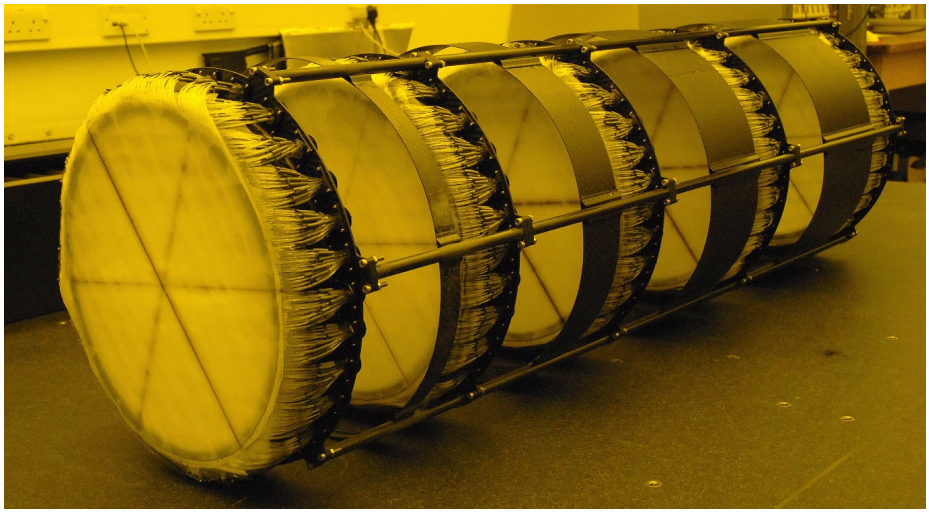

Figure 3.10: One of the scintillating fiber trackers in MICE. Clearly presented are all five stations of the tracker and where the fibers are run out to connectors on the station frame. The cross markings on each station denote the direction the fibers run in each of the three planes in the station.

before and after a particle traverses the absorber are measured to a precision of 0.1%. The trackers are located in a 3T magnetic field responsible for inducing the helical motion that makes measurements of both position and momentum.

Each tracker consist of five stations, each with a unique spacing from its nearest neighbors, so that an integer number of turns along the helical path can be resolved. The downstream tracker is rotated with respect to the upstream tracker by 180° so that the trackers mirror each other. Station one is defined then as the station closest to the AFC module. Each one of the five stations is comprised of 3 planes, rotated at an angle of 120° in the transverse plane with respect to one another; this defines the u, w, and v planes. Finally each plane contains a doublet layer of 1491, 350μm diameter scintillating fibers (1477 in the u) ganged into groups of seven for a total of 213 (211) channels. The fibers in the doublet layer are stacked such that the fiber pitch is 470μm and provide complete coverage of the 30 cm diameter active area of each station (Fig. 3.11). This geometry, gangs of seven fibers and the orientation of the three planes, allows for a positional resolution of 427μm. These statistics are summarized in Table 3.1 for reference[48].

These channels are connected to optically clear wave guides via connections along the rim of the carbon fiber station frame and run out of the spectrometer solenoids through end plate connectors at the outside edge of each SS. The expected signal from an event in a single fiber is 10 photo-electrons. To read this signal low band-gap silicon avalanche devices visible light photon counters (VLPCs), cryogenically cooled to 9K to reduce thermal noise, are used to amplify the signal. The VLPCs have been shown in some circumstances to have

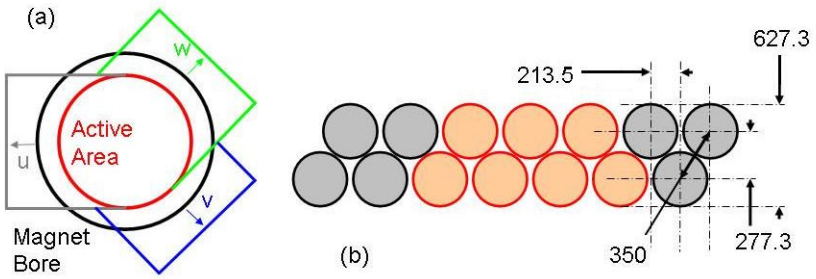

Figure 3.11: (left) The directions of the three doublet layered planes that define the 30cm diameter active area in each tracking station. (right) Layering of the doublet plane showing a single ganged channel of seven fibers in red.

a gain as high as 50,000 and a quantum efficiency above 80%. The signal is digitized via the Analogue Front End with Timing (AFE IIt) board developed for the DØ experiment.

Scope	Parameter	Value
Station Plane:	Fiber Diameter	350 μm
	Fiber Pitch	427 μm
	Number of Fibers	1491 or 1477
	Number of Channels	213 or 211
Tracker Station:	Number of Planes	3
	Rotation of Planes	120°
	Position Resolution	470 μm
	Sensitive Area Diameter	30cm
Trackers:	Number of Stations	5
	Station Separation 1 $\rightarrow$ 2	20cm
	Station Separation 2 $\rightarrow$ 3	25cm
	Station Separation 3 $\rightarrow$ 4	30cm
	Station Separation 4 $\rightarrow$ 5	35cm
	Total Length	110cm
MICE:	Rotation of Downstream Tracker	180°

Table 3.1: Reference figures for the two scintillating fiber trackers in MICE [48]

Chapter 4

MAUS Analysis User Software (MAUS)

MICE has three large software packages, MAUS is the software package developed by the MICE collaboration to meet its analysis needs. As both a particle physics experiment and an accelerator experiment MICE requires a software package that can both analyze data from the DAQ, either in real time or from file at a later time, and simulate the expected performance of the experiment. This includes simulating not only the physics involving particle interactions, but that of the various electronics in the experiment and calculating the relevant transfer matrices and Twiss parameters[49]. Not covered in this document are the other two MICE software packages: the controls and monitoring software which employs a state machine paradigm to ensure the quality of data taking and preserve the health of the experiment, and the DAQ system which facilitates communication between the outside

world and the bank of front end boards in the MICE rack room from which MICE data are processed.

Included in this chapter is a discussion of the design philosophy of MAUS. Also included is a section specifically dedicated to the reconstruction software for the MICE scintillating fiber trackers found within the MAUS framework.

4.1 Design Philosophy

MAUS has been the official software of MICE since 2010. Before the introduction of MAUS the experiment used the G4MICE package, which was created in 2002. Over time though, much of the documentation and test coverage for that package was lost, if it ever existed to begin with. This created an environment in which development and use of the code became very challenging for new users, introducing a bottleneck in the further development. Because of this it was decided that the G4MICE software would be frozen and parts of it exported to a new software project, MAUS.

The central design philosophies of MAUS come from utilizing concepts pioneered in industry to impose structure, maintain feasibility, and lower the bar for development on the code. Perhaps the most important change was in the implementation of how the code was maintained. Appointing a MAUS maintainer while migrating the code to a version controlled bazaar repository and mandating that all new code contain tests, allows for daily bug checks on the code. Any new code that breaks functionality can be 'rolled back' and sent back to the submitter for revision. In such a way the code maintains a stable base even as it is continuously developed.

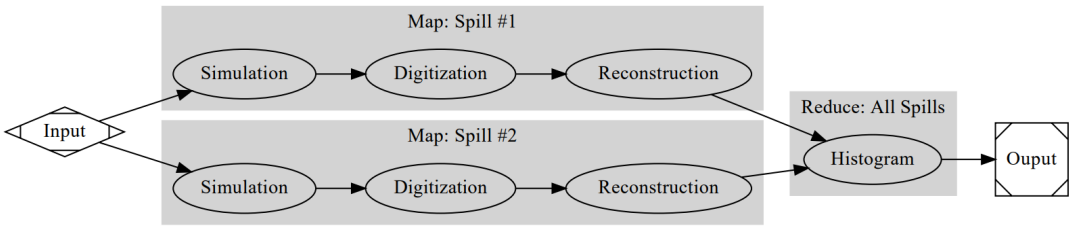

Figure 4.1: The MAUS map and reduce structure. Each spill is processed separately.

The basis for the code was switched from a purely C++ code base to using a python script to drive individual analysis written in either C++ or python. A 'map' and 'reduce' structure was adopted as well. In this notation 'map' is any routine that takes in a singular data point and transforms them to some other type of data, while a 'reduce' takes multiple data points and transforms it into one point of data[50] (see Fig. 4.1). These changes further lower the bar for new developers.

The fundamental processing unit in MAUS is the spill. A spill is defined by the particle event data collected immediately after a single dip of the MICE target into the ISIS beam. Each spill usually is on the order of 100 triggering events, which of course varies with experimental conditions, or in the case of simulation, with input parameters. Spills are self-contained units in the data, designed to facilitate the use of parallel processing.

The original implementation of MAUS used a JSON file format to store and pass data to and from analysis modules. JSON is a human readable text file will strong integration into the python language. Adopting JSON was intended to be another measure to lower the bar for new developers. However, the required processing power for passing around such a large text file precluded the ability to run live reconstruction during data

taking. To overcome this limitation JSON was phased out over the course of two years, a process that ended in 2015. Currently data are stored in memory as a ROOT TTree[51] and written out to file at the end of the run.

4.2 The Reconstruction Software for the MICE Scintillating Fiber Trackers

The tracker reconstruction software exists within the larger MAUS framework. The tracker reconstruction is actually a series of reconstruction routines, each existing within the 'map' structure of MAUS. Each of the tracker maps is written in python yet drives a C++ recon script. The reconstruction processes the data from a starting point of either simulation or DAQ hits and ends with a fully reconstructed particle track. Before beginning a more serious discussion of these routines a quick overview of the reconstructed data steps is presented below:

- **Raw Data/Scifi Hit** Light signal recorded from particle interaction via ADC (Raw Data) or from Monte Carlo simulation (SciFi Hit).
- **Digit** Raw data digitized, Contains channel, plane, station, tracker and signal information.
- **Cluster** Grouping of nearest neighbor digits from particles crossing two or more channels through the plane.
- **Spacepoint** Collection of two or more clusters, across two (doublet) or three (triplet) planes in a single station. Spacepoints must have at least a 10 photo electron signal.

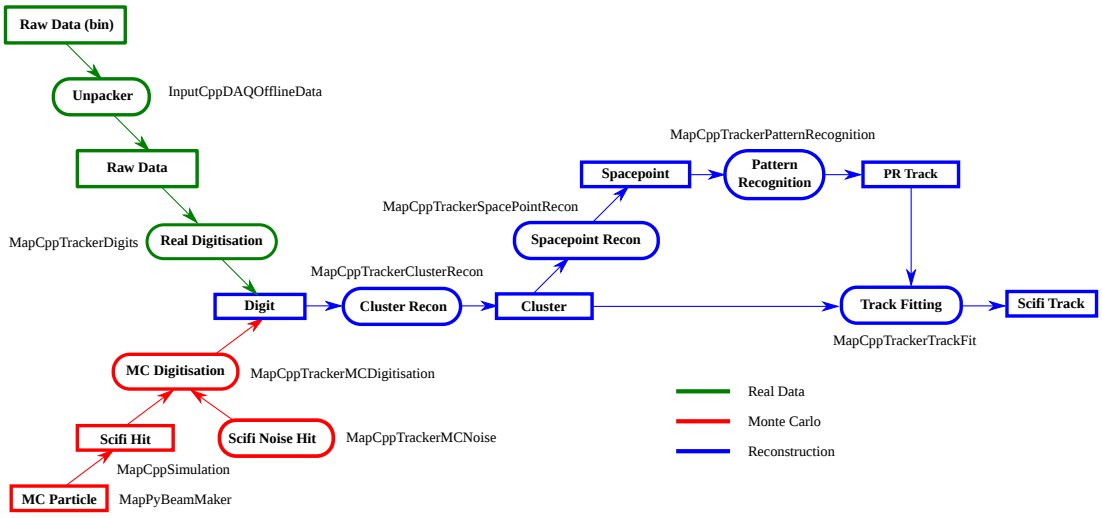

Figure 4.2: Data flow of the tracker reconstruction software. Shown are each of the data types and the reconstruction routines that are responsible for performing the reconstruction.

- **Pattern Recognition Track (PR Track)** Collection of spacepoints in a tracker from which either a straight or helical curve fit can be reconstructed.

- **Scifi Track** PR Track point corrected for multiple scattering using Kalman Filtering technique.

Figure 4.2 maps how these layers connect[52].

Data are stored in its own class with pointers back to lower level reconstruction and up to the point of digits. The reconstruction is blind to the source of the data to ensure MC and data are treated on equal footing. Figure 4.3 outlines how the reconstructed data fits within MAUS.

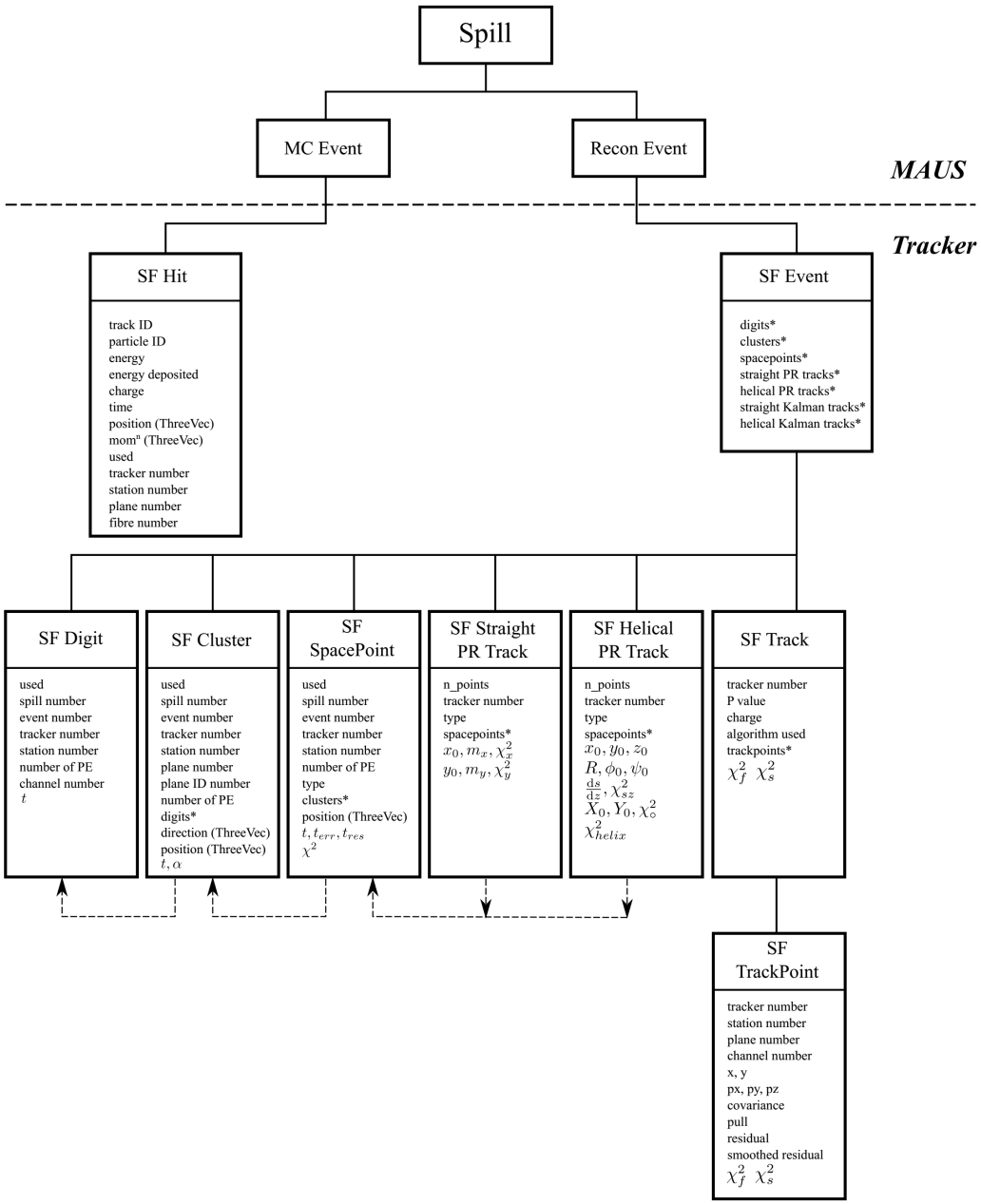

Figure 4.3: Tracker reconstruction class and data found within that class within the MAUS framework. Each higher level reconstruction contains a pointer back to lower level data so that the reconstruction may be traced[53].

4.2.1 Simulation

The Monte Carlo simulation in MAUS is driven by Geant4[54], a commonly used toolkit in the field developed specifically for modeling the passage of particles through matter. Geant4 models single particle events, which are steps through the experiment by a user defined step size. Along the way energy loss and scattering angles from multiple scattering are calculated. At each detector's geometric boundary however Geant4 is required to stop and compute a measurement within the detector.

For the simulated trackers this boundary is at the level of a fiber. Each of the 45,000 some fibers of the tracker are modeled individually. Within the fiber body energy loss, as calculated by Geant4, is recorded as being deposited in totality within the fiber. In real data digitization fibers are ganged into groups of seven and read out together. Therefore in simulation fiber number is correlated back to the correct channel number and the hit is assigned a channel number rather than fiber number. Any additional steps through the fiber or steps through fibers within the same channel are stored as multiple hits within the channel.

The MC digitization routine takes this data and does two things. First it converts the total energy deposited into the channel into a number of photo electrons (PE). This is a simple calculation based on a number of physical properties of the fibers, such as reflectivity, quantum efficiency and transmission coefficient.

The second process is an additional MC simulation, for the electronics responsible for making the measurements. The calculated PE signal is analog, in so far as it is within the size limit of the computer memory allocated to it. However, photons are quantized

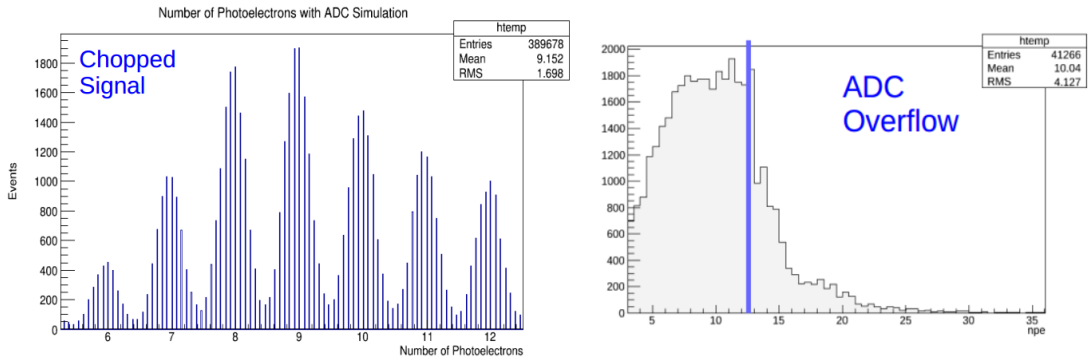

Figure 4.4: (left) Simulated tracker data is quantized, smeared, and digitized. (right) ADC digitization includes simulating overflow.

particles. The first step then is to quantize the incoming signal by rounding down to the nearest integer. The signal is then smeared, as a Gaussian, to simulate the VLPC electron avalanche. The data for the range of this smearing comes from calibration testing. The final step is a digitization of the data to simulate the 8-bit ADC boards. The spacing between bits and the overflow values are determined by the pedestal and gain calibrations for each ADC board (Fig. 4.4)

The results of this process are saved as a digit and passed on for cluster reconstruction. Optionally the user can choose to turn on an additional level of simulated noise in the form of a Poisson modeling of thermal noise in the VLPC. Even cooled down to 9K, the VLPCs have some amount of noise, which comes from the random cascading of electrons from thermal vibrations. It is estimated that in each data taking window (single particle event), there is 1.5% chance per channel of the process occurring. With nearly 7000 channels

in the tracker active during these periods, this process can produce significant background noise.

4.2.2 Reconstruction

A more detailed examination of the reconstruction routines responsible for producing the terms introduced at the start of the section is now in order.

Real Data Digitization

The process of creating digits from simulated hits is covered in detail in section 4.2.1. Real data digitization reads in signal output from the ADC boards as well as the corresponding ADC channel. Calibration and data are used to perform a linear transformation on the signal as a fuction of the ADC pedestal and gain:

$$PE = \frac{ADC - ped}{gain}. \tag{4.1}$$

Each ADC is calibrated independently; calibration checks are performed routinely to check for drift in pedestal and gain. Mapping from ADC channel to tracker channel, plane, station, and tracker is performed via a stored mapping file which is generated via an external script that traces the physical location of the fiber waveguides from tracker to VLPC to ADC.

Clusters

Cluster reconstruction loops over all the digits within each individual tracker, station, and plane over the course of a single particle event, searching for nearest neighbor hits above a single PE cutoff. If no nearest neighbor can be found a single digit can form

a cluster as well. While a single PE cutoff is sufficient for the nearest neighbor search the total PE of a data point must be over 2PE to actually create a cluster. If a nearest neighbor is found a new channel number is created from the average of the two channels.

Spacepoints

Spacepoints are formed at the intersection of channels containing clusters in either all three of a station's planes (triplet) or from any two of the planes (doublet). The reconstruction preferentially searches clusters first for triplet points. This search is performed using "Kuno's conjecture" which states that sum of the channel numbers in any three intersecting channels is approximately equal to the summed average number of the total number of channels in each plane, or:

$$((n^u + n^w + n^v) - (n_0^u + n_0^w + n_0^v)) < K, \tag{4.2}$$

where n^u, n^w, and n^v are the channel numbers of any clusters in the u, w, and v planes, n_0^u, n_0^w, and n_0^v are the central channel number in each plane and K is the triplet forming condition, usually set to $K = 3$.

Doublets are formed from the remaining clusters; here the requirements are less stringent, requiring only that the reconstructed spacepoint falls within the tracker active area. Spacepoints contain the first reconstructed position information of a tracker event. Positional measurements are made by rotation of clusters out of a plane coordinate frame into the experimental reference frame. A cluster has a position defined by[53]:

$$\begin{pmatrix} x \\ y \end{pmatrix} = R \begin{pmatrix} \alpha \\ \beta \end{pmatrix} = \begin{pmatrix} \cos\theta_D & -\sin\theta_D \\ \sin\theta_D & \cos\theta_D \end{pmatrix} \begin{pmatrix} \alpha \\ \beta \end{pmatrix}, \tag{4.3}$$

where θ_D is the rotation of the plane (0, 120°, or -120°). The plane coordinates α, β are the distance from the central channel of the plane and the position along the channel length respectively. α is defined as:

$$\alpha = c_p(n - n_0), \tag{4.4}$$

where c_p is the channel width of $\approx$ 1.5cm, n is the channel number of the cluster, and n_0 is the central channel number of the plane.

There is no mechanism in place to determine β independently: two crossing clusters must be used. Using a second crossing cluster and substituting for the x, y term gives β as:

$$\begin{pmatrix} \alpha_1 \\ \beta_1 \end{pmatrix} = R_1^{-1} R_2 \begin{pmatrix} \alpha_2 \\ \beta_2 \end{pmatrix}, \tag{4.5}$$

allowing

$$S = R_1^{-1} R_2 = \begin{pmatrix} s_{11} & s_{12} \\ s_{21} & s_{22} \end{pmatrix} \tag{4.6}$$

which yields β for each cluster as:

$$\beta_2 = \frac{\alpha 1 - s_{11}\alpha_2}{s_1 2} \tag{4.7}$$

$$\beta_1 = s_{21}\alpha 2 + s_{22}\beta_2. \tag{4.8}$$

Once β has been calculated for each spacepoint Eq.4.3 can be employed to determine spacepoint x, y positioning in the tracker frame. This is then translated into the experimental frame via the stored geometry, informed by survey measurements of the MICE hall.

Pattern Recognition

Pattern recognition comes in two flavors: straight and helical track reconstruction. The type of reconstruction used is set by the user, based on the presence of the 3T field. Both routines operate under similar principles: approximate tracks are generated using a minimum number of spacepoints over the maximum separation in z, spacepoints are collected near that approximate track, and if at least one additional spacepoint is found a linear least squares fit is applied to the collection of points.

The helical PR is performed in cylindrical coordinates given by (ρ, ϕ, z) where ρ is the radius of the subtended circle, ϕ is the rotation in the transverse plane and z is the longitudinal length. Defining the variable s to be the length of the arc swept out in moving from one spacepoint to the next, and Ψ as the azimuthal angle of the line tangent to the track, $(\phi + \pi/2)$, the track is parameterized by:

$$\mathbf{v} = \begin{pmatrix} x_0 \\ y_0 \\ \Psi_0 \\ \frac{ds}{dz} \\ \rho \end{pmatrix} \tag{4.9}$$

A detailed examination of how a track is formed from these points is worked out in Ref. [53]. Once the linear least squares fit has been completed every point used in the fit is compared against the new track and a figure for χ^2 is determined. If the χ^2 figure is sufficiently small, by default < 15 multiplied by the NDF then a second linear fit will be carried out. This linear fit is along the straight line that is defined by the (z, s) plane. If the χ^2 for this fit is sufficiently small as well (< 4.0 times the NDF by default) then the track is recorded

A similar process is performed in the straight track reconstruction, except here obviously a circle is not subtended by a straight line drawn between two spacepoints. Just as for the helical PR, if any additional spacepoints can be found that are sufficiently close to this line a linear least-squares fit is performed. Like the straight line fit in (z, s) space from the helical fit, if a sufficiently low χ^2 can be found(< 4.0 times the NDF) the straight track is recorded.

In both of these routines should a track fail to reconstruct the spacepoints are used again and in a different permutation will be examined. This is done specifically to deal with the case of more than one spacepoint in a tracker station, as selecting a background spacepoint will throw off reconstruction. Once a track has been formed any remaining spacepoints will be used to try to find secondary tracks in the tracker.

Scifi Track

The Scifi track fitting routine differs from the PR track in the use of a Kalman filter[55, 56]. The Kalman filter is an iterative routine that incrementally propagates an estimate of track states. The PR track provides the seeds for the parametrization of the

Kalman track fit while the clusters are passed in as the measurement data. The Kalman filter corrects for noise in the track through multiple scattering via the Highland formula and energy loss through the tracking medium and helium gas using the Bethe formula.

Chapter 5

First Transverse Emittance Measurements in MICE Step IV

In this chapter results from the first transverse emittance reduction in MICE Step IV are present. Section 5.1 provides a quick outline of which data sets were used in this analysis. Beam setting and run information are presented in greater detail in Appx. A.

Event selection was performed via two different analysis techniques. The first technique, discussed in section 5.3, uses curve fitting on TOF0 $\rightarrow$ 1, TOF1 $\rightarrow$ 2, and Upstream/Downstream reconstructed effective masses. Assumed in this approach is that tails in these peaks are due to scraping of particles along the side of the solenoid bore or in abnormally large interactions with material present within the beam. The second technique uses unsupervised Gaussian mixture method to find patterns in the five dimensional detector space as defined by the TOF0 $\rightarrow$ 1, TOF1 $\rightarrow$ 2, TOF0 $\rightarrow$ 2, and Upstream/Downstream

effective mass reconstruction axis. These criteria are discussed in section 5.4. Both analysis share a number of selection criteria; these similarities are discussed in section 5.2

In the following discussion all figures depict the 6-200 run. Additional figures can be found in Appx.B and Appx. C. Additional information pertaining to the beam settings used is presented in Appx. A

5.1 Data Sets

The data evaluated in this analysis come from the ISIS User cycle 2016/04, collected between November 28 through December 16, 2016. The data covers eight of the nine optical configurations (momenta: 140, 200, 240 MeV/c and initial emittance 3, 6, 10 π mm rad), as shown in table 5.1. Beams in this set were directed through the LiH absorber, which was installed during the ISIS User Cycle 2015/04 (Feb-Mar 2016). The data was analyzed using MAUS 2.7.0 which was released December 19 2016.

These data represent the most complete Step IV LiH data taken to date. The downstream spectrometer solenoid (DSS) is not running with either matching coil which leads to a large emittance growth in the downstream tracker (DT). This is compensated by the Kalman routine which is used in predicting the initial momentum information at DT plane 1 right after the absorber. The downstream optics have been adjusted accordingly to ensure beam transmission to the downstream detectors of post-cooling channel PID and allowing for a measure of muon-ness of the outgoing beam.

Momentum (MeV/c) \ Emittance (π mm rad)			
3-140	6-140	10-140
3-200	6-200	10-200
	6-240	10-240

Table 5.1: (Left) Initial momenta and emittance of the 2016/04 data sets evaluated in this analysis. There is no data available at the 3-240 setting. Data covers expected NF cooling requirements.

5.2 Common Event Selections Criteria

There are three primary concerns when looking for events to consider in the final analysis: PID, proper reconstruction in the tracker, and minimizing the effects of particle interaction with the sides of the experiment. The criteria shared between the two selection analysis include all three of these concerns. However, PID is limited to detecting decay positrons in the EMR.

Initial event selection is provided by a simple TOF1 coincident trigger. This requires that at minimum two slabs in TOF1 record a hit, a single hit in the X-plane and another in the Y-plane. This is a sufficient requirement to prevent overloading of the DAQ system while maximizing the data collected. Generally a single spill will contain 100 TOF0 triggers per spill, where a spill is defined as a single dipping of the MICE target into the ISIS beam. Secondary cuts done after MAUS reconstruction include checks on the radial

path length of the particle within the tracking area, track fit goodness parameters, and EMR χ^2 and plane densities.

5.2.1 Tracker Cuts

There are two simple event selections preformed using only the twin cooling chamber scintillating fiber trackers. The first of these is a radial cut: the active plane of each tracker station is defined by a 15 cm radius through which the fibers of each of three planes cross while the inner most radius of the solenoid bore is 20 cm. In between the area carved out by these two figures lies the tracker superstructure of carbon fiber and the clear light guide wire connecting the scintillating fibers to the VLPCs. In order to negate the influence of any scraping against these components a strict radial cut of 15cm from the center of the tracker fiducial area was imposed; if any part of the reconstructed particle path is outside this area that event is removed.

The second selection is a parameter quantifying how well the tracker was able to make a measurement of the particle event. Two factors go into the determination of this parameter: the number of doublet or triplet spacepoints, and the Kalman filter P-value. For the purpose of this analysis a requirement was set that each of the 10 tracking stations must record either a doublet or triplet spacepoint and the P-value of the Kalman filter must be above 0.01.

5.2.2 EMR Cuts

The parameters in the EMR cut were developed from a September 2013 run and reported November 2015 [47]. The data represent a series of runs at different beam purities

and scanned over a D2 selected momentum range of 230 - 450MeV corresponding to 200 - 420 MeV for muons and pions and 100 - 250MeV for positrons. The purpose of the EMR PID is to clearly separate positrons and muon events, primarily to identify muons that may have decayed in the cooling channel which would be difficult to detect using only TOF measurements.

An positrons traversing the EMR will differ from a muon in two primary ways. First, a muon traveling through the EMR will leave a signal in near 100% of the scintillating slabs it travels though, while the positrons will not. This plane density is defined as:

$$\rho = \frac{N_x + N_y}{Z_x + Z_y}, \tag{5.1}$$

where N is the number of planes reporting at least one slab hit in both the x and y planes, and Z is the plane number of the deepest plane to record a hit. Second, positrons will tend to shower while traversing the KL while muons will pass through intact. This will produce many short lived particles in the first half of the EMR planes while deeply penetrating but lower energy photon events will produce hits further down the EMR.

The muon and positron distributions were examined for both ρ and χ^2. Particle species was determined via a 90% confidence requirement as described by the intersection of the three time of flight distributions

$$TOF0 \rightarrow 1 \cap TOF0 \rightarrow 2 \cap TOF1 \rightarrow 2 > 90\% \tag{5.2}$$

The results of these studies is shown in Fig 5.1.

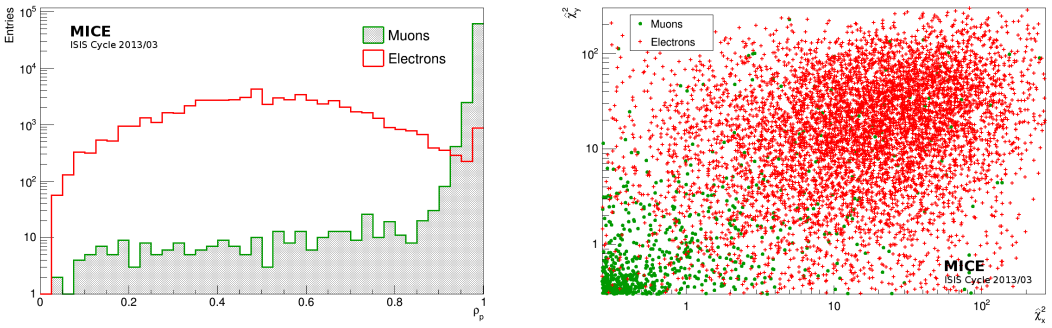

Figure 5.1: (left) EMR plane density the positrons distribution has been normalized to match the number of muon events. Muon events show a clear peak near $\rho = 1$, while the positron peak is spread around $\rho = 0.5$. (right) χ^2 distribution in both X and Y: muons traveling a straight line through the EMR exhibit χ^2 values much lower than those produced from a showering positron.

The cut limits are determined by minimizing the Δ fitness parameter as defined by:

$$\Delta = \sqrt{\alpha_{\mu}^2 + \beta_{e^-}^2}, \tag{5.3}$$

The results are shown in the top two figures of Fig 5.2. Additionally a multivariate test was conducted shown in the bottom portion of Fig 5.2 which produces better results than either test alone. The conditions of the multivariate state are:

$$\begin{aligned} \rho > \rho_c \cap \chi^2 < \chi_c^2 \rightarrow Muon \\ \rho < \rho_c \cup \chi^2 > \chi_c^2 \rightarrow Electron/Positron \end{aligned} \tag{5.4}$$

The final analysis found that cuts of $\chi^2 = 1.6$ and $\rho = 91\%$ would yield muon losses of 0.925% and positron contamination of 1.448%.

5.3 Curve Fit Event Selection

The EMR, an excellent tool for separating decay positrons from muons, is unfortunately largely insensitive to differences between muons and pions. The following two analysis techniques then deal specifically with the PID hypothesis defined by the statistical analysis of ensemble measurements of particle behavior as beams travel the length of the MICE experiment. Traditionally this has been done through the analysis of time of flight between TOF0 $\rightarrow$ 1 and TOF1 $\rightarrow$ 2. This technique has been augmented though an effective mass reconstruction by coupling the timing data with momentum measurements from the trackers. In most beam settings this secondary analysis allows for cuts with lower expected pion contamination while delivering lower rates of muon beam loss.

5.3.1 Upstream/Downstream TOF Cuts

Particles are momentum selected when passing through the two beamline dipoles immediately before and after entering the decay solenoid. The effect of this is a separating of the average time of flight by mass between the positron, muon, pion populations. The analysis is complicated somewhat by the distribution in time between the muon and pion populations overlapping. The downstream data are further complicated over upstream measurements due to an increased path length and a significant increase in the amount of

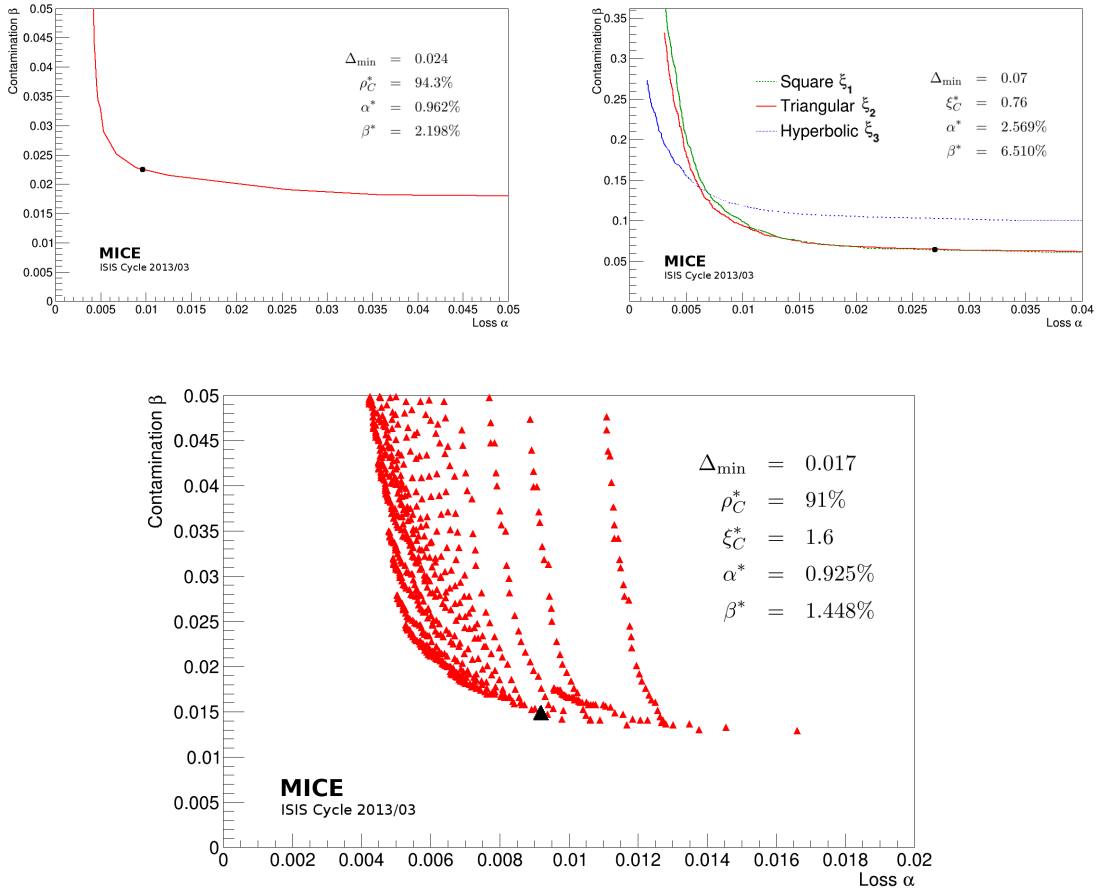

Figure 5.2: (top) The top two figures show the minimizing points in loss vs contamination space of the (left) plane density and (right) χ^2 studies. (bottom) A multivariate composition of the two studies above produces better statistics than either study alone.

material in the beam. As a result, downstream timing is particularly sensitive to long tails in the distribution that present a problem to making accurate cuts.

A solution to deal with the tails in the muon peak has been adopted through a combination Gaussian and Landau distribution. A simple Gaussian distribution is used to model the pion data. The Landau contribution is not included in this for two reasons. First the interesting region is between the muon/pion peak where the muon tail stretches out into the pion peak, the pion tail does not need to be considered. Second, the ROOT fitting routine is limited in the number of parameters it can fit in one model. Additionally no attempt is made in modeling the positron peak in the data, the separation between this peak and the muon peak is sufficient for a timing cut to be selected by eye.

The muon/pion timing cut was determined by minimizing the radial length of the parameter defined by the muon loss vs the pion contamination at a specific time of flight ($\Delta t_{i,j}$) between either set of TOFs as:

$$\Delta = \sqrt{\alpha^2_{\mu(\Delta t_{i,j})} + \beta^2_{\pi(\Delta t_{i,j})}}, \tag{5.5}$$

where α_μ defined as the muon loss takes the form:

$$\alpha_\mu = 1 - \frac{\int_{-\infty}^{\Delta t_{i,j}} (Land_\mu(\mu_L, \sigma_L, C_L, \Delta t) + Gaus_\mu(\mu_{G1}, \sigma_{G1}, C_{G1}, \Delta t))\, d\Delta t}{\int_{-\infty}^{\infty} (Land_\mu(\mu_L, \sigma_L, C_L, \Delta t) + Gaus_\mu(\mu_{G1}, \sigma_{G1}, C_{G1}, \Delta t))\, d\Delta t}, \tag{5.6}$$

and β_π, the pion contamination in the beam, is defined in a similar manner as:

$$\beta_\pi = \frac{\int_{-\infty}^{\Delta t_{i,j}} Gaus_\pi(\mu_{G2}, \sigma_{G2}, C_{G2}, \Delta t)\, d\Delta t}{\int_{-\infty}^{\Delta t_{i,j}} (Land_\mu(\mu_L, \sigma_L, C_L, \Delta t) + Gaus_\mu(\mu_{G1}, \sigma_{G1}, C_{G1}, \Delta t) + Gaus_\pi(\mu_{G2}, \sigma_{G2}, C_{G2})\, d\Delta t} \tag{5.7}$$

The Gaussian and Landau distributions are as expected:

$$Gaus = C\, e^{-\frac{1}{2}(\frac{x-\mu}{\sigma})^2} \tag{5.8}$$

$$Land = \frac{C}{\sqrt{2\pi}} e^{\frac{1}{2}(\frac{x-\mu}{\sigma} + e^{\frac{-(x-\mu)}{\sigma}})} \tag{5.9}$$

Model parameters are trained by Minuit fitting algorithm packaged in the ROOT software, and the minimization routine is preformed by the python package SciPy. An example of this process is shown in Fig 5.3

5.3.2 Effective Mass Reconstruction

An effective mass reconstruction analysis was performed. In addition to providing a sanity check in verifying that we measure the expected value of the muon, it also can provide a finer cut criterion than just the time of flight information alone. This is especially true of the downstream PID, where the time of flight is muddled by variable path length and passage through multiple materials, but the effective mass measurement benefits from the symmetry of the system. The effective mass is determined from coupling the time of flight to the momentum as measured at the tracker stations as:

$$m_{eff} = \frac{p}{\beta\gamma}, \tag{5.10}$$

where $\beta\gamma$ is determined by assuming that the average positron traverses the distance between the two TOFs at $\approx c$, so that $\bar{\beta} \approx \frac{\Delta t_e}{\Delta t_{part}}$. To simplify the calculation it is assumed that

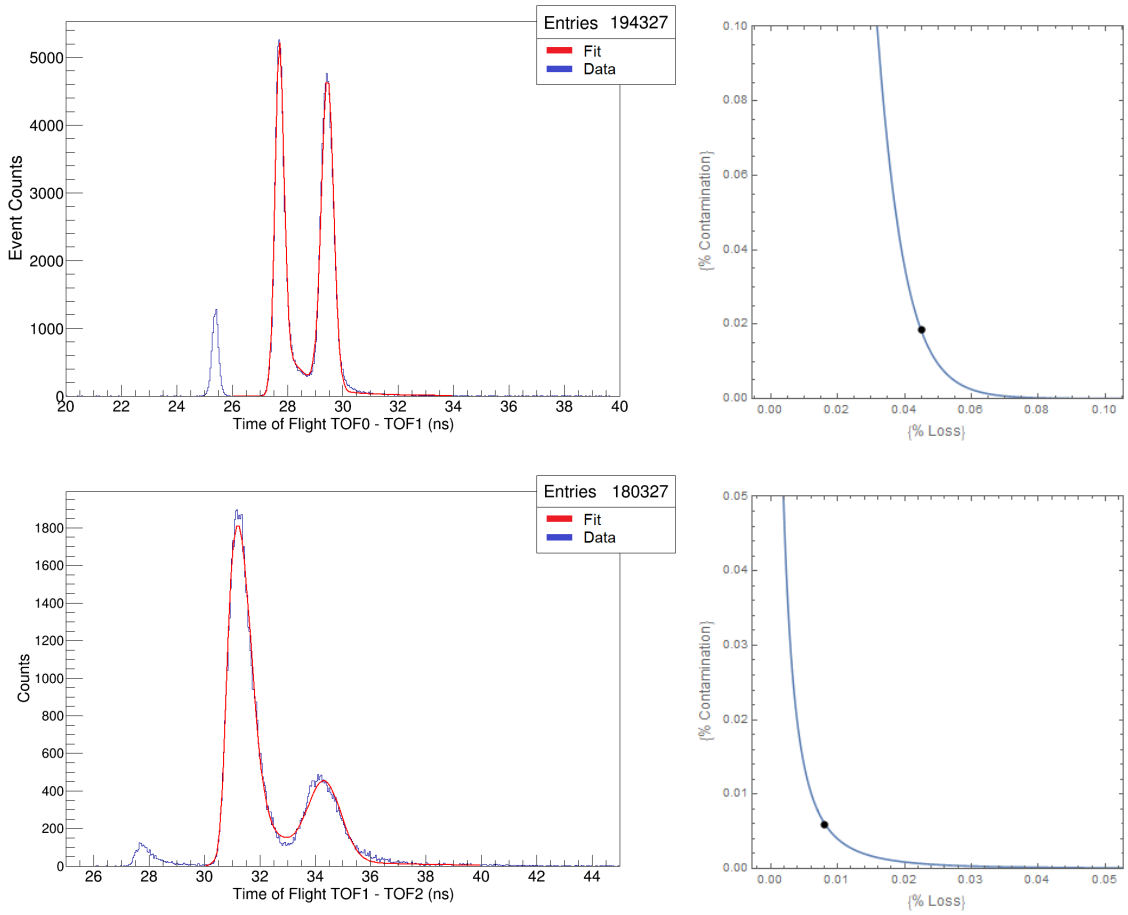

Figure 5.3: Data taken from training set for 6-200 beam setting. (Top) Upstream, TOF0 to TOF1 timing. (Bottom) Downstream, TOF1 - TOF2, timing. (Left) Plots show the total time of flight from initial to final TOF. The three clear peaks in both sets are evidence of e^+, μ, and π populations in the beam. The fit, in red, is used to identify a proper cutoff point. (Right) μ loss plotted against π contamination. The dot represents the point where both these features are minimized.

the change in velocity of the particle is negligible, which is reasonable over small distances in low density, low Z medium such as air.

Solutions for the upstream and downstream momentum in equation 5.10 are determined differently. The trackers and TOF1 - 2 are nearly symmetric about the absorber. There is a slight asymmetry due to the lack of functioning match solenoid coils downstream. But this takes place in the low Z He atmosphere of the tracker bore so the effects on the measurement are small. The average momentum recorded at the innermost stations upstream and downstream is used. Effective mass here is very near actual mass values.

Upstream, the momentum recorded at the outer upstream tracking station is traced back to the center of the TOF0 - 1 system, using the Bethe formula in air. However, the presence of the diffuser is not taken into account in this analysis. The diffuser sits between the TOFs and the tracker so that both velocity and momentum calculations are blind to it. The diffuser is a significant source of multiple scattering and shows up in two ways: first as a lowering of the effective mass and second as a leading 'tail' in the effective mass reconstruction. As the diffuser is thickened to increase the input emittance the amount of momentum loss increases. While the presence of the leading 'tail' is explained as lost momentum which creates the appearance of a secondary low mass distribution.

Analysis of the effective mass distributions follows exactly the same as performed in Eq 5.5 above. The results of this analysis and comparison to the time of flight analysis and are provided in Tables 5.2 and 5.3. The 200 MeV/c and 240 MeV/c effective mass analysis provides a cleaner cut in both muon loss (α) and pion contamination (β). A sample of the

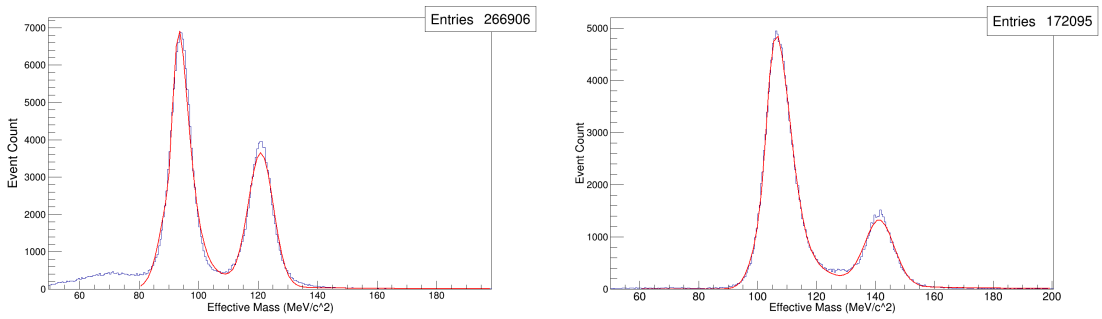

Figure 5.4: Data taken from the training set for the 6-200 beam setting. Data are shown in blue while the fit is in red. (left) The upstream effective mass distribution, the influence of the diffuser between velocity and momentum measurements shows up as a loss of momentum. (right) The downstream mass distribution benefits from the symmetry of the cooling channel and shows only slight variations above the expected m_μ and m_π values.

data for the 6-200 beam setting is shown in Fig 5.4; this can be compared to the timing data shown in Fig 5.3 above.

Effective mass is not used as a selection criteria for any of the 140 MeV/c nominal beam settings. The muon and pion mass were not able to be resolved reliably in both the upstream and downstream views. The mass reconstruction for the 3-140 analysis are shown in Fig 5.5. The complete collection of data is presented in Appx. B

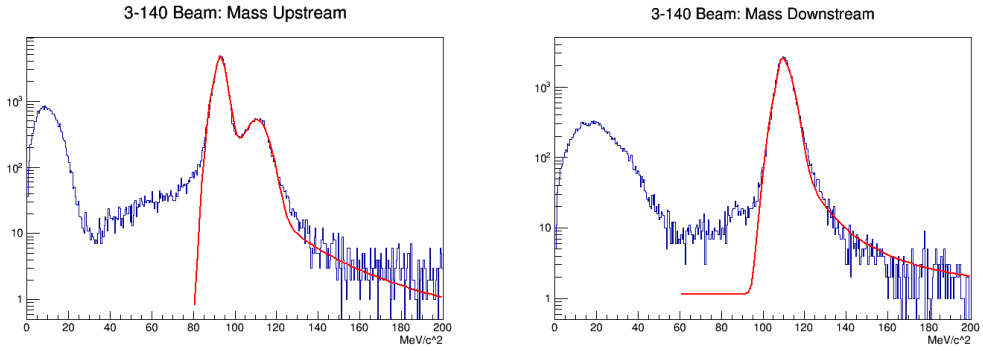

Figure 5.5: Effective mass reconstruction for the 3-140 beam setting.

			Upstream			
Beam Setting	m_μ (MeV/c^2)	m_π (MeV/c^2)	α_M (%)	α_{TOF} (%)	β_M (%)	β_{TOF} (%)
3-140	92.2	110.7	0.469	0.119	0.504	0.082
6-140	87.2	103.3	1.519	0.108	1.647	0.070
10-140	71.9	-	0	4.791	0	1.753
3-200	97.9	126.2	2.205	9.316	0.761	3.106
6-200	92.2	120.9	0.380	4.527	0.249	1.846
10-200	82.8	106.8	0.937	5.747	0.751	2.227
6-240	92.3	123.3	0.870	4.264	0.559	1.986
10-240	87.9	113.9	2.053	15.48	1.247	6.037

Table 5.2: Upstream effective mass reconstruction. No pion peak is found for the 10-240 beam setting.

		Downstream				
Beam Setting	m_μ (MeV/c^2)	m_π (MeV/c^2)	α_M (%)	α_{TOF} (%)	β_M (%)	β_{TOF} (%)
3-140	110.1	-	0	0.132	0	0.090
6-140	110.7	-	0	0.297	0	0.070
10-140	111.0	143.1	0.003	2.396	0	1.572
3-200	107.1	142.4	0.138	0.190	0.084	0.166
6-200	106.2	141.3	0.479	0.811	0.288	0.592
10-200	107.9	140.9	0.382	1.986	0.246	1.545
6-240	104.8	140.7	0.927	2.286	0.590	1.626
10-240	107.2	141.3	2.736	5.355	1.796	4.039

Table 5.3: Downstream effective mass reconstruction. No pion peak found for both the 3-140 and 6-140 beam settings.

5.4 Machine Learning Event Selection

The second analysis that was undertaken involved utilizing the open source python machine learning scikit-learn libraries[57]. First an unsupervised Gaussian mixture analysis was used to perform PID on the data along the five dimensional detector space as defined by the TOF timing and the upstream/downstream reconstructed effective masses (as defined in section 5.3.2) axis. Muon results from this process were then rotated from the four dimensional phase space (defined by: x, p_x, y, p_y) to an equivalent four dimensional orthogonal eigen-space via a principle component analysis package. A number of elliptical envelope outlier routines were then applied to the rotated data set all at different levels of effective cuts. A final emittance analysis was performed on the remaining data and compared against the curve fit analysis of section 5.3 for comparable levels of statistics (discussed in section 5.5).

5.4.1 Unsupervised Gaussian Mixture (UGM) PID

Very simply the UGM model works by drawing confidence ellipsoids about multivariate data. As discussed in the preamble to this section, the variables used in this analysis are defined by data from the MICE detectors. This model was chosen over other models because it was simple to use and implement plus it provides a metric for the particle species hypothesis according to confidence level of the model. In all cases a muon is defined by a confidence level greater than 99.9995% and corresponds to the grouping of data that has the majority of signal in the middle peak of the TOF0 $\rightarrow$ 1 timing data.

Before training the UGM model simple cuts were performed on the data. This involved sanity cuts in the TOF timing and ensuring that each data point processed had one and only one value for each axis. The effect of this shows up primarily in a reduction in the positron peak, this is because the peak timing in the positron distribution is taken as the time needed for light to travel the relevant distance. Any positron on the low side of that distribution then appears to be traveling faster than light and does not reconstruct an effective mass, and is hence cut from the analysis. The sanity cut unfortunately represents a loss of data due to a rolling over of the TOF timing circuit. A future analysis could most likely recover this data with knowledge of the bit size of the TOF ADC circuit.

With these simple cuts in place the data is prepared to begin training the UGM model. This is done by splicing the data into narrow slices along the TOF0 $\rightarrow$ 1 axis. These slices are initial best guesses as to the location of positron/muon/pion peaks in that data set. This axis was picked due to its importance as the first means of forming a particle hypothesis and because it posses the cleanest data set as particles have traveled through the least amount of material at this point in the experiment.

The five dimensional data that survives this rather harsh cut is then broken into three sets according to an initial particle hypothesis and the mean value of each of these sets in each of the 5 dimensions is sent to the model. The data is then recombined without the particle hypothesis and the data is fed into the model for training. Once the model has been developed the rest of the data that had previously been cut to form the training set, is processed by the newly formed model.

The final step of extracting a muon beam from the UGM is the imposition of a 99.9995% confidence in the model's muon hypothesis and applying the EMR cuts specified in section 5.2 (See figure 5.6). Events that pass this criteria are then collected and passed on for further analysis.

Investigating "Reach Over" in the Pion Data Set

The UGM model treats the cross over area, where neither the muon or pion area dominate, differently than in the previous analysis (section 5.3). That analysis treated the this area as a muon tail due to matter effects, The UGM analysis however, prioritizes the pion peak over the muon peak for much of this region. This inconsistency between the two models was analyzed through an examination of the downstream effective mass on the nominal momentum 200 and 240 MeV/c^2 sets. The 140 MeV/c^2 sets were excluded from the investigation due to low statistics.

The downstream effective mass has a clear peak present in the data as well as a leading tail into a lower mass region. A subtraction of the data against a Gaussian fit to the primary peak produces a dual peaked residual similar to one seen Monte Carlo simulations of MICE beam purity produced by the selection of forward versus backward decaying muons from the decay solenoid (Fig 3.5).

The relative difference between the residual peaks and the primary pion peak was compared against the expected pion decays while traveling through the experiment (Fig 5.7). It was found that the residual peaks can not completely account for expected decays over the pion time of flight (Table 5.4). This can be explained though if decaying pions

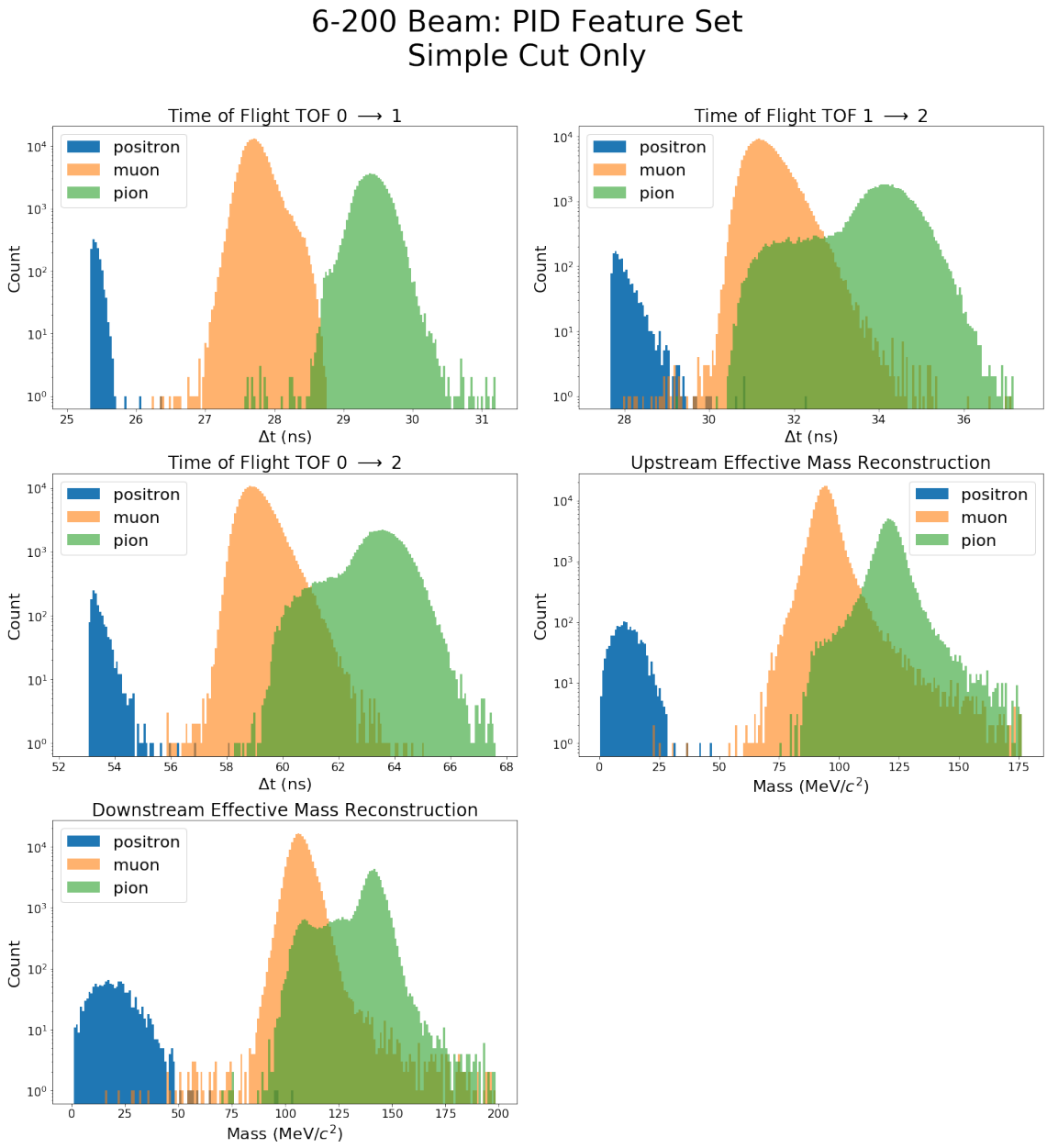

Figure 5.6: Results of PID from an unsupervised Gaussian mixture model for the 6-200 beam setting data set. Plots represent each axis used the five dimensional detector space. The positron peak in blue is truncated near the peak due to the way effective mass is calculated.

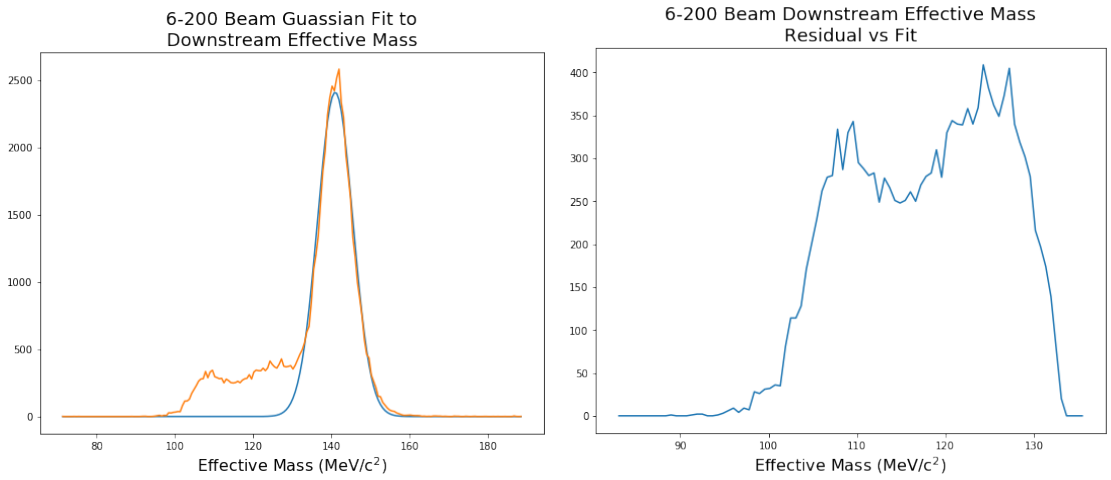

Figure 5.7: Curve fit to the effective downstream mass of the pion after UGM PID and the residual.

preferentially are predisposed to exiting the experimental volume. While it is possible to collect information on beam loss as particles travel through the experiment, MICE is not configured in such a way that performing PID on particles exiting the experiment is possible.

A splitting about an arbitrarily selected middle point in the downstream effective mass axis does however appear to lend support for the hypothesis that particles located in the cross over area are indeed muons from decayed pions and not delayed muons. Particles below the downstream mass cut-off show up firmly in the TOF0 $\rightarrow$ 1 pion peak but over time shift over to the muon peak in the TOF1 $\rightarrow$ 2 data set (Fig 5.8).

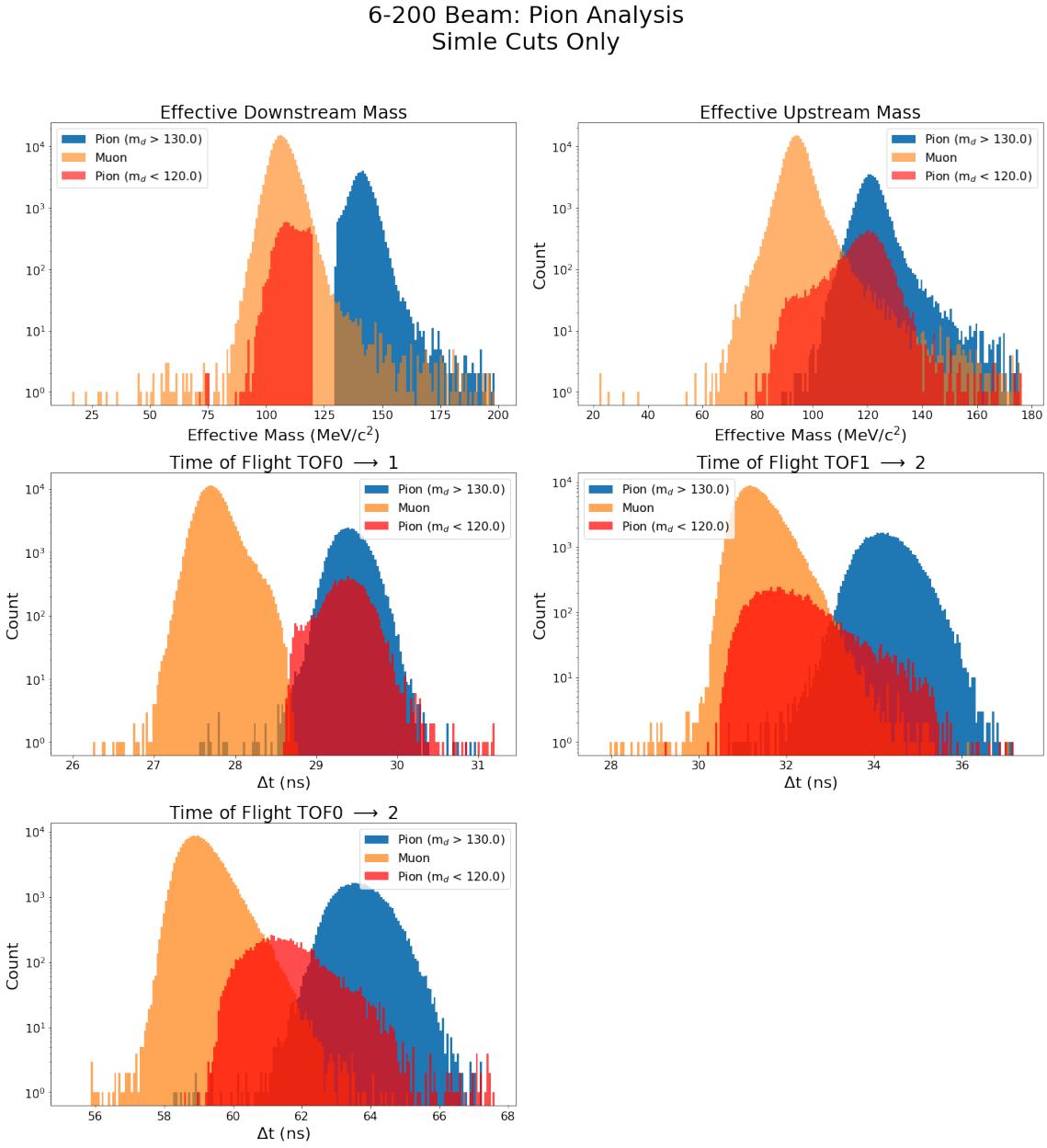

Figure 5.8: Comparison of the UGM PID pion data set against the muon data set. The pion peak is split at 120 MeV/c^2.

Beam Setting	β	Expected Remaining	Actual Remaining
3-200	0.785	43.20%	60.58%
6-200	0.809	46.10%	73.05%
6-240	0.850	51.78%	73.63%
10-200	0.796	44.56%	66.93%
10-240	0.854	52.29%	71.21%

Table 5.4: Results of investigation into pion identified particles located in 'cross over' area defined as the area between the muon and pion peaks. Analyzed under the hypothesis of pions decaying in the experiment. Shown is the percent of an original population of pion that could be expected to survive the flight from TOF1 $\rightarrow$ 2. The actual remain column is the percent of the pion data outside of the leading 'tail' as defined by the residual to the Gaussian fit to the primary peak.

5.4.2 Data Rotation and Elliptical Envelope Outlier Cuts

After the UGM PID muon tagged particle events are collected and cleaned of decay positrons that may have hidden from the UGM model through application of the EMR cuts. A final cutting of the data is performed though use of an elliptical envelope(EE) outlier routine on the four dimensional phase space coordinates (x, px, y, py) at the downstream tracker station 5. As this is the last tracker station in the experiment any non-linear effects that may be effecting particles is at its greatest measurable extent at this station, evidenced it the large growth in initial emittance measurements downstream.

A series 14 of outlier searches are performed on the data ranging from a cut that excludes only 0.25% of the data on up to a massive 30% cut on the data. The EE routine was selected for this purpose. The routine is simple, it draws a 4D ellipse about the data set such that the amount of data defined to be cut is outside the ellipse and the rest is inside. To ensure the routine is cutting for particles that are truly statistical outliers, and not just cutting data about the edge of the tracker fiducial area or at high momentum, the data is pre-processed using a principle component analysis (PCA) routine.

A PCA is a technique for diagonalizing the covariance matrix of a set of points. The data points are rotated out of the frame of a 4D phase space and into an equivalent orthogonal frame (Fig. 5.9). This process separates and highlight abnormal points in the data allowing the EE routine to cut on truly anomalous points (Fig 5.10).

Figure 5.11 shows the effect these outlier cuts have on both input emittance and the change of emittance. Low levels of cuts ($\lesssim 2.5\%$) show larger change in emittance across

absorber than loss of input emittance. An attempt is made to match the number of tagged muon events across the two event selection criteria.

5.5 Results

Emittance is calculated at each of the ten tracker stations as described by 2.2.2. The change in emittance across the absorber is defined as the fractional difference between the emittance measured in Station 1 of both trackers. These results are presented in table 5.5. The number of total events shown in the table are the total number of events that pass the requirement of one and only one event in all three TOFs and all 10 tracker stations.

The selection events were applied as follows:

- No 140 MeV/c beam uses the EMR cuts.
- Curve Fit Selection:
  - 140 MeV/c beams do not use the mass curve fits.
  - 200 and 240 MeV/c beams use both the time of flight cut and mass cut.
- Machine Learning Selection:
  - 7.50% of the data in the 10-140 beam was removed
  - 2.00% of the 10-200 beam
  - 0.25% of the 3-200 beam
  - 1.00% of the other 5 beams

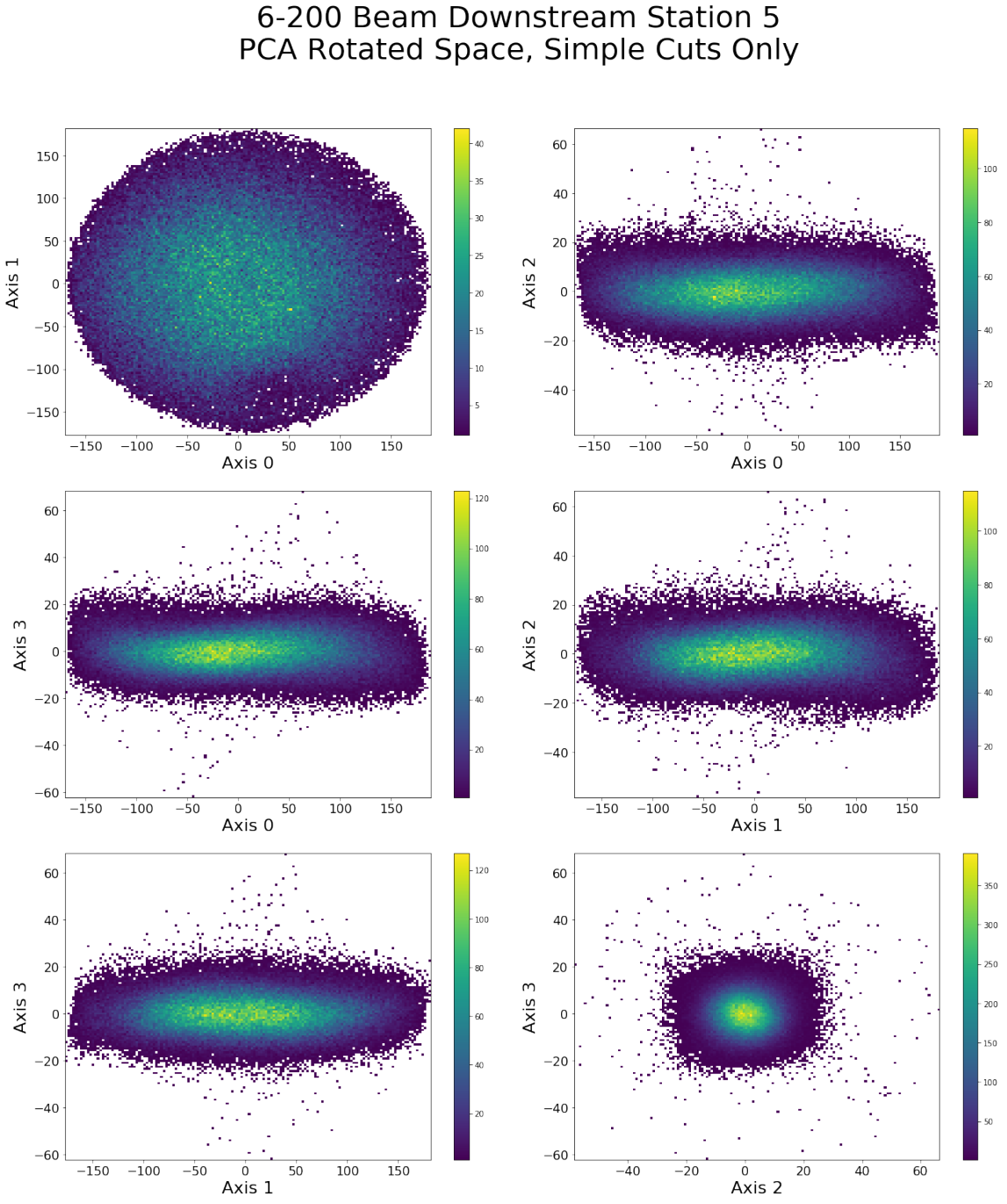

Figure 5.9: PCA rotated space generated from 4D phase space before EE cut is performed.

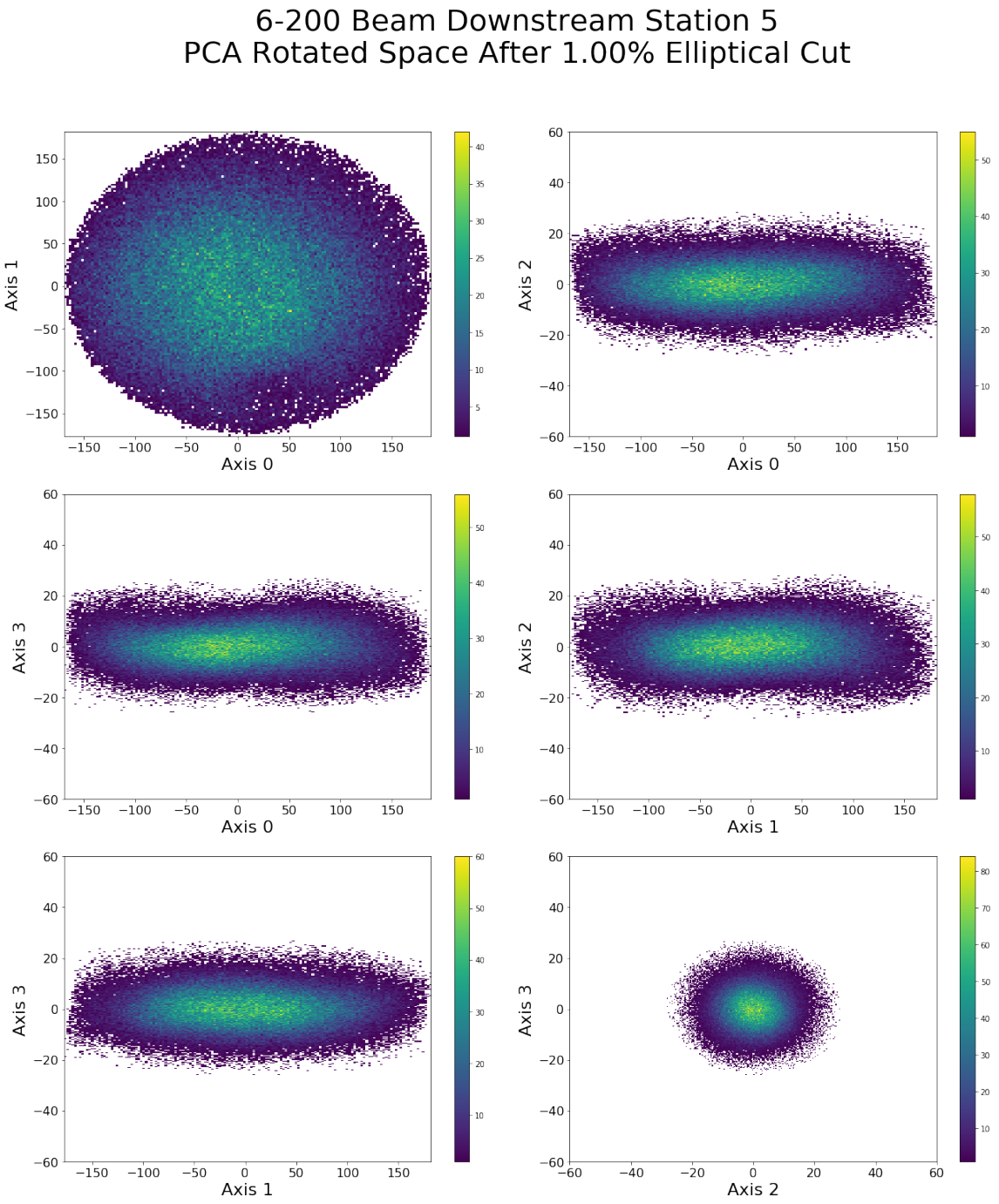

Figure 5.10: PCA rotated space after a 1% EE cut.

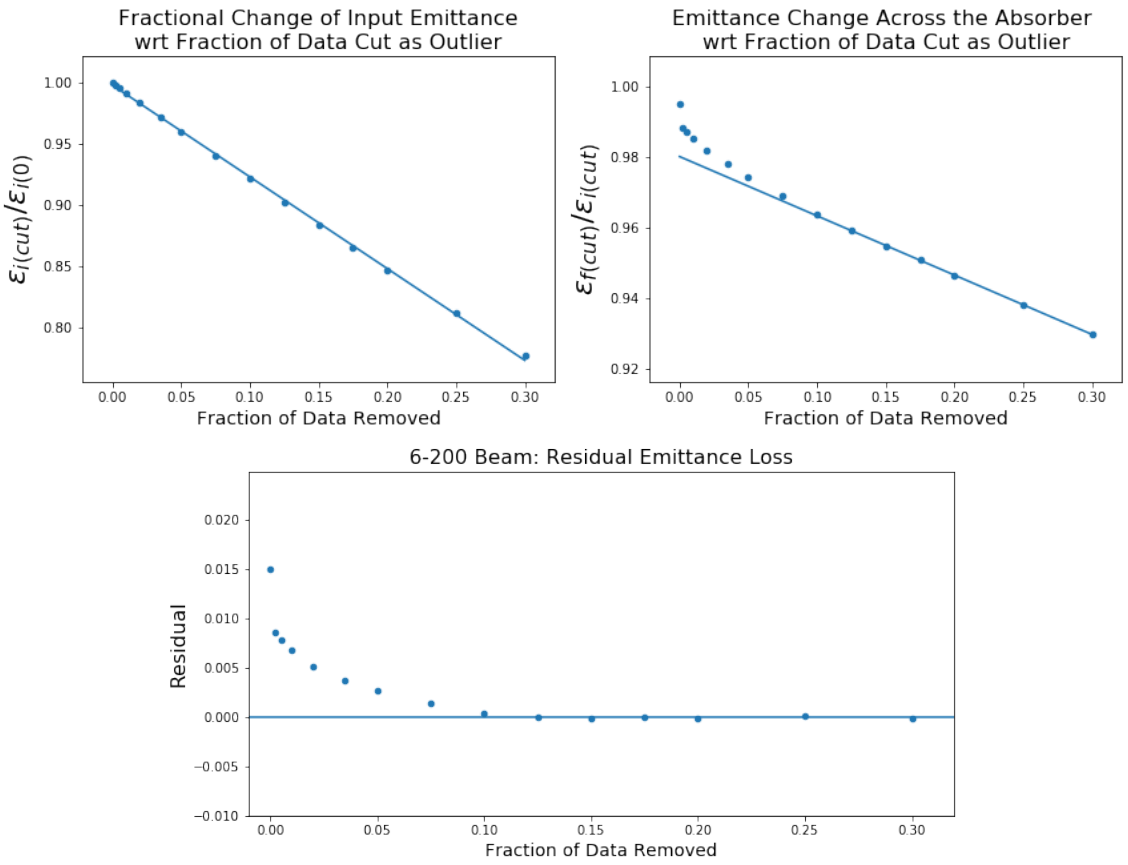

Figure 5.11: (top left) Input emittance change against fractional EE outlier cut. (top right) Change of emittance across absorber against fractional outlier cut. (bottom) Residual Change of emittance after subtracting out linear fit to cuts above 10%

The lack of EMR cuts in the 140 MeV/c beams means there may be some level of decay positron contamination in these data sets. The EMR is just not capable of producing meaningful data at such low beam energies. It may be possible to use the KL to gain some power to cull these events out of the data, but that information was not processed in time for this document.

An attempt was made to make use of only one of the curve fit cuts, either time of flight or mass reconstruction, however these two sets do not completely overlap. Cutting on only time of flight left a small pion peak in reconstructed mass just as cutting on mass left a small pion peak in time of flight. Because of this both cuts were used to tag muon events.

It is clear from these results that the Gaussian mixture event selection criteria produce a cleaner cut on the data than traditional curve fitting methods. Additionally it does this with sacrificing statistics or re-defining the input emittance of the beam. A comparison of emittance across all stations between the two methods is shown in figure 5.12, the final results across all beam settings are shown in figure 5.13. Error calculations in these plots are statistical in nature only and discussed in detail in [58].

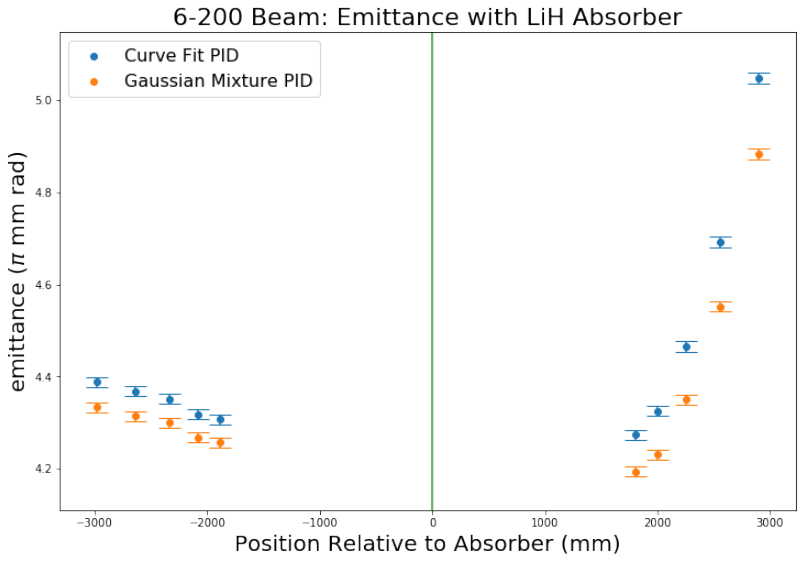

Figure 5.12: Differences in emittance across all stations using the curve fit PID and UGM PID.

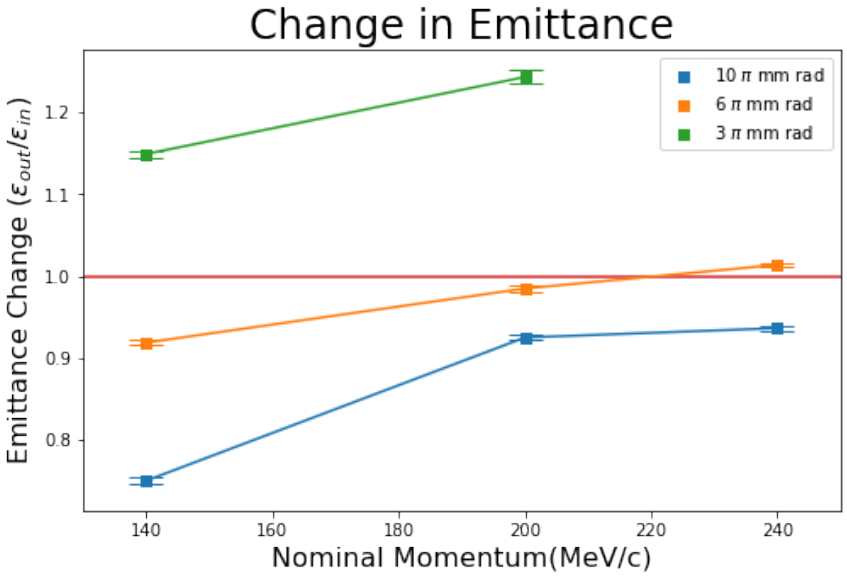

Figure 5.13: Change of emittance across absorber for all beam settings using the Gaussian mixture event selection criteria.

Nominal Beam Setting	Total Events	Curve Fit PID				UGM PID				UGM with EE Cut				
		Muon Events	$\Delta\epsilon$	ϵ_{in}	ϵ_{out}	Muon Events	$\Delta\epsilon$	ϵ_{in}	ϵ_{out}	Muon Events	$\Delta\epsilon$	ϵ_{in}	ϵ_{out}	Data Cut (%)
10-240	283387	141679	0.946	8.49	8.03	143261	0.940	8.61	8.10	141828	0.937	8.54	8.00	1.00
10-200	360425	223124	0.942	5.73	5.40	228290	0.949	5.75	5.46	223724	0.925	5.62	5.20	2.00
10-140	60748	53270	0.791	5.34	4.22	57345	0.817	5.67	4.63	53044	0.751	5.43	4.08	7.50
6-240	940255	483723	1.022	5.22	5.33	490105	1.022	5.23	5.35	485203	1.014	5.18	5.25	1.00
6-200	269750	163686	0.992	4.31	4.27	165657	0.995	4.30	4.28	164000	0.985	4.26	4.19	1.00
6-140	238846	208458	0.927	3.83	3.54	210173	0.938	3.86	3.62	208071	0.919	3.84	3.53	1.00
3-200	72377	45982	1.248	2.76	3.44	46071	1.253	2.80	3.50	45955	1.243	2.77	3.45	0.25
3-140	202476	145213	1.170	2.34	2.74	146737	1.171	2.39	2.80	145269	1.149	2.38	2.73	1.00

Table 5.5: Final results from different event selection criteria over the 8 beam settings tested.

Chapter 6

Conclusion

The Muon Ionization Cooling Experiment (MICE) in the Step IV configuration demonstrates for the first time the reduction of emittance in a muon beam. Large growth in the emittance as the particle leaves the downstream tracking volume, tends to overwhelm the final emittance measurement. Through the implementation of Kalman filtering (section 4.2.2) and outlier detection (section 5.4) this effect can be largely mitigated.

Emittance measurements, defined in section 2.2.2, are performed on eight nominal beam settings using two different event selection criteria: a curve fit criteria (section 5.3) and via an unsupervised Gaussian mixture routine coupled with an elliptical envelope outlier search (section 5.4). Both of these selection criteria were compared against one another with the Gaussian mixture routine consistently producing better results at similar statistical levels to the curve fit criteria. Further the elliptical envelope outlier detection was shown to produce results in reducing the downstream emittance growth. Evidenced in larger reduc-

tion of emittance in downstream measurements compared identical measurements upstream as shown in figure 5.11.

The final calculation using the Gaussian mixture technique and outlier detection shows emittance reduction within the statistical limits for all of the 10 π mm rad nominal emittance beams as well as the 6-140 and 6-200 beam settings.

These results corroborate the potential of using ionization cooling as a technique for beam cooling in future muon based research facilities. The next step for the collaboration is the instillation and commissioning of additional absorber modules as well as the first of the RF modules. This will allow for full test of ionization cooling under conditions similar to what will be required for these future facilities.

Appendix A

Beam Settings

All of the experimental parameters of the data sets analyzed in this document are given in this section. For each nominal beam setting the user runs examined are present in a table with the total amount of data collected. Here Total beam loss is given as a pulse weighted average of each run's beam loss.

The next two table present the beam and magnet settings used for each data run. Magnet currents are given as the average current over each run. Additionally the proton absorber (PA) thickness and diffuser (Diff) setting are provided. The data is split over two tables, the first table is the beamline settings, the second is for the cooling channel magnets.

Run Number	Date	Pulses	TOF0 Triggers	TOF1 Triggers	TOF2 Triggers	Beam Loss (V)
8734	12-05-2016	5752	1270671	256775	137896	2.343
8738		5684	1254247	253566	137003	2.385
8743	12-06-2016		C&M Not Recording			
8751		5497	1097006	222045	120659	2.094
8754		1417	284138	57402	32127	2.109
8762	12-07-2016		C&M Not Recording			
8771	12-08-2016	5668	1142198	230401	129093	2.120
Total:		24018	5048260	1020189	556778	2.230

3-140 Data Set

Run Number	Date	Pulses	TOF0 Triggers	TOF1 Triggers	TOF2 Triggers	Beam Loss (V)
8797	12-09-2016	5643	1759936	393786	76008	1.847
8798		5495	1872188	419821	81060	2.011
8799		567	129484	28833	5744	1.443
8816		5545	1782433	399124	79577	1.903
Total:		17250	5544041	1241564	242389	1.904

3-200 Data Set

Run Number	Date	Pulses	TOF0 Triggers	TOF1 Triggers	TOF2 Triggers	Beam Loss (V)
8736	12-05-2016	4773	1235697	281492	112076	2.500
8739		5582	1386652	315176	125278	2.366
8744	12-06-2016	5520	1408571	320501	128905	2.432
8752		5510	1248279	283656	112137	2.124
8755	12-07-2016	1716	398896	90346	37787	2.155
8761			C&M Not Recording			
8772	12-08-2016	5433	1171732	265974	111376	2.013
8775		5545	1311354	298346	121845	2.201
Total:		34079	8161181	1855491	749404	2.262

6-140 Data Set

Run Number	Date	Pulses	TOF0 Triggers	TOF1 Triggers	TOF2 Triggers	Beam Loss (V)
8794	12-09-2016	5650	1810156	546839	295979	1.686
8795		5647	1935411	584294	316870	1.798
8796		2377	806459	243452	131667	1.801
Total:		13674	4552026	1374585	744516	1.752

6-200 Data Set

Run Number	Date	Pulses	TOF0 Triggers	TOF1 Triggers	TOF2 Triggers	Beam Loss (V)
8873	12-12-2016	4293	2129985	704140	387050	2.000
8874		4280	2118105	699568	385159	1.962
8875		622	264612	87850	48240	2.291
8877	12-13-2016	4391	2119339	698513	383877	1.979
8878		4185	2088178	688588	378382	2.001
8879		4208	1983443	653999	359764	1.937
8880		4312	2103815	693424	380751	1.976
8881		4133	2007051	662340	363291	4.429
8882		2609	1382187	457551	251623	2.123
Total:		33033	16196715	5345973	2938137	2.300

6-240 Data Set

Run Number	Date	Pulses	TOF0 Triggers	TOF1 Triggers	TOF2 Triggers	Beam Loss (V)
8740	12-06-2016	5619	2110467	535769	77052	2.546
8753		5762	1889310	478483	70546	2.135
8756	12-07-2016	5773	2037677	515878	80181	2.298
8759			C&M Not Recording			
8760			C&M Not Recording			
8773	12-08-2016	5608	1695638	428987	66829	1.996
Total:		22762	7733092	1959117	294608	2.243

10-140 Data Set

Run Number	Date	Pulses	TOF0 Triggers	TOF1 Triggers	TOF2 Triggers	Beam Loss (V)
8817	12-09-2016	1197	409151	129581	39216	1.458
8818		1739	693099	221639	66612	1.653
8819		646	278105	88590	26173	1.821
8820		1473	551151	175874	52232	1.653
8821		5164	994550	317979	94845	4.494
8822		4120	1836971	586739	173594	1.920
8823	12-10-2016	5694	2565573	819341	243505	1.952
8824		4383	2053059	657808	194853	1.985
8826		5627	2736104	875025	257790	2.056
8828		1756	902255	289617	85729	2.184
Total:		31799	13020018	416193	1234549	2.345

10-200 Data Set

Run Number	Date	Pulses	TOF0 Triggers	TOF1 Triggers	TOF2 Triggers	Beam Loss (V)
8907	12-13-2016	227	124455	45658	14589	3.035
8908		3575	1905571	703679	224373	2.590
8914		6131	3367232	1239866	395903	2.446
8915		5587	3203429	1177212	377260	2.371
8917	12-14-2016	1386	769821	283394	90479	2.322
Total:		16906	9370508	3449809	1102604	2.450

10-240 Data Set

Nominal Beam	Diff	PA (mm)	D1 (A)	D2 (A)	DS (A)
3-140	0	29	142.66	69.99	311.11
3-200	0	29	180.70	94.92	395.38
6-140	4	29	153.01	76.40	323.86
6-200	3	29	202.91	98.00	418.14
6-240	8	49	230.24	110.00	498.48
10-140	15	29	170.01	85.00	371.75
10-200	15	29	214.01	108.02	454.99
10-240	15	49	250.04	119.99	516.38

Beamline settings (sans quadrupoles) for each nominal beam

Nominal Beam	Q1 (A)	Q2 (A)	Q3 (A)	Q4 (A)	Q5 (A)	Q6 (A)	Q7 (A)	Q8 (A)	Q9 (A)
3-140	48.01	59.90	41.61	131.27	175.99	116.66	110.77	167.49	142.88
3-200	60.77	75.87	52.74	159.45	213.87	141.77	70.03	105.99	90.45
6-140	50.06	62.50	43.39	133.95	179.63	119.02	113.68	171.87	146.60
6-200	64.38	80.33	55.80	171.54	230.10	152.53	152.39	230.57	196.92
6-240	76.52	95.56	66.43	203.72	273.24	181.18	184.54	279.25	238.63
10-140	57.23	71.41	49.60	152.78	204.86	135.83	99.96	113.36	129.02
10-200	69.98	87.37	60.70	186.27	249.89	165.71	150.53	227.04	194.40
10-240	79.28	99.04	68.85	211.04	283.12	187.78	143.89	217.73	186.02

Quadrupole beamline settings for each nominal beam

Nominal Beam	FCU-C (A)	SSU-E2 (A)	SSU-E1 (A)	SSU-M2 (A)	SSU-M1 (A)	SSU-C (A)
3-140	55.20	208.00	208.00	187.42	178.07	208.00
3-200	56.20	208.01	208.00	172.91	239.21	208.01
6-140	55.20	208.00	208.00	187.42	178.07	208.00
6-200	56.20	208.01	208.00	172.91	239.21	208.01
6-240	78.79	208.00	208.00	193.12	177.68	208.00
10-140	55.20	208.00	208.00	187.42	178.07	208.00
10-200	56.20	208.00	208.00	172.91	239.21	208.00
10-240	78.79	208.00	208.00	193.12	177.68	208.00

Upstream cooling channel magnet settings for each nominal beam.

Nominal Beam	SSD-E1 (A)	SSD-E2 (A)	SSD-M2 (A)	SSD-M1 (A)	SSD-C (A)
3-140	208.01	208.00	0.00	0.00	208.00
3-200	208.00	208.00	0.00	0.00	208.00
6-140	208.01	208.00	0.00	0.00	208.00
6-200	208.00	208.00	0.00	0.00	208.00
6-240	207.99	207.99	0.00	0.00	207.99
10-140	208.01	208.01	0.00	0.00	208.01
10-200	208.00	208.00	0.00	0.00	208.00
10-240	207.99	207.99	0.00	0.00	207.99

Downstream cooling channel magnet settings for each nominal beam.

Appendix B

Curve Fit Analysis

Presented here is all the fits used in the curve fit PID analysis. The fit is carried out as outlined in section 5.3, represented by the red line on the plots. You can see in all of the nominal 140 MeV/c setting that pion mass does not reconstruct reliably. Curve fits are not over complete data sets, a single run from each beam setting.

Additionally cuts were much less lose than normal analysis, allowing for multiple reconstructed data points for each plot. For example, allow for TOF0 to have three recorded time in a single particle event and TOF1 to have two recorded times. This situation will produce the six possible permutations for time of flight in this analysis. Finally unlike the emittance measurement analysis incomplete data sets can be used. A particle event with no TOF2 measurement will still reconstruct upstream timing and mass measurements.

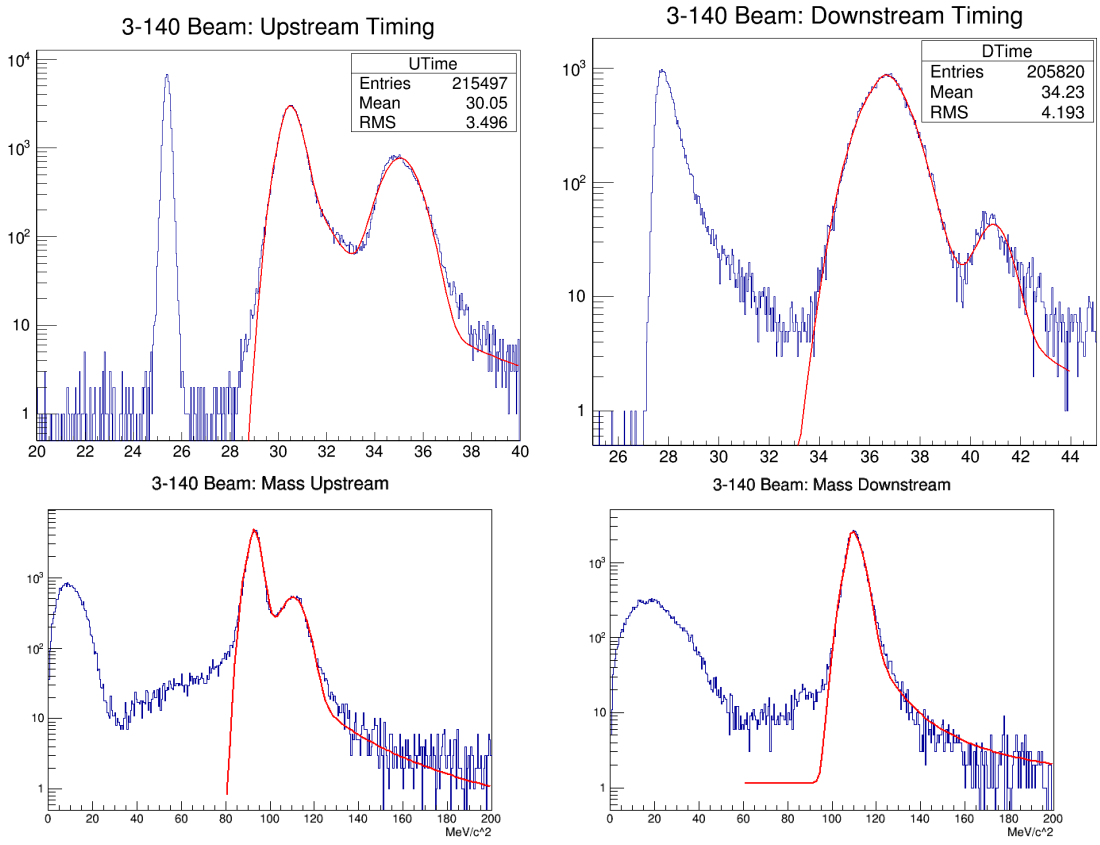
3-140 Beam: Upstream Timing
UTime
Entries 215497
Mean 30.05
RMS 3.496
3-140 Beam: Downstream Timing
DTime
Entries 205820
Mean 34.23
RMS 4.193
3-140 Beam: Mass Upstream
3-140 Beam: Mass Downstream
MeV/c^2
MeV/c^2

3-140 Beam

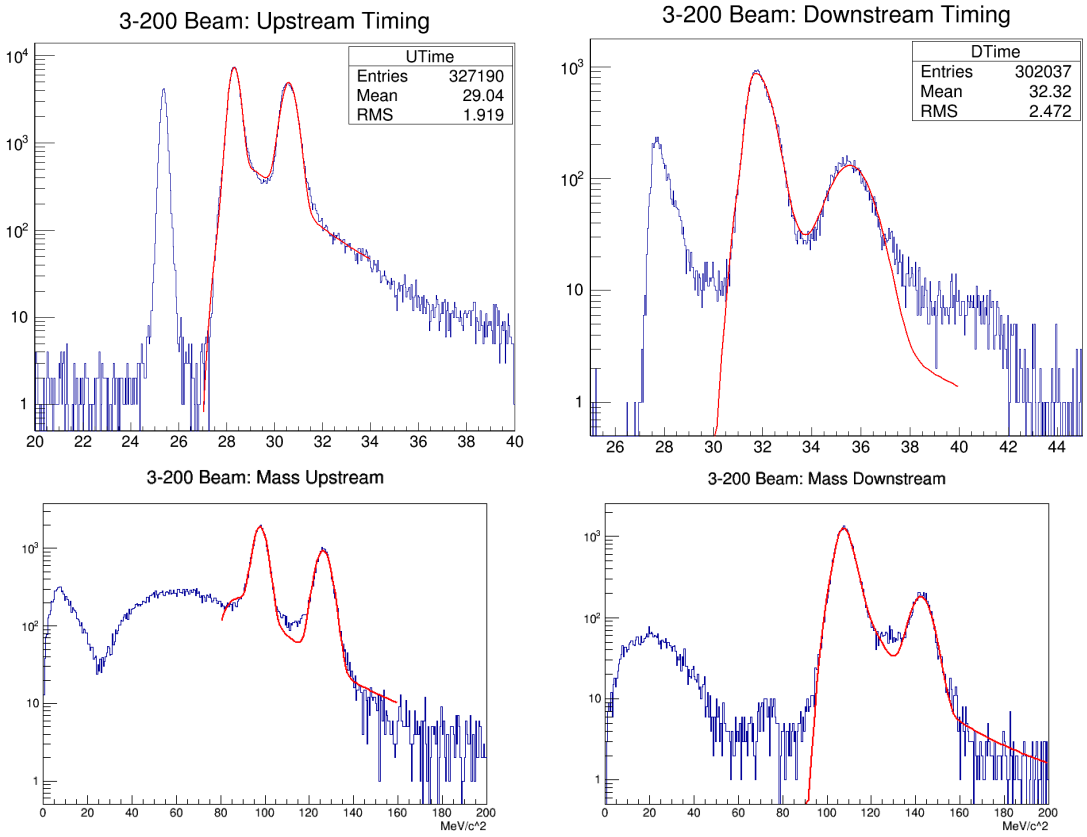
3-200 Beam: Upstream Timing
UTime
Entries 327190
Mean 29.04
RMS 1.919
3-200 Beam: Downstream Timing
DTime
Entries 302037
Mean 32.32
RMS 2.472
3-200 Beam: Mass Upstream
MeV/c^2
3-200 Beam: Mass Downstream
MeV/c^2

3-200 Beam

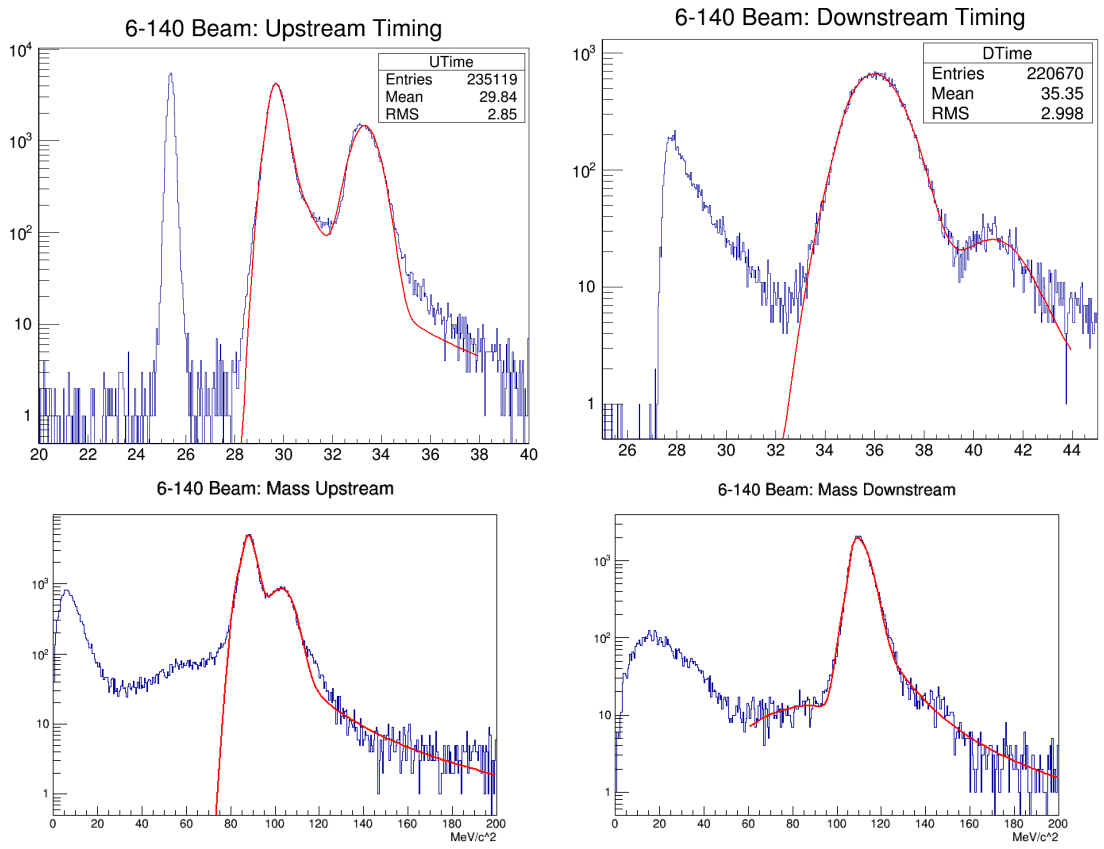
6-140 Beam: Upstream Timing
UTime
Entries 235119
Mean 29.84
RMS 2.85
6-140 Beam: Downstream Timing
DTime
Entries 220670
Mean 35.35
RMS 2.998
6-140 Beam: Mass Upstream
MeV/c^2
6-140 Beam: Mass Downstream
MeV/c^2

6-140 Beam

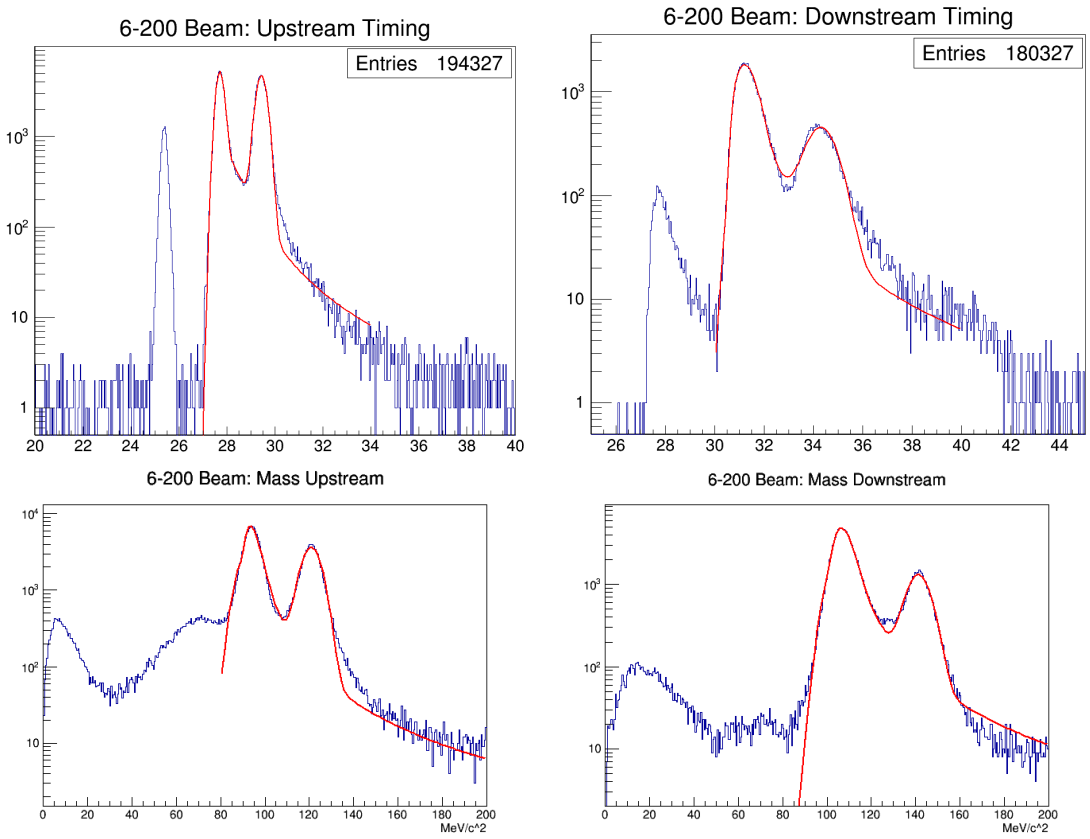
6-200 Beam: Upstream Timing
Entries 194327
6-200 Beam: Downstream Timing
Entries 180327
6-200 Beam: Mass Upstream
6-200 Beam: Mass Downstream
MeV/c^2
MeV/c^2

6-200 Beam

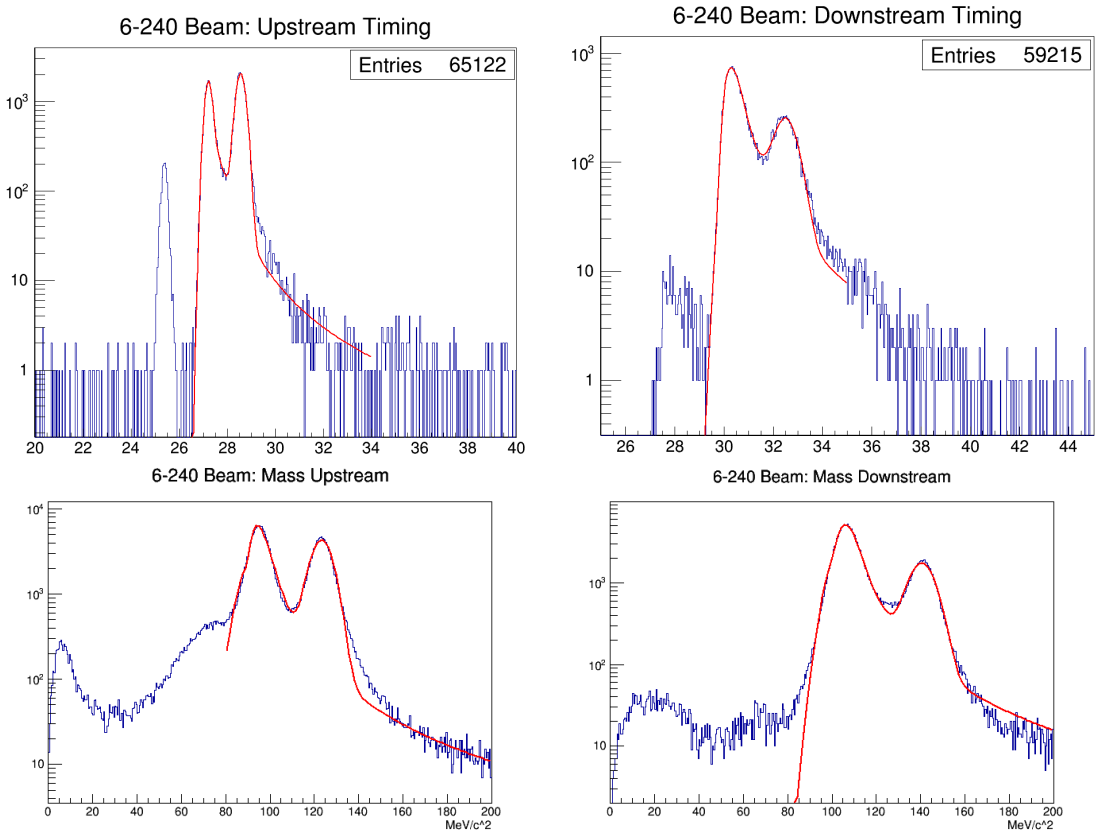
6-240 Beam: Upstream Timing
Entries 65122
6-240 Beam: Downstream Timing
Entries 59215
6-240 Beam: Mass Upstream
6-240 Beam: Mass Downstream
MeV/c^2
MeV/c^2

6-240 Beam

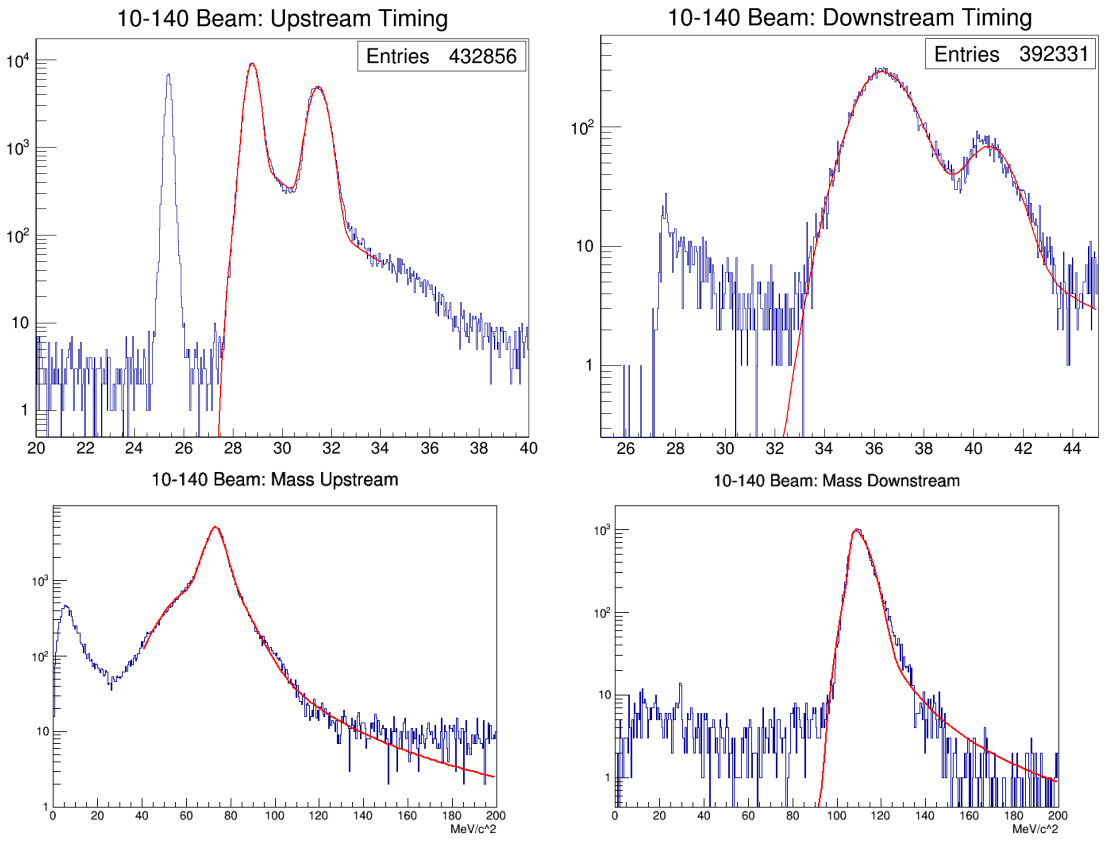
10-140 Beam: Upstream Timing
Entries 432856
10-140 Beam: Downstream Timing
Entries 392331
10-140 Beam: Mass Upstream
10-140 Beam: Mass Downstream
MeV/c^2
MeV/c^2

10-140 Beam

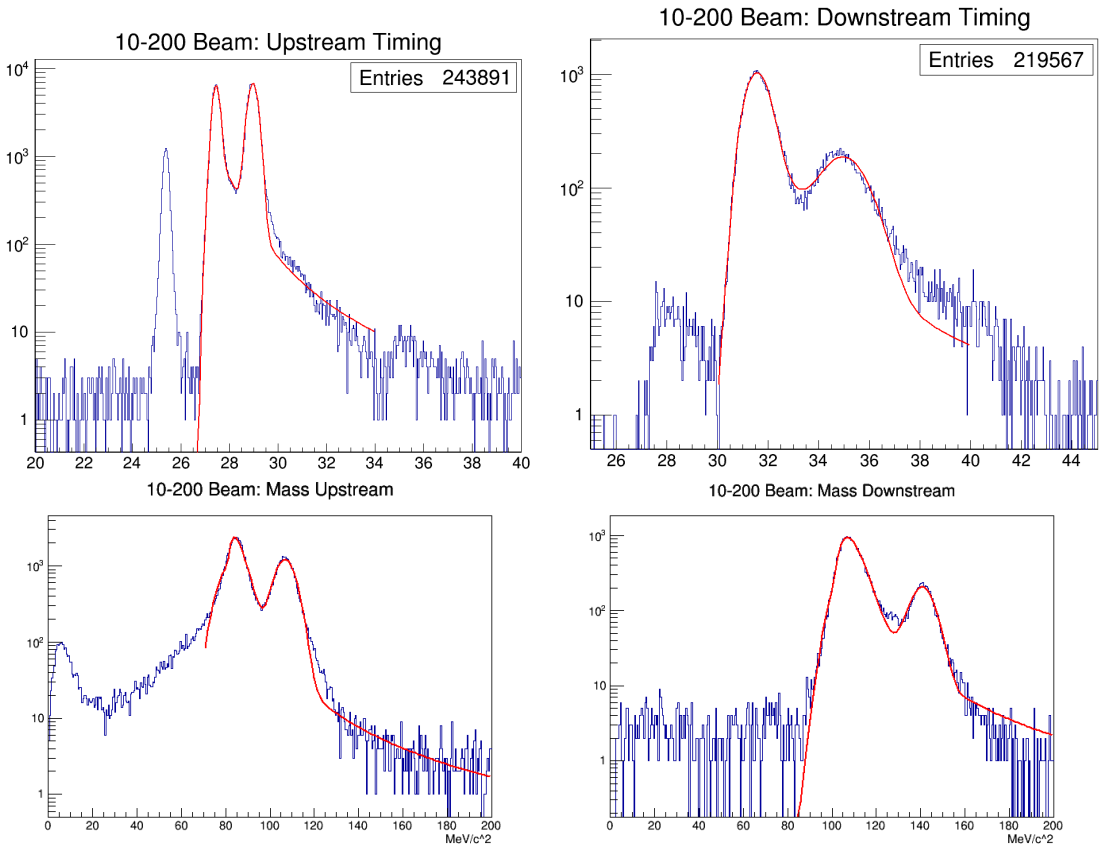
10-200 Beam: Upstream Timing
Entries 243891
10-200 Beam: Downstream Timing
Entries 219567
10-200 Beam: Mass Upstream
10-200 Beam: Mass Downstream
MeV/c^2
MeV/c^2

10-200 Beam

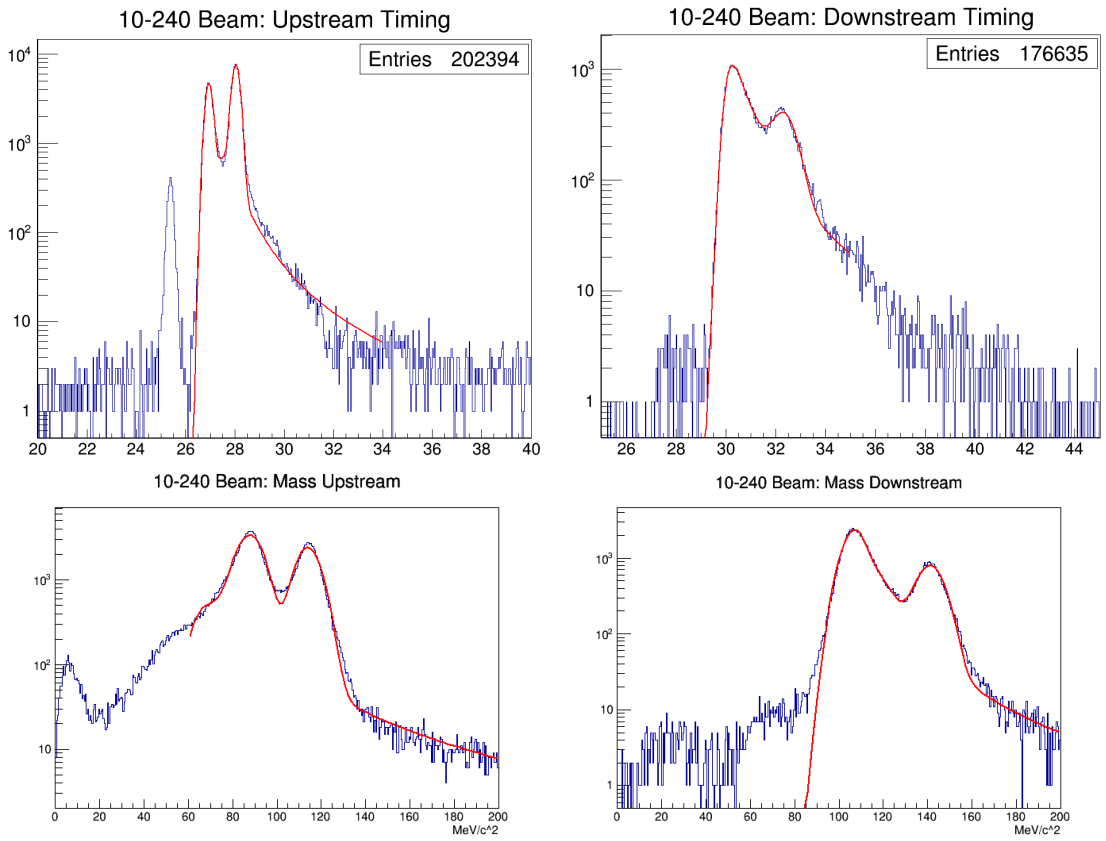
10-240 Beam: Upstream Timing
Entries 202394
10-240 Beam: Downstream Timing
Entries 176635
10-240 Beam: Mass Upstream
10-240 Beam: Mass Downstream
MeV/c^2
MeV/c^2

10-240 Beam

Appendix C

Unsupervised Gaussian Mixture

Presented here is the results from the UGM PID search. The first set of plots show the raw data read in for analysis. The term 'Simple Cuts' on these plots refer to some sanity cuts performed before PID. the PID plots shown do not include the EMR cut which is performed after this step.

The next set of plots is the analysis of the effects of the elliptical envelope outlier cut on emittance measurements. Error in emittance is given by

$$\sigma_{\epsilon_\perp} = \frac{\epsilon_\perp}{\sqrt{N}}. \tag{C.1}$$

Emittance calculations are carried out as shown in section 2.2.2. Two sets of plots are shown for each beam setting: first, the effect of the EE cuts on the emittance and second, a side-by-side comparison of the emittance calculation for the final EE cut against the emittance produced by the curve fit cut.

3-140 Beam: Raw Feature Set
Simple Cut Only

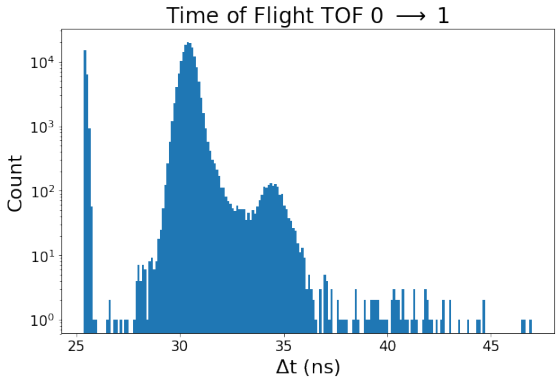

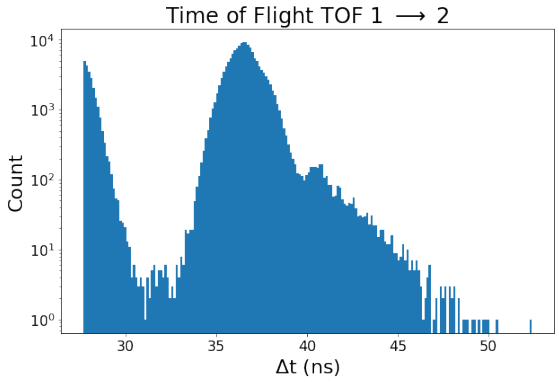

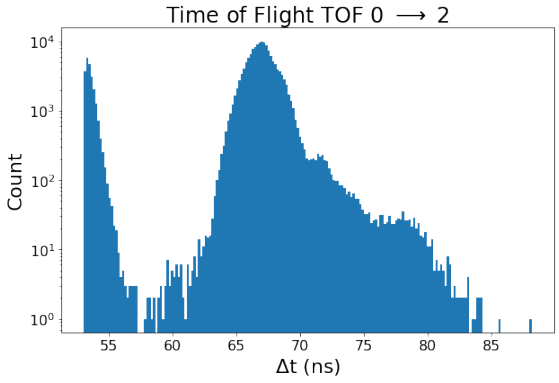

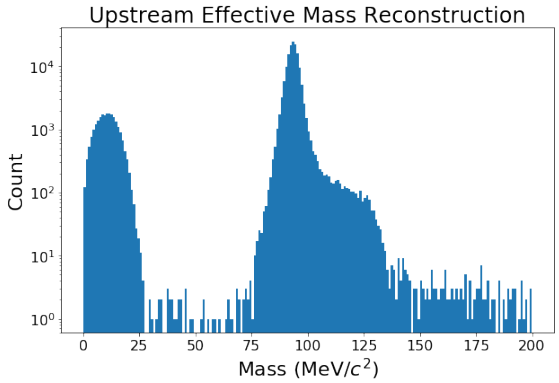

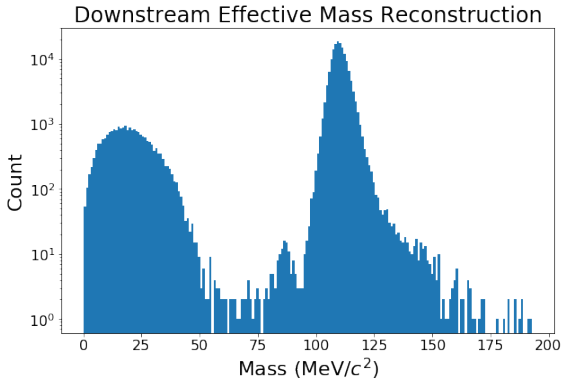

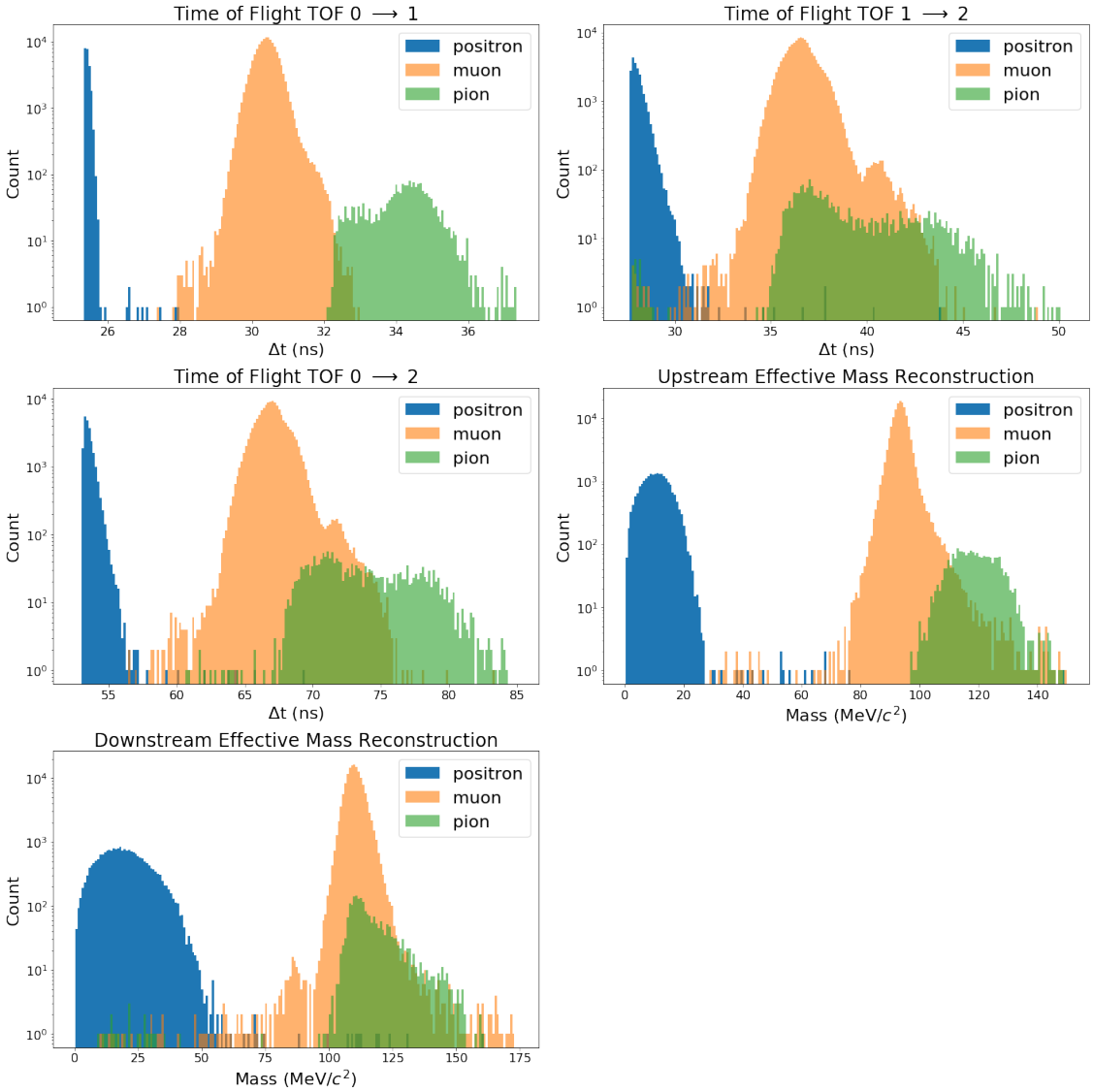
3-140 Beam: PID Feature Set
Simple Cut Only
Time of Flight TOF 0 ⟶ 1
Time of Flight TOF 1 ⟶ 2
Time of Flight TOF 0 ⟶ 2
Upstream Effective Mass Reconstruction
Downstream Effective Mass Reconstruction
positron
muon
pion
Count
Δt (ns)
Mass (MeV/c^2)

3-200 Beam: Raw Feature Set
Simple Cut Only

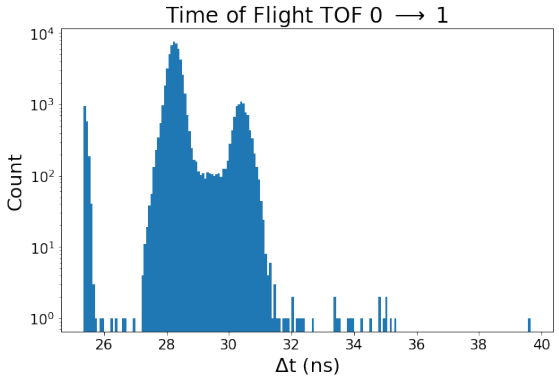

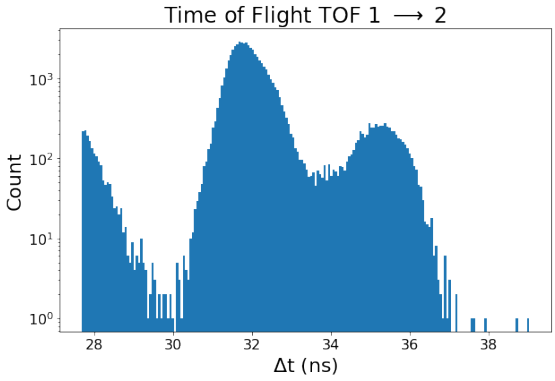

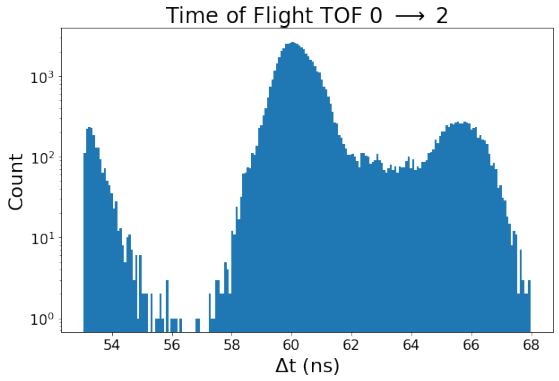

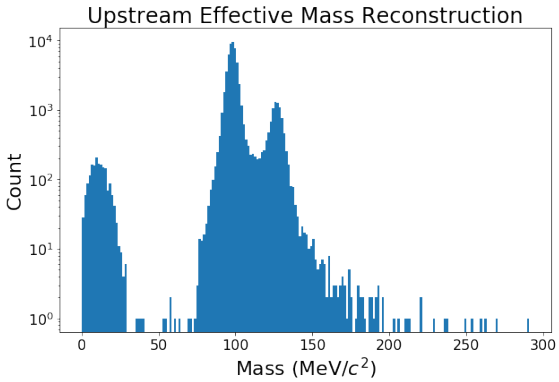

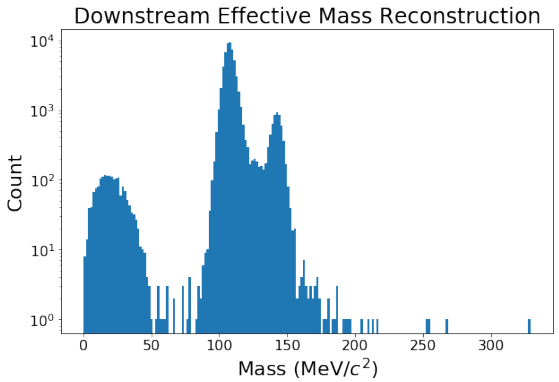

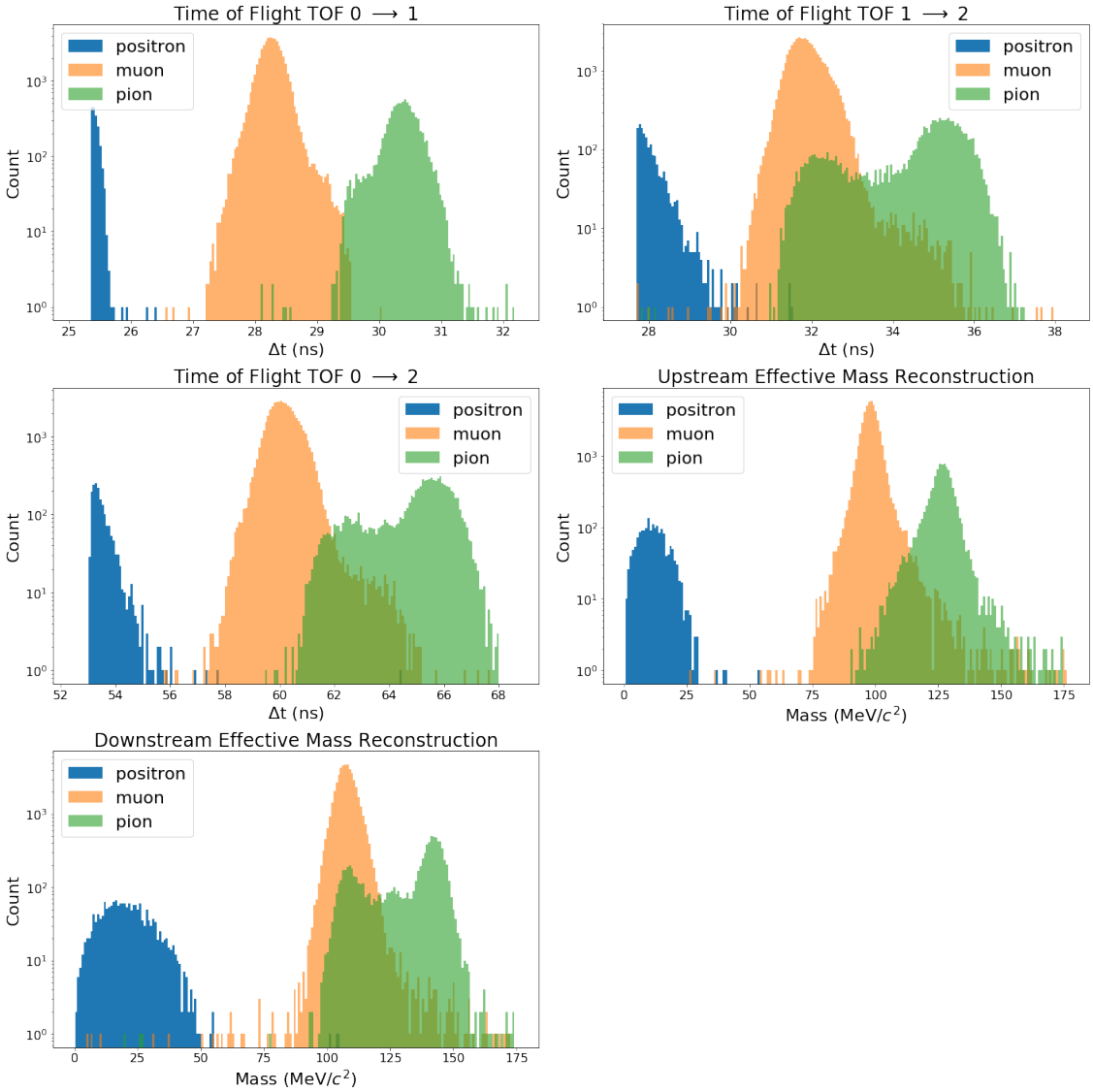
3-200 Beam: PID Feature Set
Simple Cut Only
Time of Flight TOF 0 ⟶ 1
positron
muon
pion
Count
Δt (ns)
Time of Flight TOF 1 ⟶ 2
positron
muon
pion
Count
Δt (ns)
Time of Flight TOF 0 ⟶ 2
positron
muon
pion
Count
Δt (ns)
Upstream Effective Mass Reconstruction
positron
muon
pion
Count
Mass (MeV/c^2)
Downstream Effective Mass Reconstruction
positron
muon
pion
Count
Mass (MeV/c^2)

6-140 Beam: Raw Feature Set
Simple Cut Only

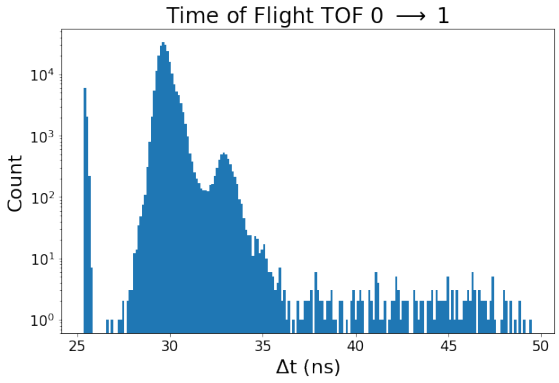

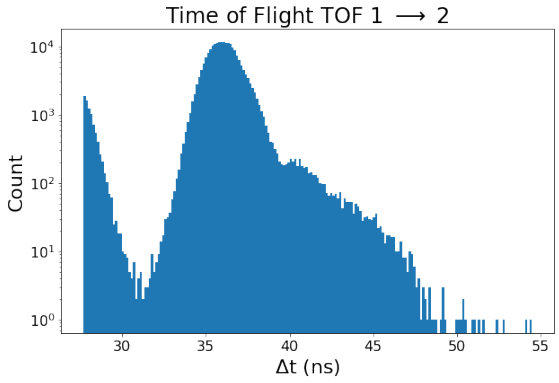

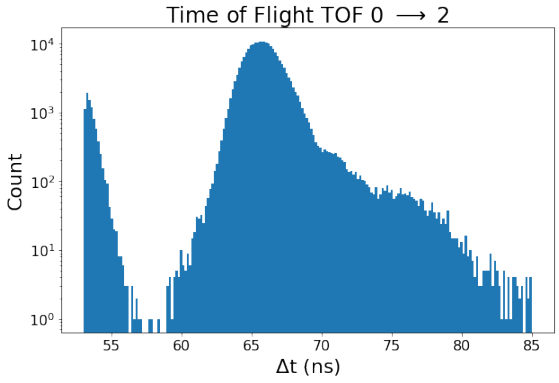

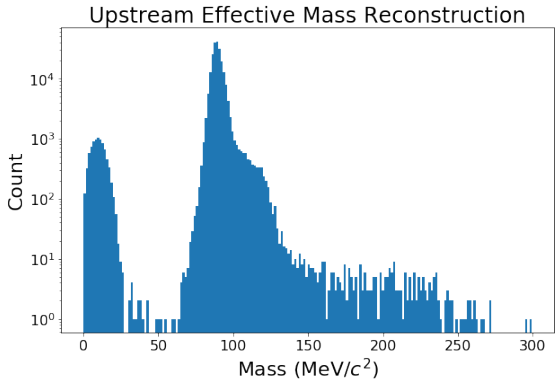

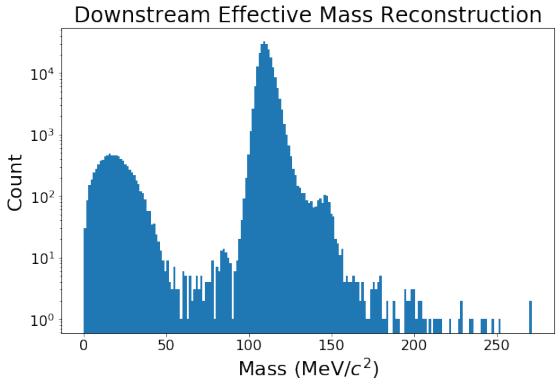

6-140 Beam: PID Feature Set
Simple Cut Only

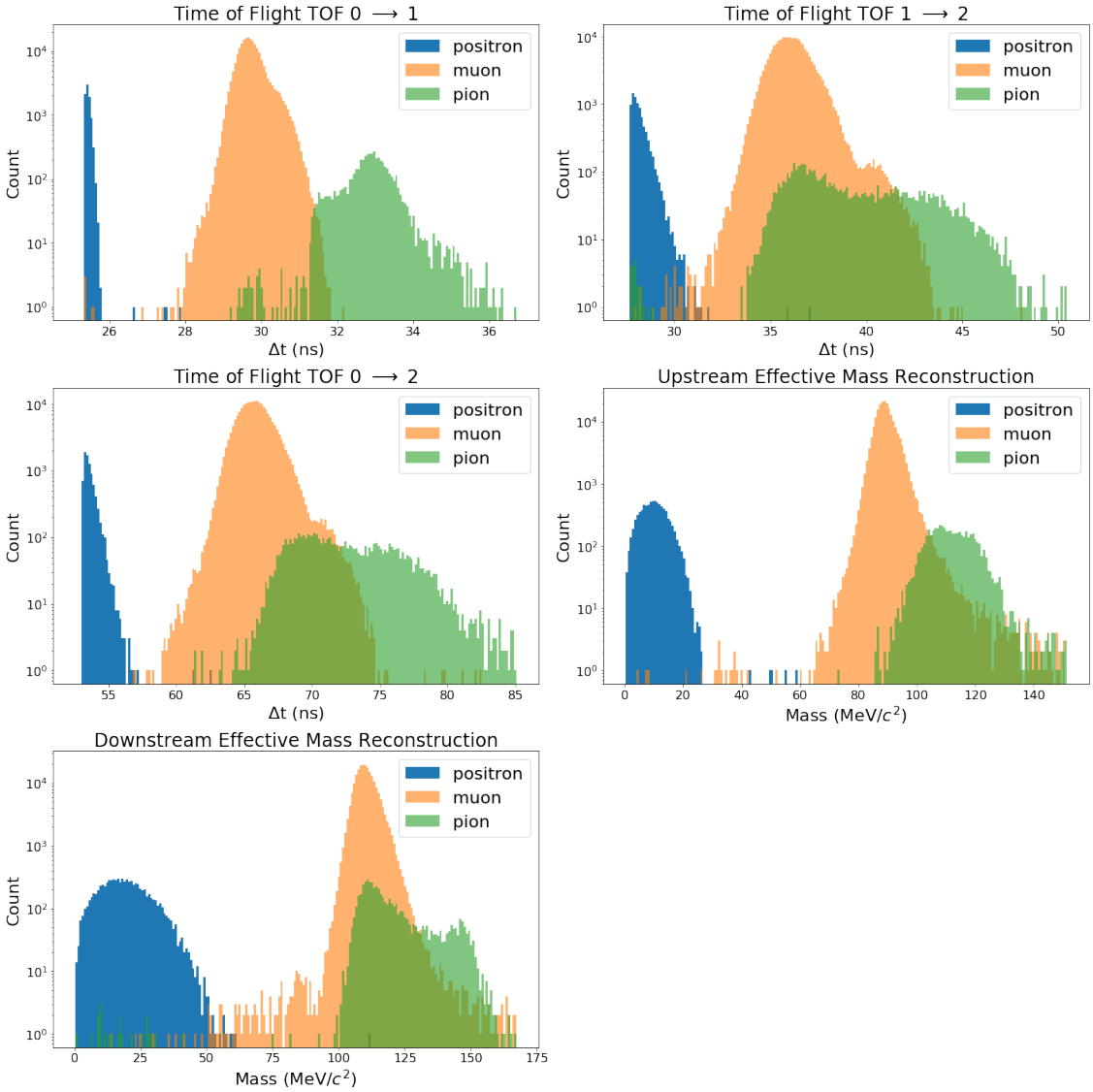

6-200 Beam: Raw Feature Set
Simple Cut Only

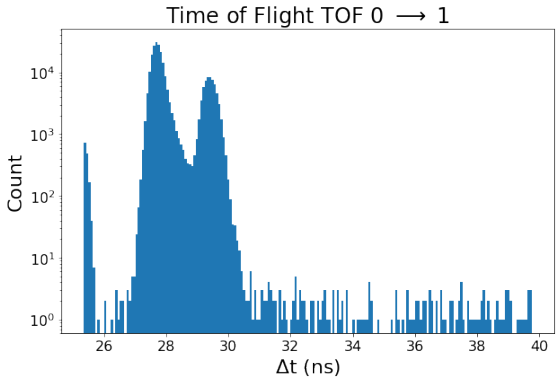

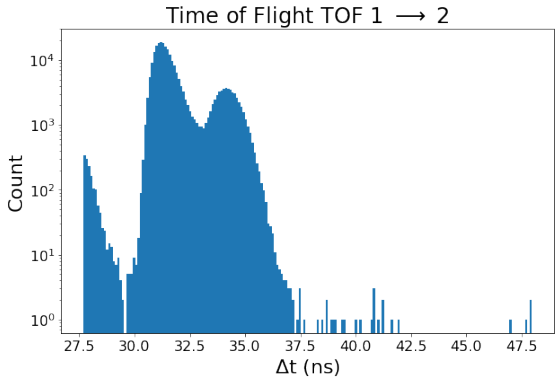

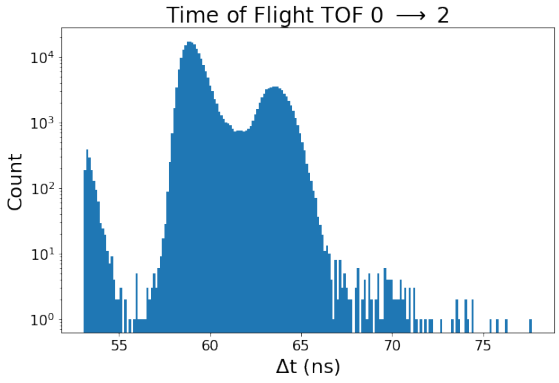

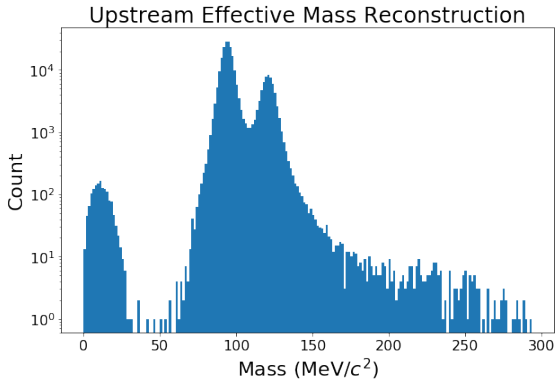

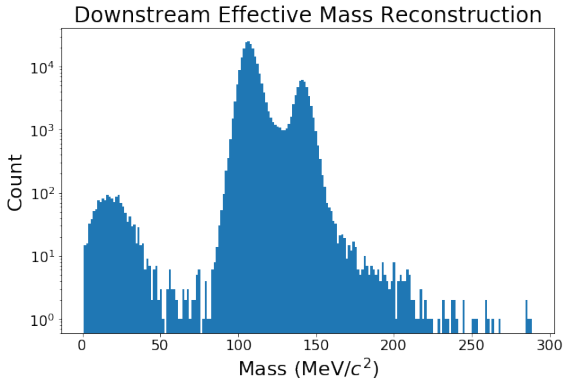

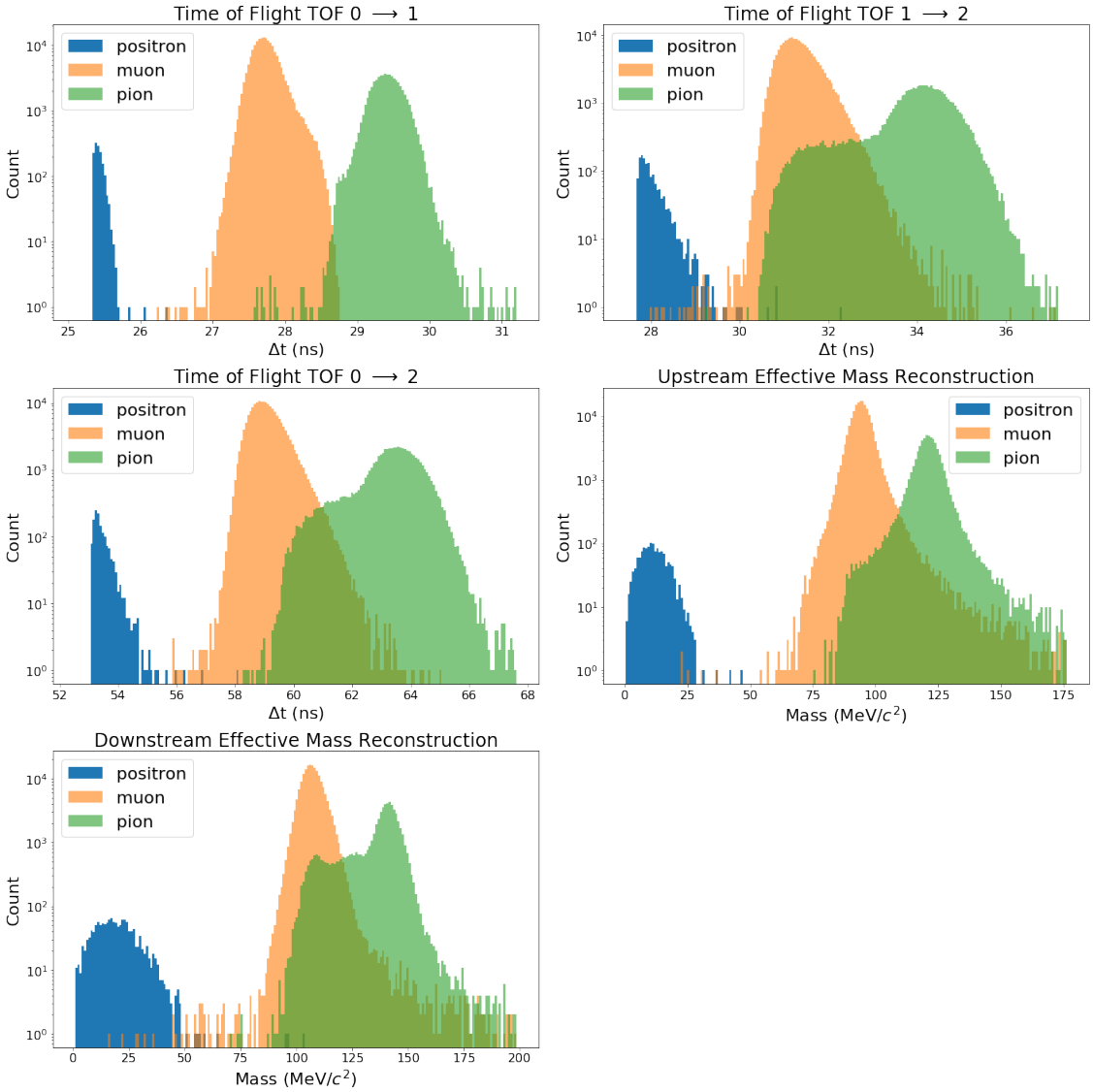
6-200 Beam: PID Feature Set
Simple Cut Only
Time of Flight TOF 0 ⟶ 1
Time of Flight TOF 1 ⟶ 2
Time of Flight TOF 0 ⟶ 2
Upstream Effective Mass Reconstruction
Downstream Effective Mass Reconstruction
positron
muon
pion
Count
Δt (ns)
Mass (MeV/c^2)

6-240 Beam: Raw Feature Set
Simple Cut Only

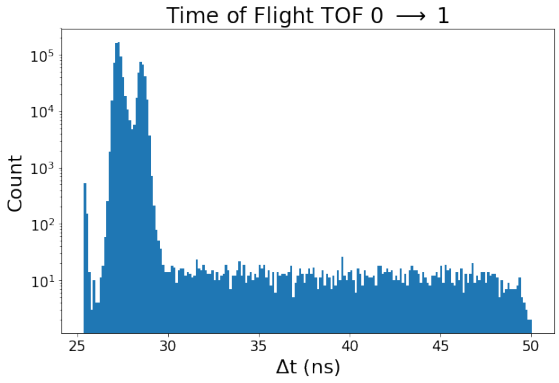

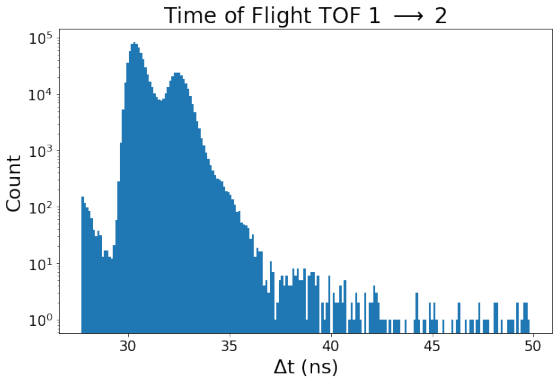

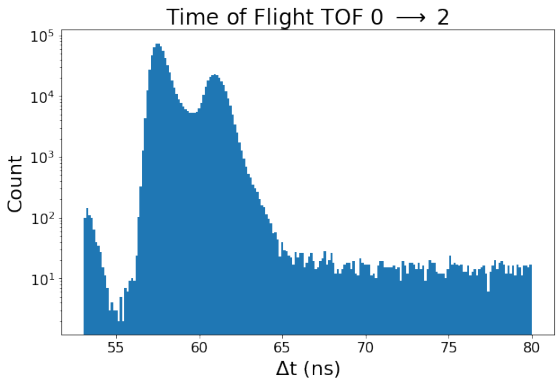

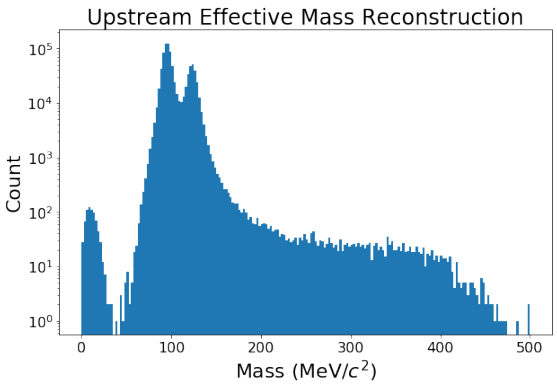

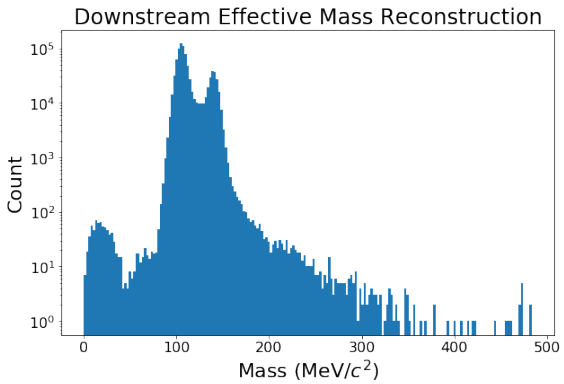

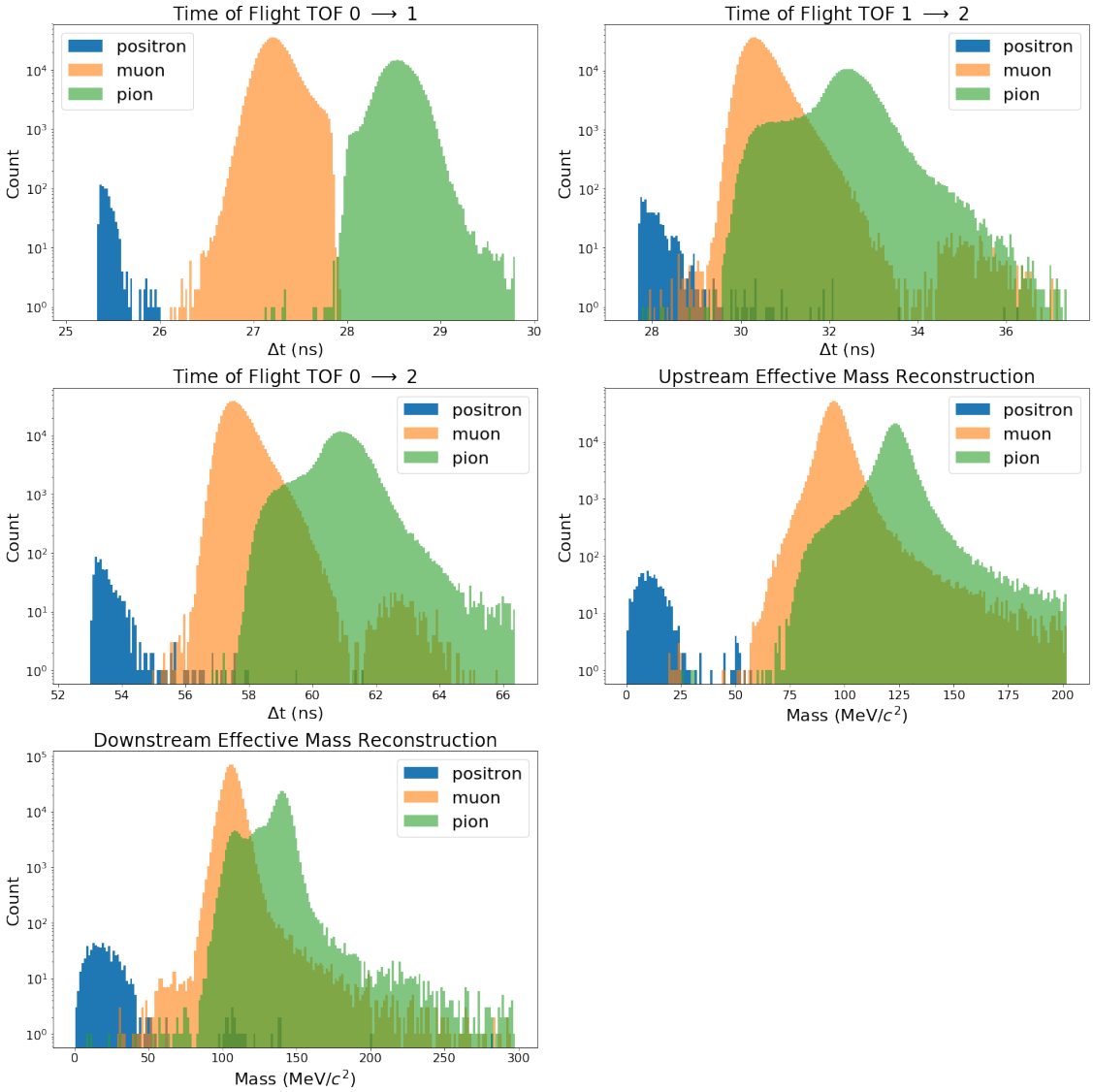
6-240 Beam: PID Feature Set
Simple Cut Only
Time of Flight TOF 0 ⟶ 1
positron
muon
pion
Count
Δt (ns)
Time of Flight TOF 1 ⟶ 2
positron
muon
pion
Count
Δt (ns)
Time of Flight TOF 0 ⟶ 2
positron
muon
pion
Count
Δt (ns)
Upstream Effective Mass Reconstruction
positron
muon
pion
Count
Mass (MeV/c^2)
Downstream Effective Mass Reconstruction
positron
muon
pion
Count
Mass (MeV/c^2)

10-140 Beam: Raw Feature Set
Simple Cut Only

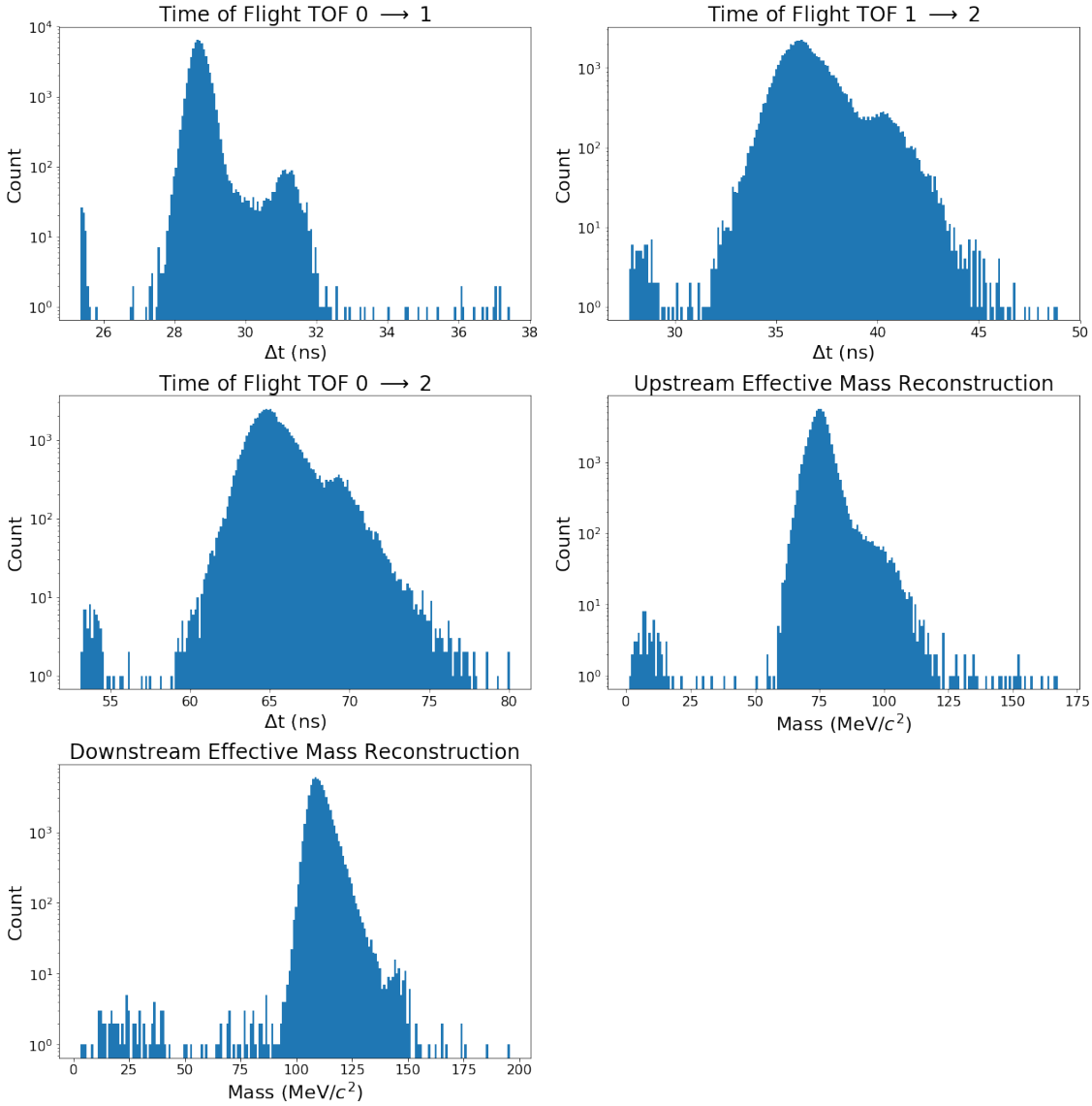

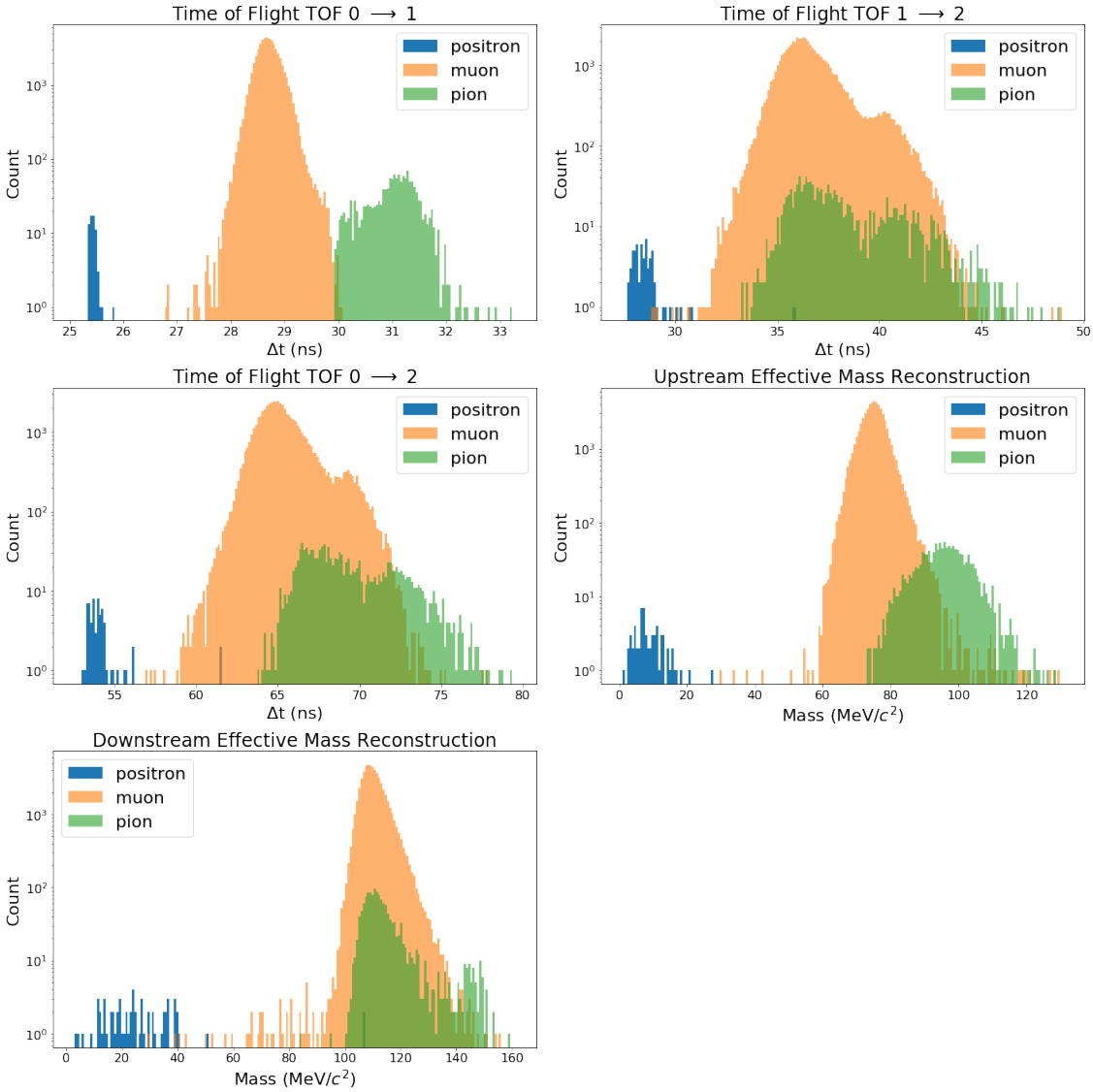
10-140 Beam: PID Feature Set
Simple Cut Only
Time of Flight TOF 0 ⟶ 1
Time of Flight TOF 1 ⟶ 2
Time of Flight TOF 0 ⟶ 2
Upstream Effective Mass Reconstruction
Downstream Effective Mass Reconstruction
positron
muon
pion
Count
Δt (ns)
Mass (MeV/c^2)

10-200 Beam: Raw Feature Set
Simple Cut Only

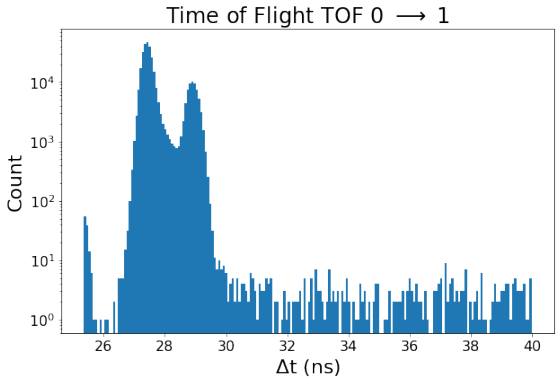

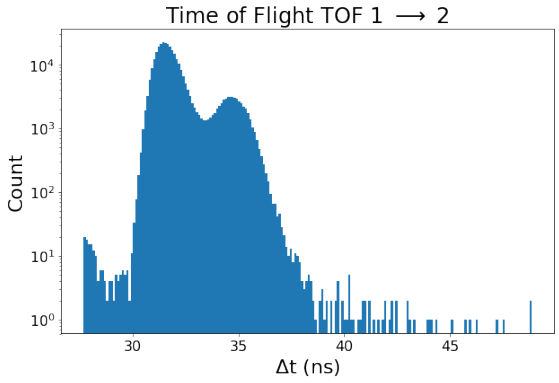

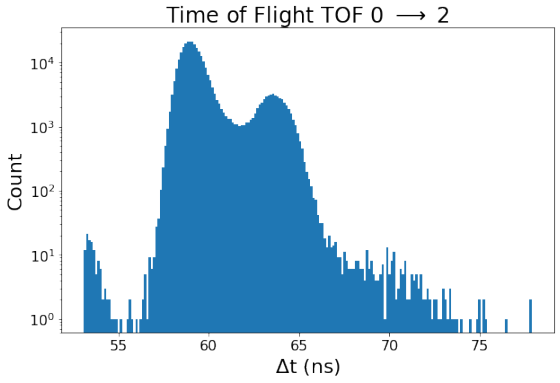

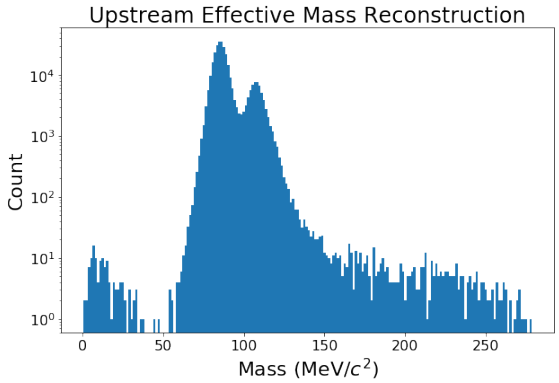

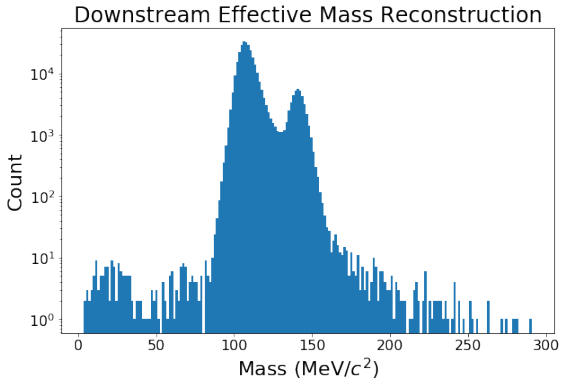

10-200 Beam: PID Feature Set
Simple Cut Only

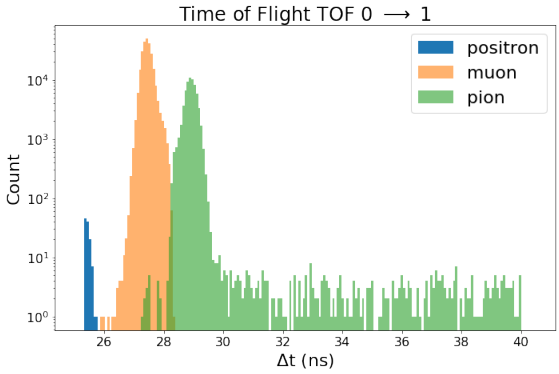

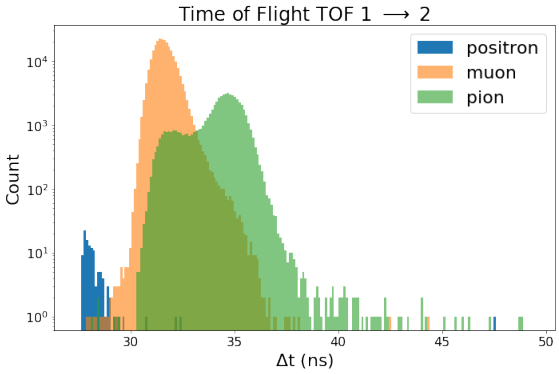

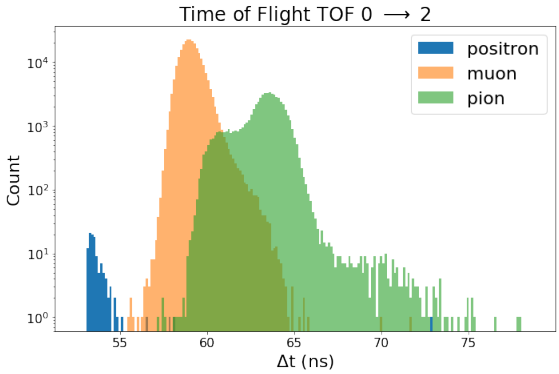

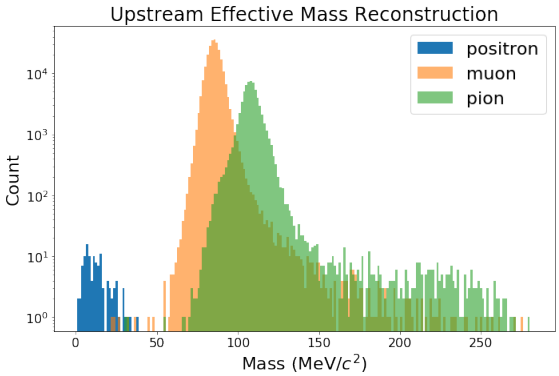

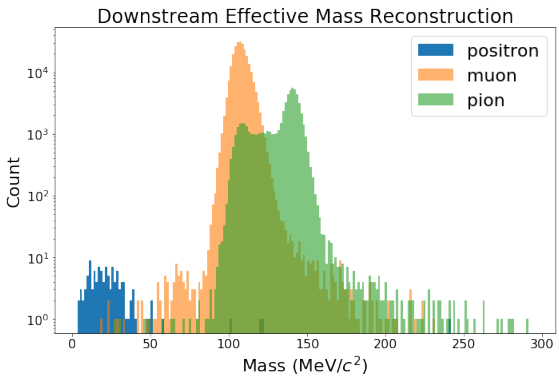

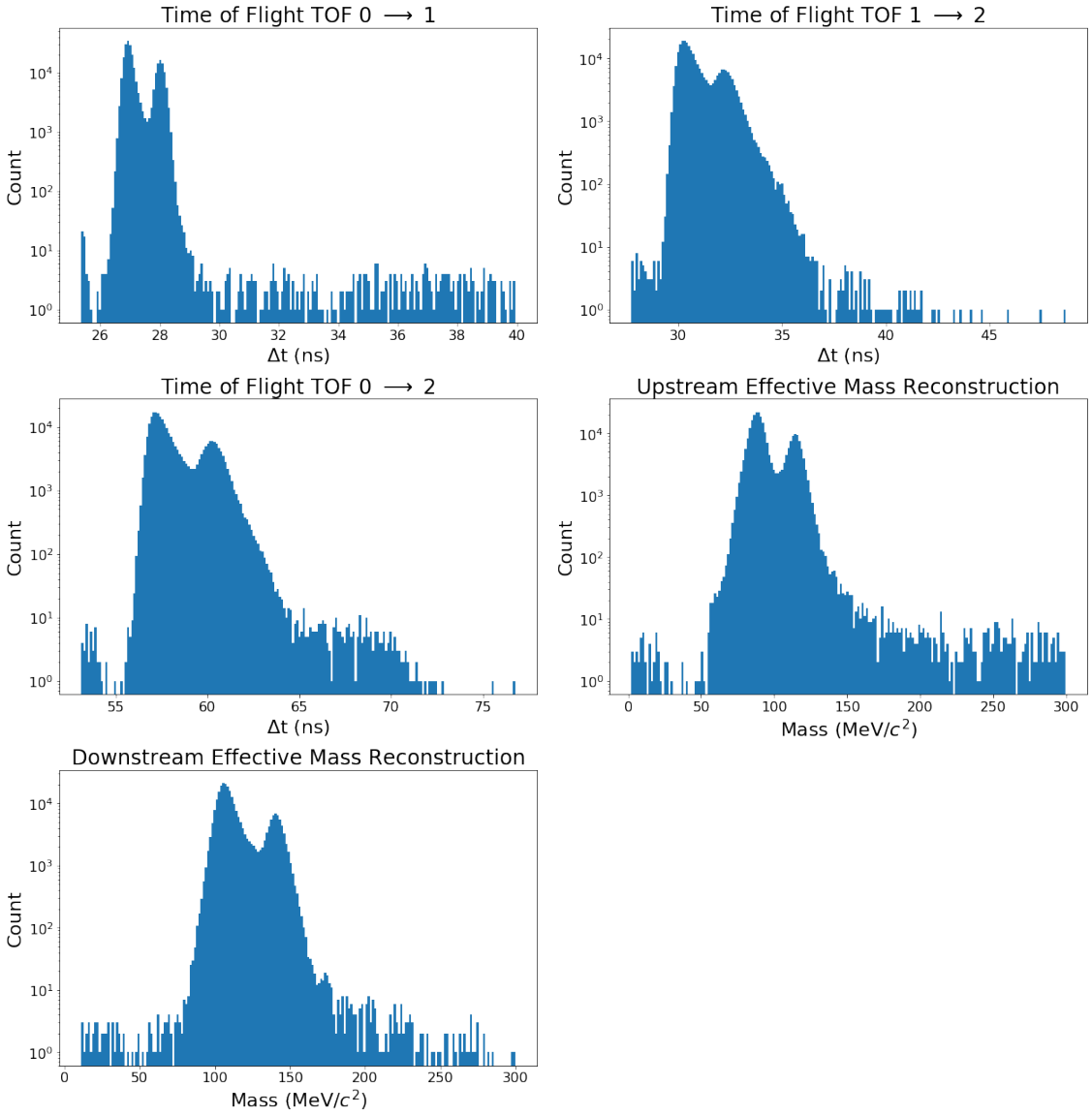
10-240 Beam: Raw Feature Set
Simple Cut Only
Time of Flight TOF 0 ⟶ 1
Count
Δt (ns)
Time of Flight TOF 1 ⟶ 2
Count
Δt (ns)
Time of Flight TOF 0 ⟶ 2
Count
Δt (ns)
Upstream Effective Mass Reconstruction
Count
Mass (MeV/c^2)
Downstream Effective Mass Reconstruction
Count
Mass (MeV/c^2)

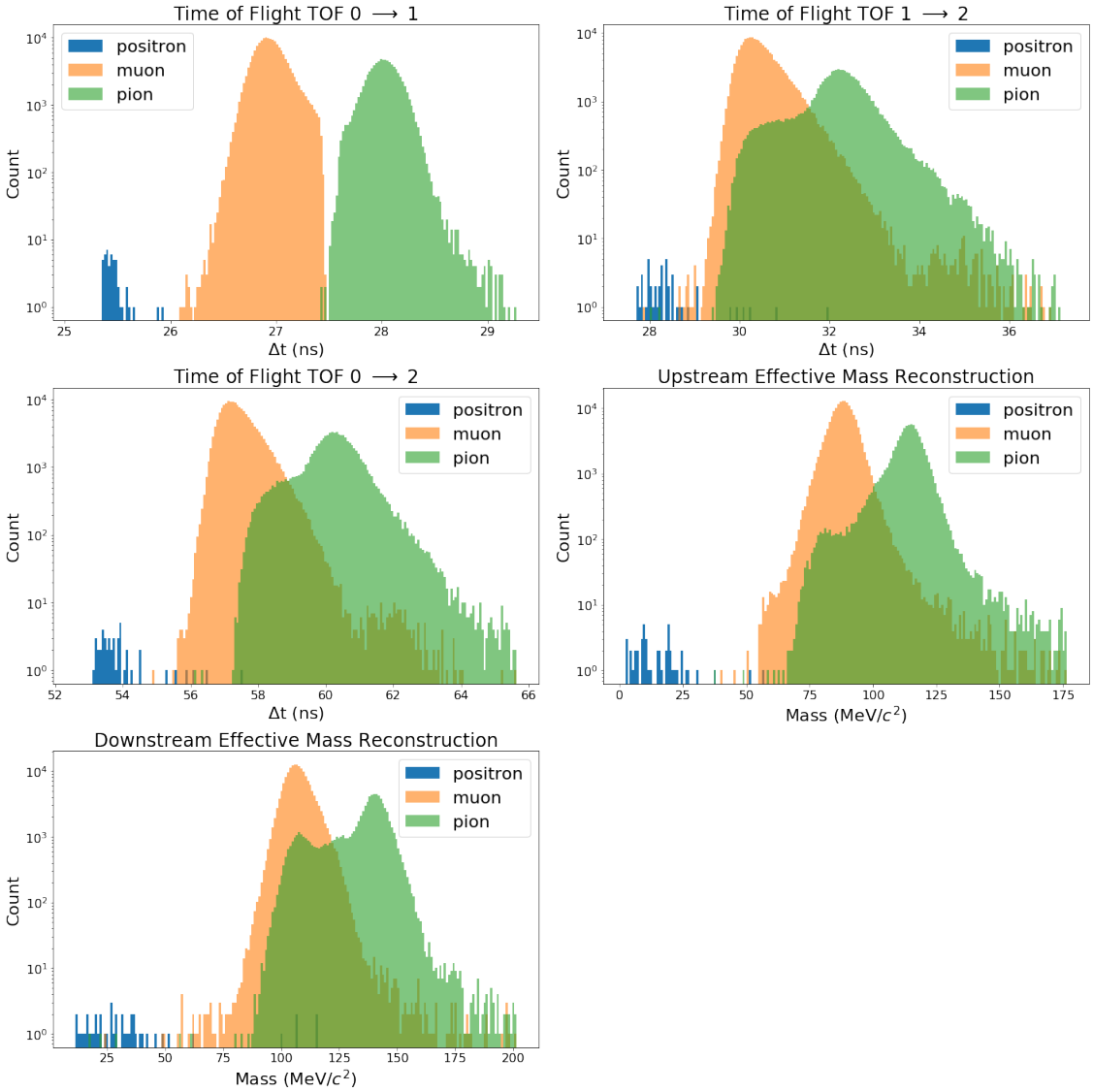
10-240 Beam: PID Feature Set
Simple Cut Only
Time of Flight TOF 0 ⟶ 1
Time of Flight TOF 1 ⟶ 2
Time of Flight TOF 0 ⟶ 2
Upstream Effective Mass Reconstruction
Downstream Effective Mass Reconstruction
positron
muon
pion
Count
Δt (ns)
Mass (MeV/c^2)

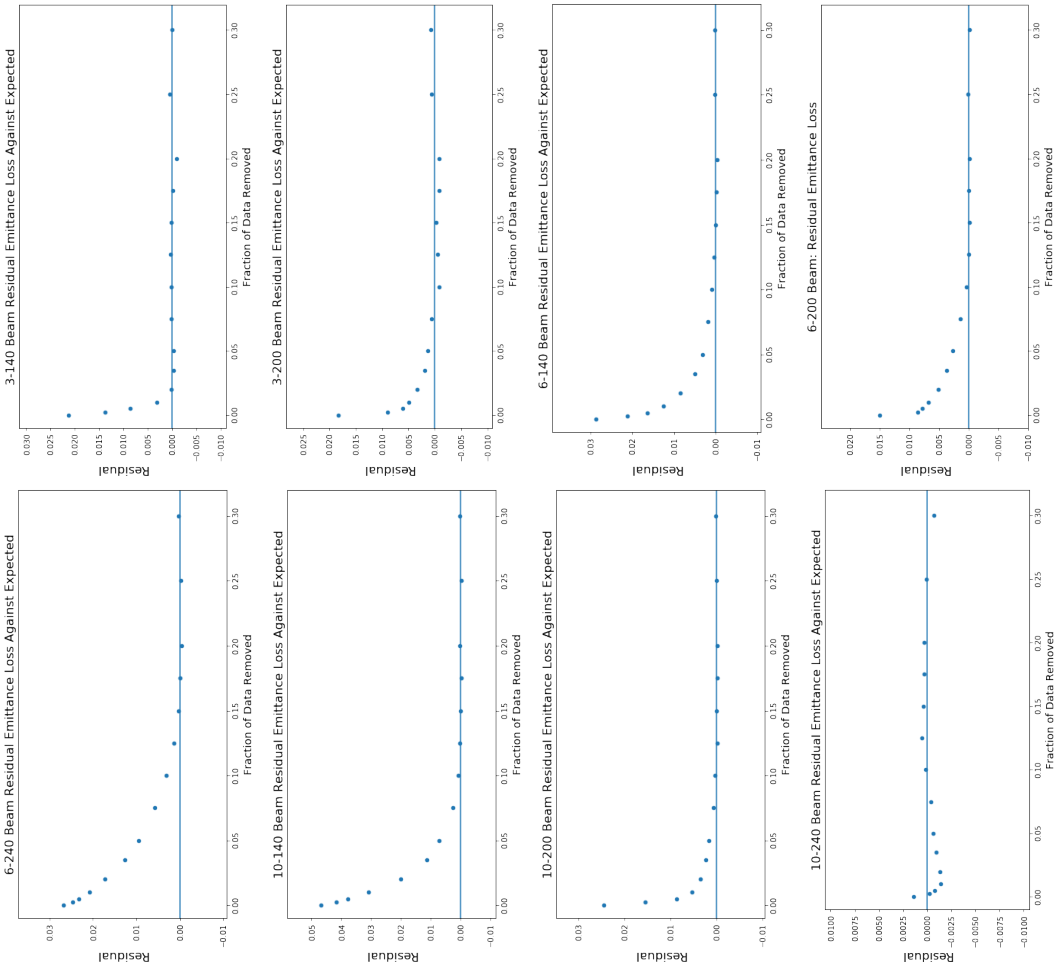

Figure C.1: Residual emittance change across the absorber against best fit line for large emittance cuts plotted as a function of total cut for each beam setting.

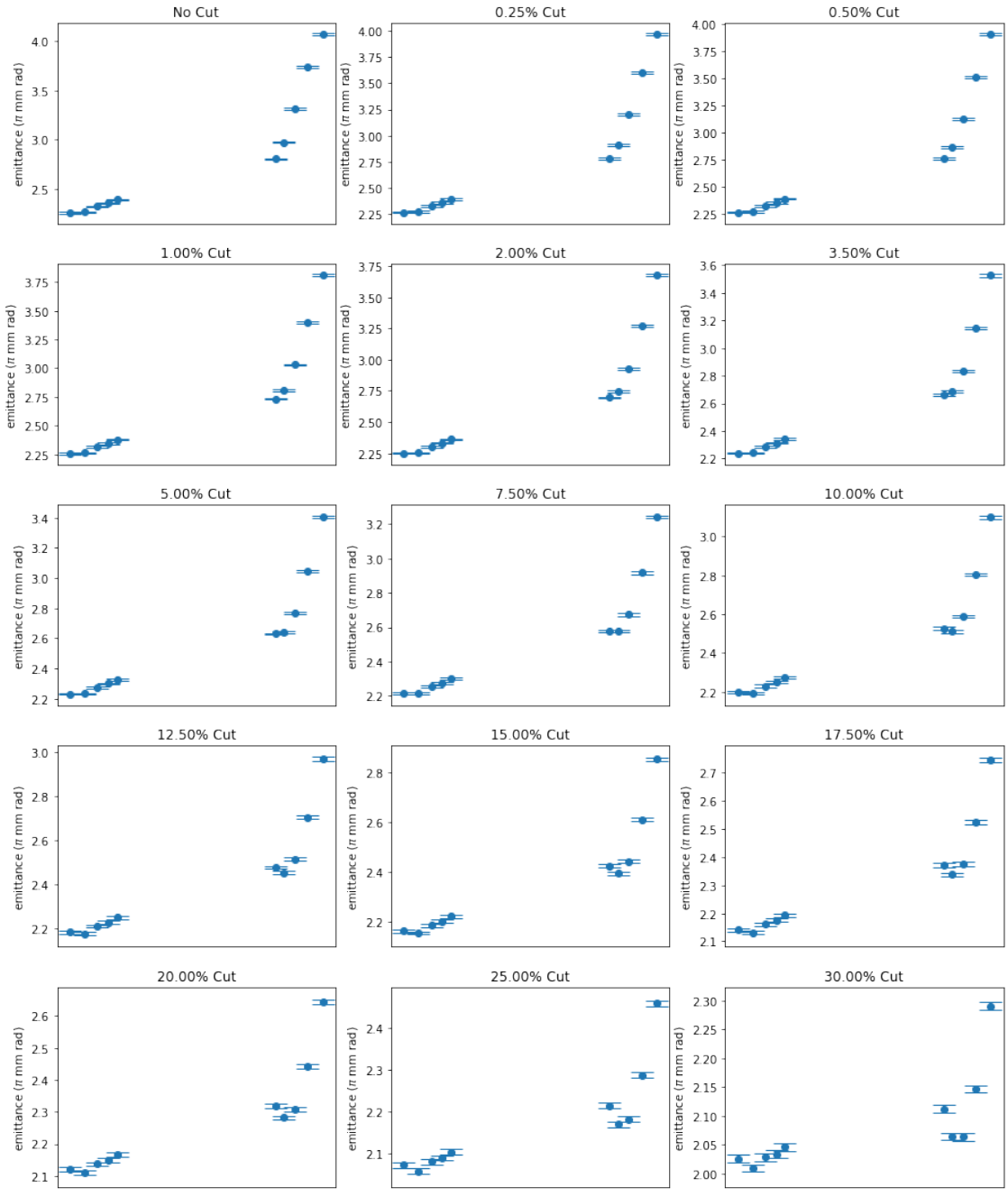
3-140 Beam: Emittance by Elliptical Cut
No Cut
0.25% Cut
0.50% Cut
1.00% Cut
2.00% Cut
3.50% Cut
5.00% Cut
7.50% Cut
10.00% Cut
12.50% Cut
15.00% Cut
17.50% Cut
20.00% Cut
25.00% Cut
30.00% Cut
emittance (π mm rad)

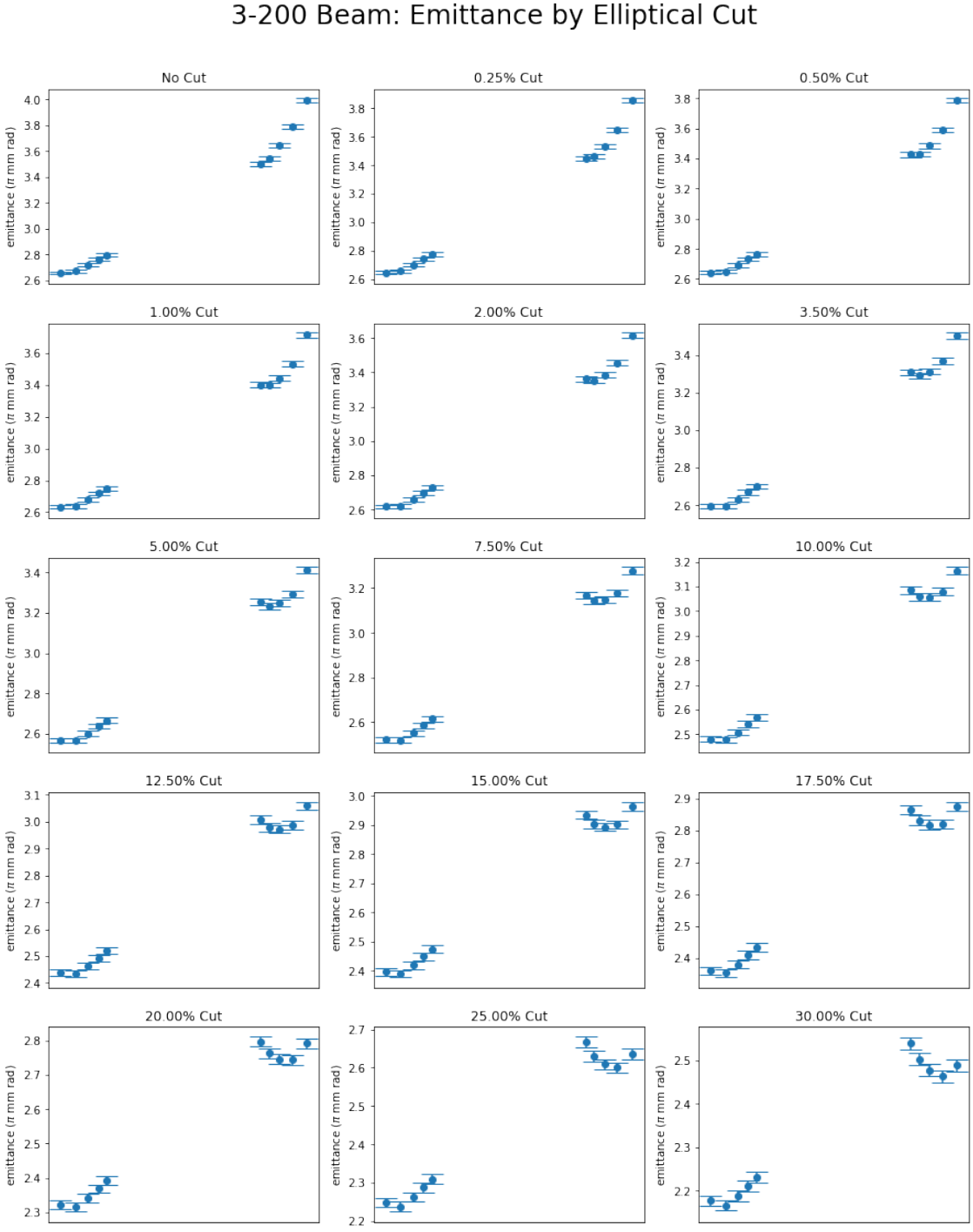
3-200 Beam: Emittance by Elliptical Cut
No Cut
0.25% Cut
0.50% Cut
1.00% Cut
2.00% Cut
3.50% Cut
5.00% Cut
7.50% Cut
10.00% Cut
12.50% Cut
15.00% Cut
17.50% Cut
20.00% Cut
25.00% Cut
30.00% Cut
emittance (π mm rad)

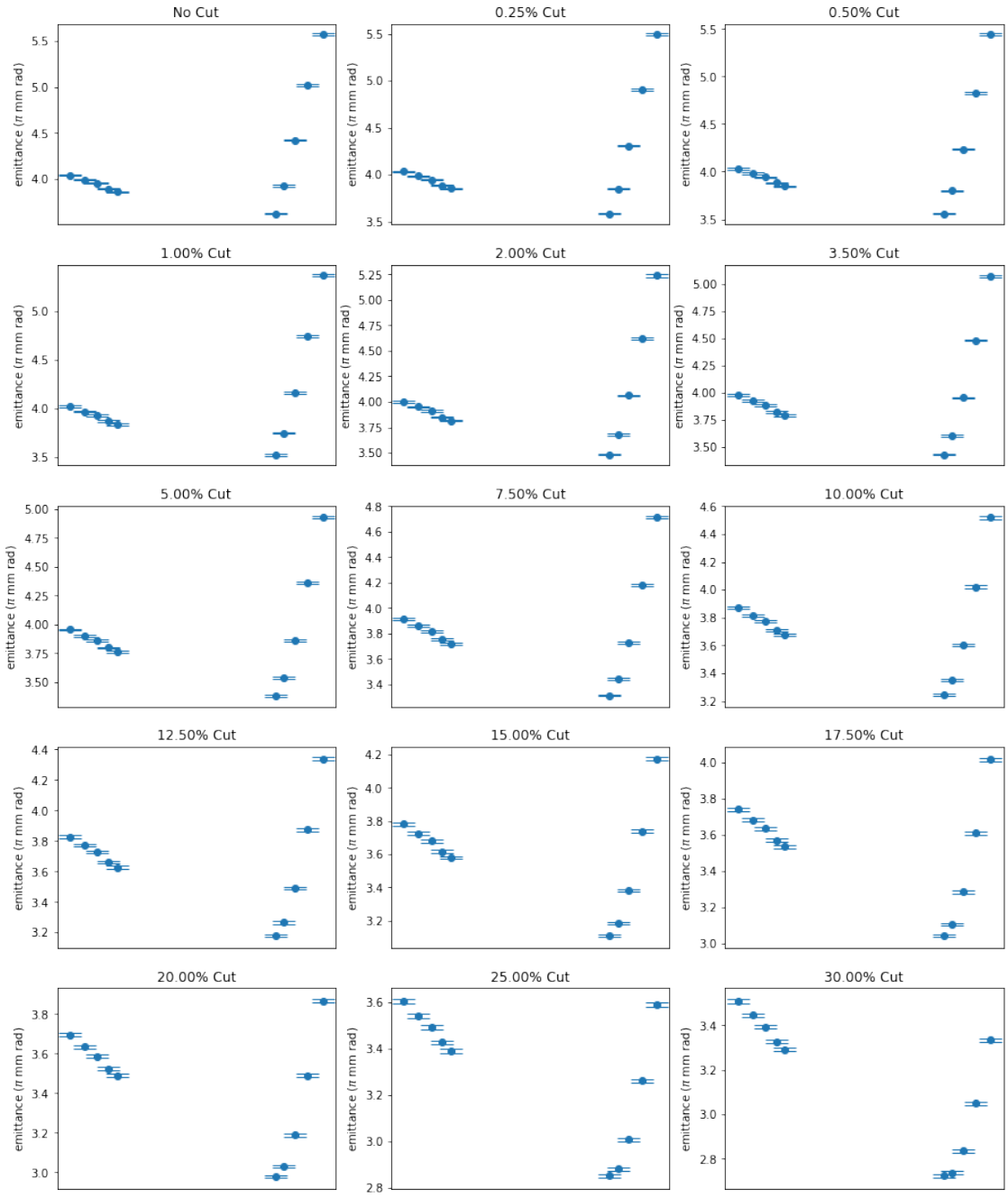
6-140 Beam: Emittance by Elliptical Cut
No Cut
0.25% Cut
0.50% Cut
1.00% Cut
2.00% Cut
3.50% Cut
5.00% Cut
7.50% Cut
10.00% Cut
12.50% Cut
15.00% Cut
17.50% Cut
20.00% Cut
25.00% Cut
30.00% Cut
emittance (π mm rad)

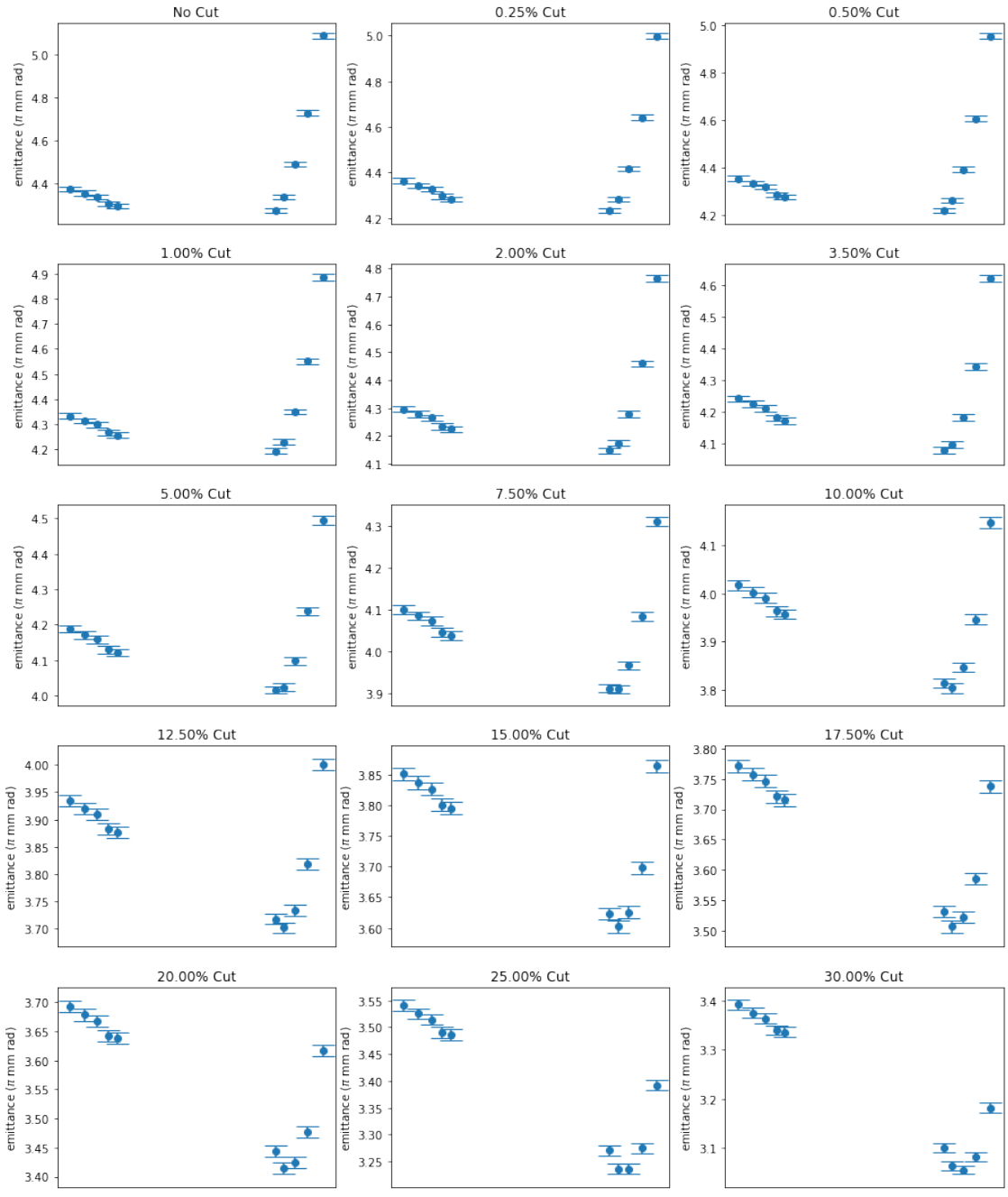
6-200 Beam: Emittance by Elliptical Cut
No Cut
0.25% Cut
0.50% Cut
1.00% Cut
2.00% Cut
3.50% Cut
5.00% Cut
7.50% Cut
10.00% Cut
12.50% Cut
15.00% Cut
17.50% Cut
20.00% Cut
25.00% Cut
30.00% Cut
emittance (π mm rad)

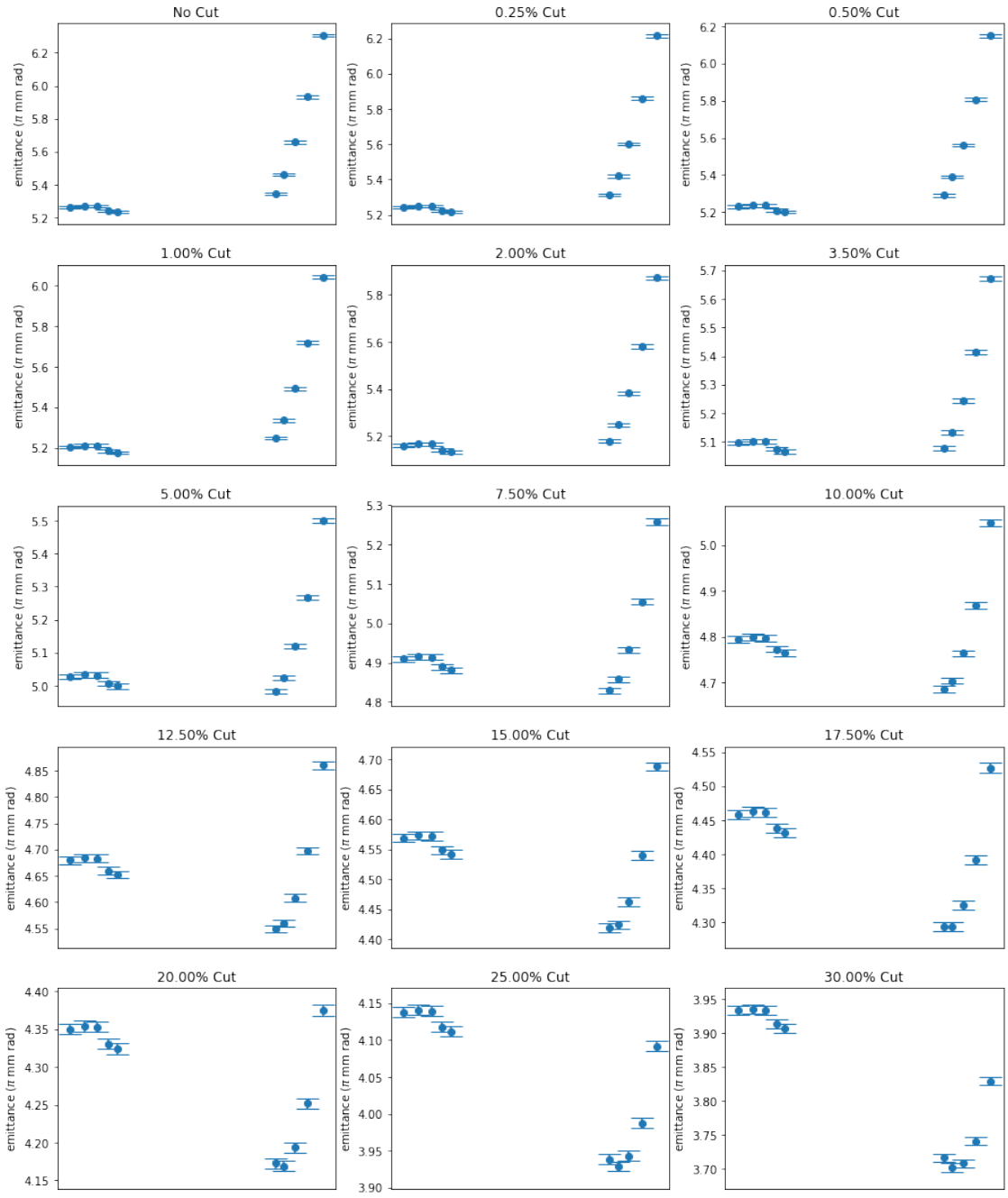
6-240 Beam: Emittance by Elliptical Cut
No Cut
0.25% Cut
0.50% Cut
1.00% Cut
2.00% Cut
3.50% Cut
5.00% Cut
7.50% Cut
10.00% Cut
12.50% Cut
15.00% Cut
17.50% Cut
20.00% Cut
25.00% Cut
30.00% Cut
emittance (π mm rad)

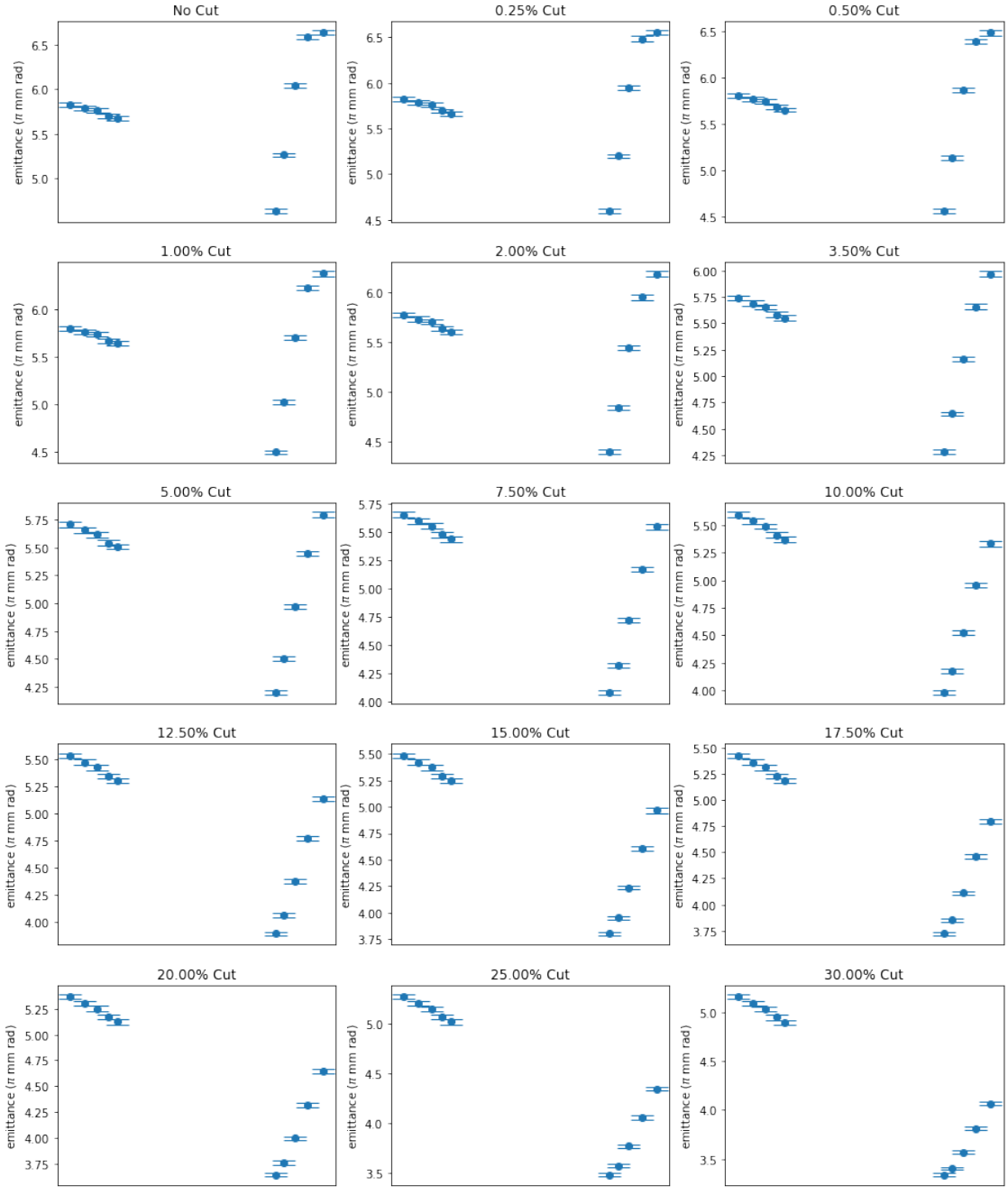
10-140 Beam: Emittance by Elliptical Cut
No Cut
0.25% Cut
0.50% Cut
1.00% Cut
2.00% Cut
3.50% Cut
5.00% Cut
7.50% Cut
10.00% Cut
12.50% Cut
15.00% Cut
17.50% Cut
20.00% Cut
25.00% Cut
30.00% Cut
emittance (π mm rad)

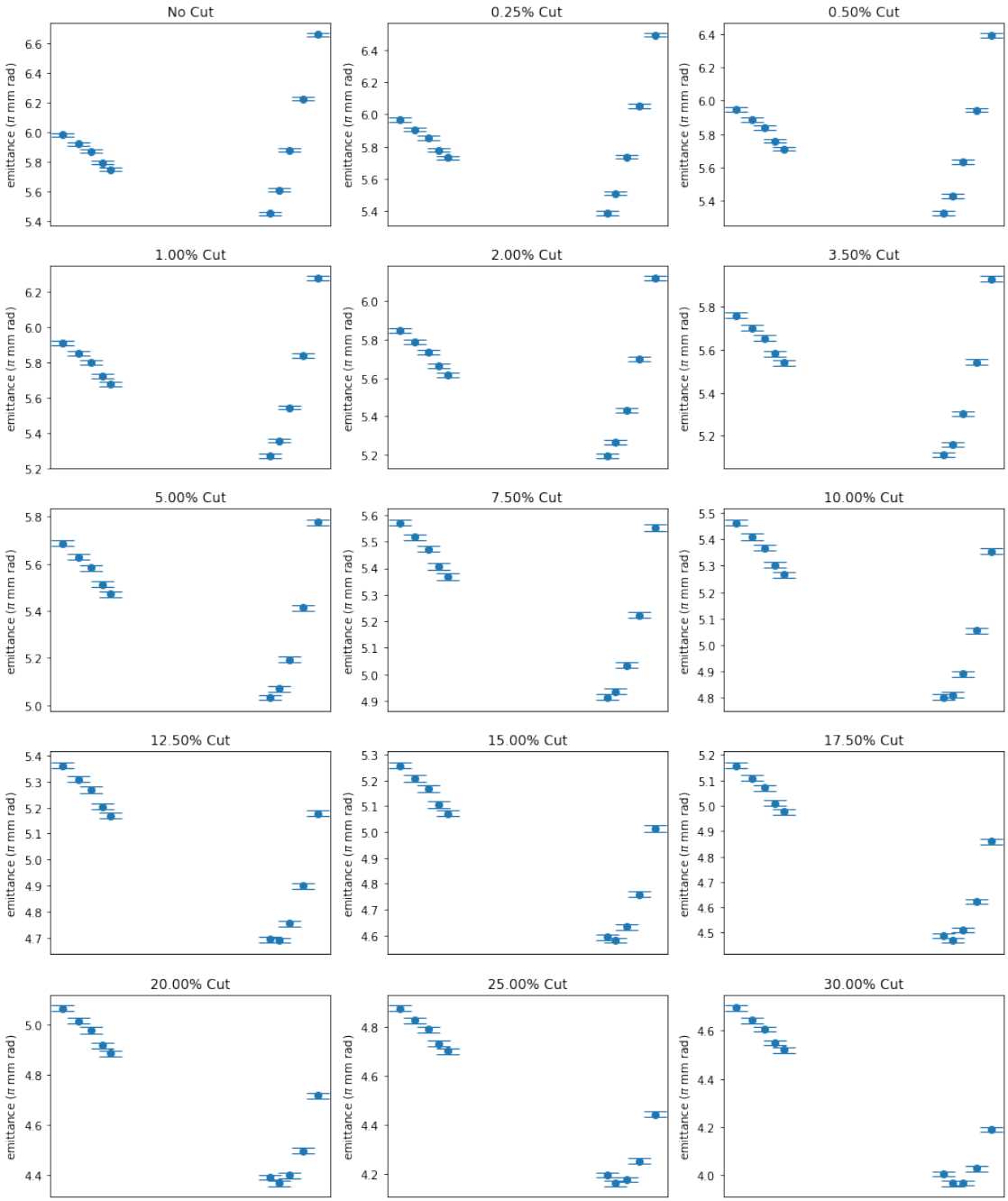
10-200 Beam: Emittance by Elliptical Cut
No Cut
0.25% Cut
0.50% Cut
1.00% Cut
2.00% Cut
3.50% Cut
5.00% Cut
7.50% Cut
10.00% Cut
12.50% Cut
15.00% Cut
17.50% Cut
20.00% Cut
25.00% Cut
30.00% Cut
emittance (π mm rad)

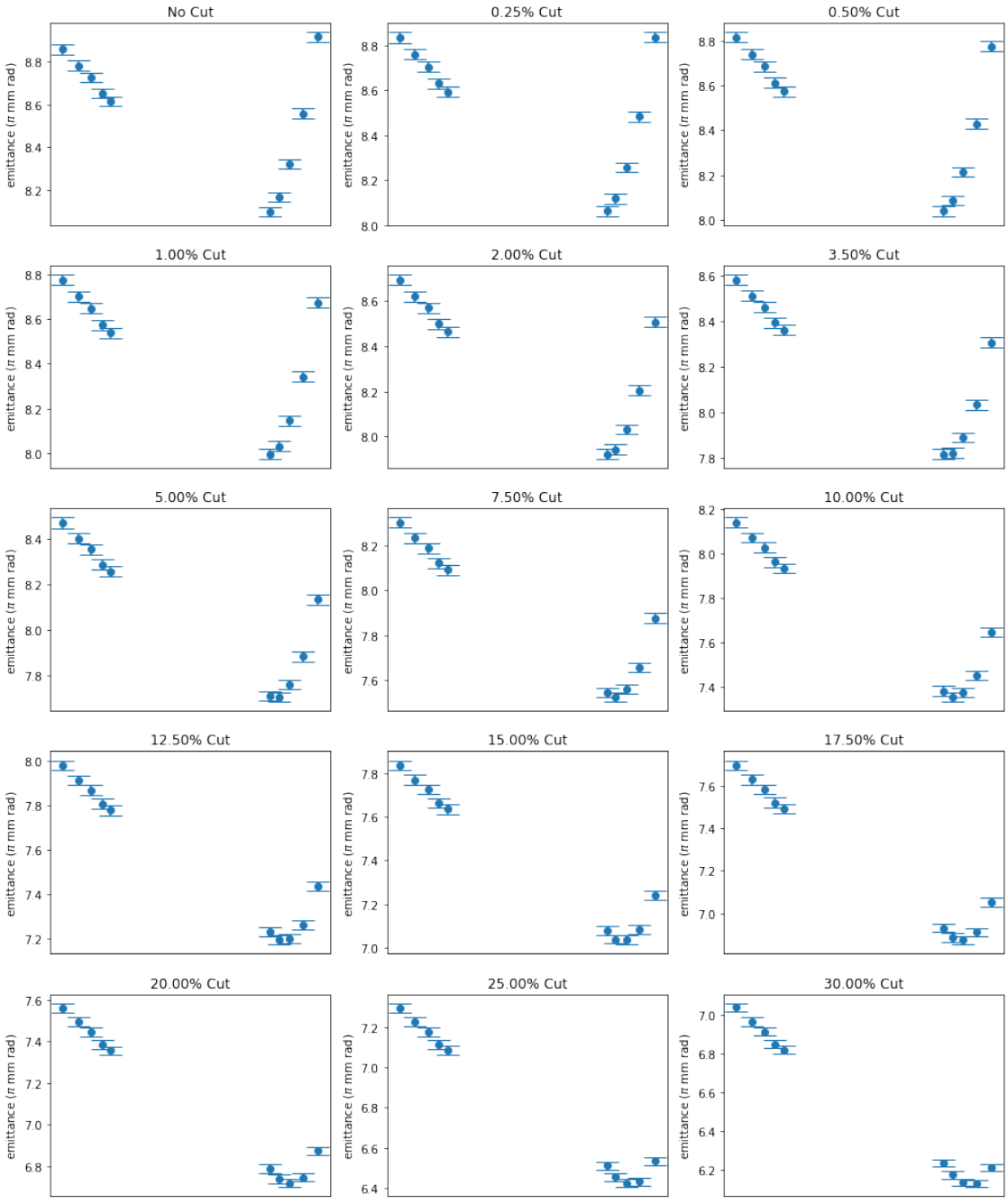
10-240 Beam: Emittance by Elliptical Cut
No Cut
0.25% Cut
0.50% Cut
1.00% Cut
2.00% Cut
3.50% Cut
5.00% Cut
7.50% Cut
10.00% Cut
12.50% Cut
15.00% Cut
17.50% Cut
20.00% Cut
25.00% Cut
30.00% Cut
emittance (π mm rad)

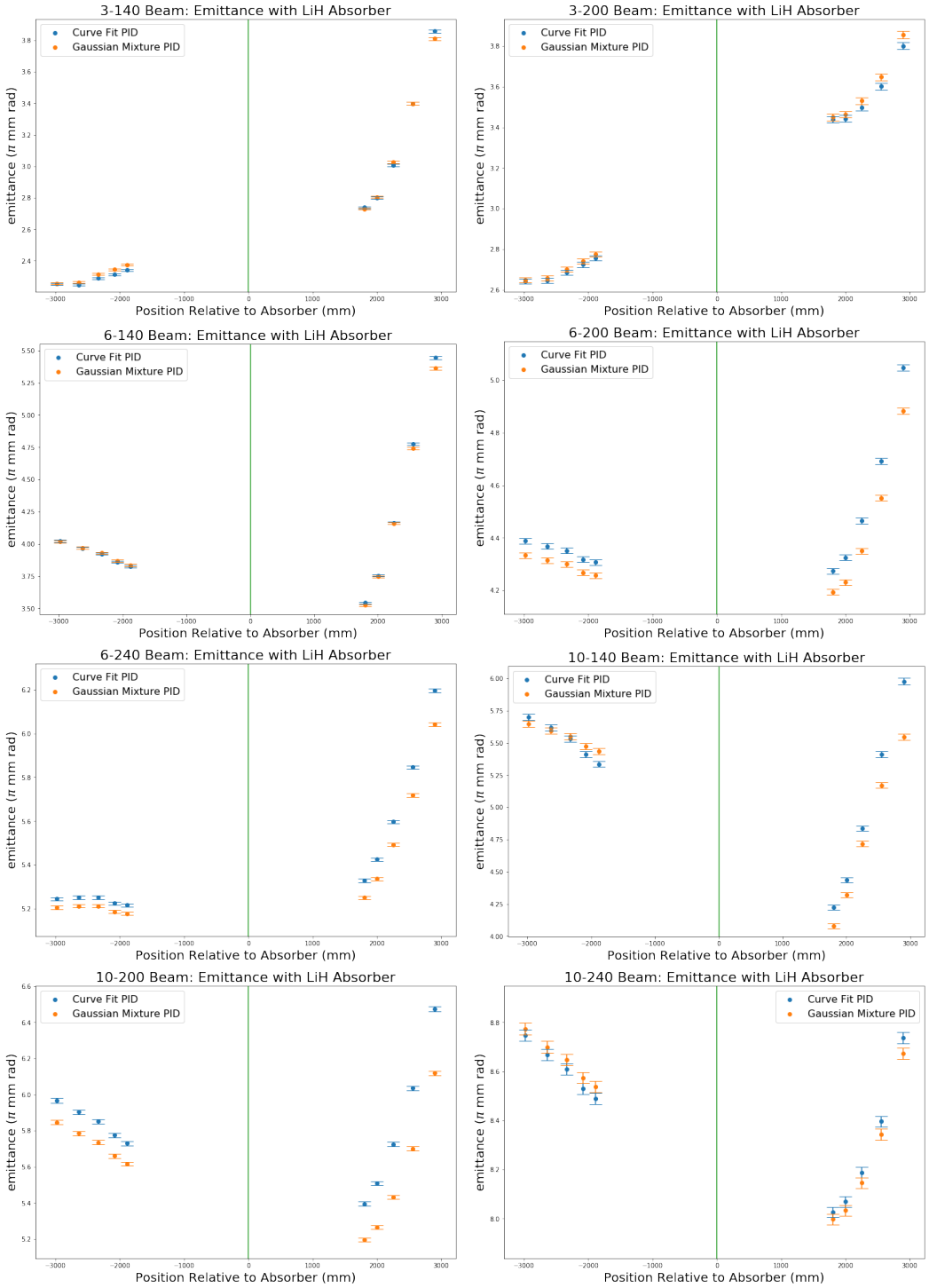

Figure C.2: Emittance measurements for each beam setting. Two PID methods plotted against each other.

Bibliography

[1] G. Rajasekaran, "The Story of the Neutrino," 2016.

[2] F. Reines, C. L. Cowan, F. B. Harrison, A. D. McGuire, and H. W. Kruse, "Detection of the free antineutrino," *Phys. Rev.*, vol. 117, pp. 159–173, Jan 1960.

[3] S. H. Neddermeyer and C. D. Anderson, "Note on the nature of cosmic-ray particles," *Phys. Rev.*, vol. 51, pp. 884–886, May 1937.

[4] G. Danby, J.-M. Gaillard, K. Goulianos, L. M. Lederman, N. Mistry, M. Schwartz, and J. Steinberger, "Observation of high-energy neutrino reactions and the existence of two kinds of neutrinos," *Phys. Rev. Lett.*, vol. 9, pp. 36–44, Jul 1962.

[5] M. L. e. a. Perl, "Evidence for anomalous lepton production in $e^+ - e^-$ annihilation," *Phys. Rev. Lett.*, vol. 35, pp. 1489–1492, Dec 1975.

[6] K. K. at al., "Observation of tau neutrino interactions," *Physics Letters B*, vol. 504, no. 3, pp. 218 – 224, 2001.

[7] M. Goldhaber, L. Grodzins, and A. W. Sunyar, "Helicity of neutrinos," *Phys. Rev.*, vol. 109, pp. 1015–1017, Feb 1958.

[8] R. Davis, D. S. Harmer, and K. C. Hoffman, "Search for neutrinos from the sun," *Phys. Rev. Lett.*, vol. 20, pp. 1205–1209, May 1968.

[9] B. T. Cleveland, T. Daily, J. Raymond Davis, J. R. Distel, K. Lande, C. K. Lee, P. S. Wildenhain, and J. Ullman, "Measurement of the solar electron neutrino flux with the homestake chlorine detector," *The Astrophysical Journal*, vol. 496, no. 1, p. 505, 1998.

[10] Z. Maki, M. Nakagawa, and S. Sakata, "Remarks on the unified model of elementary particles," *Progress of Theoretical Physics*, vol. 28, no. 5, pp. 870–880, 1962.

[11] A. Dobbs, *Particle Rate and Host Accelerator Beam Loss on the MICE Experiment.* PhD thesis, Imperial College London, Nov. 2011.

[12] D. J. Griffiths, *Introduction to elementary particles; 2nd rev. version.* Physics textbook, New York, NY: Wiley, 2008.

[13] Juno Collaboration, "Low energy neutrino physics." `http://www.staff.uni-mainz.de/wurmm/juno.html`.

[14] C. P. et al., "Review of Particle Physics," *Chin. Phys.*, vol. C40, p. 100001, 2016.

[15] F. Capozzi, E. Lisi, A. Marrone, D. Montanino, and A. Palazzo, "Neutrino masses and mixings: Status of known and unknown 3ν parameters," *Nucl. Phys.*, vol. B908, pp. 218–234, 2016.

[16] T. Nakaya and R. K. Plunkett, "Neutrino oscillations with the minos, minos+, t2k, and nova experiments," *New Journal of Physics*, vol. 18, no. 1, p. 015009, 2016.

[17] D. W. Schmitz, "Viewpoint: Hunting the sterile neutrino," *Physics*, vol. 94, Aug 2016.

[18] B. A. Dobrescu and C. T. Hill, "Electroweak symmetry breaking via a top condensation seesaw mechanism," *Phys. Rev. Lett.*, vol. 81, pp. 2634–2637, Sep 1998.

[19] M. G. Aartsen *et al.*, "Searches for Sterile Neutrinos with the IceCube Detector," *Phys. Rev. Lett.*, vol. 117, no. 7, p. 071801, 2016.

[20] W. Commons, "Feynman diagram of double beta decay," January 2009.

[21] S. Dell'Oro, S. Marcocci, M. Viel, and F. Vissani, "Neutrinoless double beta decay: 2015 review," *Adv. High Energy Phys.*, vol. 2016, p. 2162659, 2016.

[22] S. M. Bilenky and C. Giunti, "Neutrinoless double-beta decay: A probe of physics beyond the standard model," *International Journal of Modern Physics A*, vol. 30, no. 04n05, p. 1530001, 2015.

[23] S. Dell'Oro, S. Marcocci, M. Viel, and F. Vissani, "Neutrinoless double beta decay: 2015 review," *Adv. High Energy Phys.*, vol. 2016, p. 2162659, 2016.

[24] R. Henning, "Current status of neutrinoless double-beta decay searches," *Reviews in Physics*, vol. 1, no. Supplement C, pp. 29 – 35, 2016.

[25] S. Abe *et al.*, "Precision Measurement of Neutrino Oscillation Parameters with KamLAND," *Phys. Rev. Lett.*, vol. 100, p. 221803, 2008.

[26] The T2K Collaboration, "About t2k." `http://t2k-experiment.org/t2k/`, 2013.

[27] J. Cao and K.-B. Luk, "An overview of the Daya Bay Reactor Neutrino Experiment," *Nucl. Phys.*, vol. B908, pp. 62–73, 2016.

[28] F. P. An *et al.*, "A side-by-side comparison of Daya Bay antineutrino detectors," *Nucl. Instrum. Meth.*, vol. A685, pp. 78–97, 2012.

[29] P. Adamson *et al.*, "Constraints on Oscillation Parameters from ν_e Appearance and ν_μ Disappearance in NOvA," *Phys. Rev. Lett.*, vol. 118, no. 23, p. 231801, 2017.

[30] S. K. Agarwalla, S. Prakash, and W. Wang, "High-precision measurement of atmospheric mass-squared splitting with T2K and NOvA," 2013.

[31] D. M. Kaplan, "Muon Colliders and Neutrino Factories," *EPJ Web Conf.*, vol. 95, p. 03019, 2015.

[32] S. Ozaki, R. Palmer, M. Zisman, and J. Gallardo, "Feasibility Study-II of a Muon-Based Neutrino Source," *BNL-52623*, 2001.

[33] A. Letchford, M. Clarke-Gayther, D. Faircloth, S. Lawrie, *et al.*, "Status of the ral front end test stand,"

[34] K. T. McDonald, J. Lettry, I. Efthymiopoulos, A. Fabich, V. B. Graves, T. Tsang, P. Loveridge, P. T. Spampinato, O. Caretta, H. Park, *et al.*, "The merit high-power target experiment at the cern ps," in *Conf. Proc.*, vol. 90504, pp. 795–799, 2009.

[35] H.-J. Cai, G. Yang, N. Vassilopoulos, S. Zhang, F. Fu, Y. Yuan, and L. Yang, "New target solution for a muon collider or a muon-decay neutrino beam facility: The granular waterfall target," *Phys. Rev. Accel. Beams*, vol. 20, p. 023401, Feb 2017.

[36] S. Machida *et al.*, "Acceleration in the Linear Non-Scaling Fixed-Field Alternating-Gradient Accelerator EMMA," *Nature Phys.*, vol. 8, pp. 243–247, 2012.

[37] E. Wilsom, *An Introduction to Particle Accelerators*. The address: Oxford, 2001. An optional note.

[38] B. J. Holzer, "Beam optics and lattice design for particle accelerators," 2013. [Landolt-Bornstein21C,119(2013)].

[39] C. Rogers, "Definitions and methods used for the determination of the beam optical functions and emittances," *MICE Note 465*, Oct. 2015.

[40] J. Marriner, "Stochastic cooling overview," *Nuclear Instruments and Methods in Physics Research Section A: Accelerators, Spectrometers, Detectors and Associated Equipment*, vol. 532, no. 1, pp. 11 – 18, 2004. International Workshop on Beam Cooling and Related Topics.

[41] R. C. Fernow and J. C. Gallardo, "Muon transverse ionization cooling: Stochastic approach," *Phys. Rev. E*, vol. 52, pp. 1039–1042, Jul 1995.

[42] Science and Technology Facilities Council, "How isis works - in depth." `https://www.isis.stfc.ac.uk/Pages/How-ISIS-works--in-depth.aspx`.

[43] C. N. Booth, P. Hodgson, L. Howlett, R. Nicholson, E. Overton, M. Robinson, P. J. Smith, M. Apollonio, G. Barber, A. Dobbs, J. Leaver, K. R. Long, B. Shepherd, D. Adams, E. Capocci, E. McCarron, and J. Tarrant, "The design, construction and performance of the mice target," *Journal of Instrumentation*, vol. 8, no. 03, p. P03006, 2013.

[44] M. Bogomilov *et al.*, "The MICE Muon Beam on ISIS and the beam-line instrumentation of the Muon Ionization Cooling Experiment," *JINST*, vol. 7, p. P05009, 2012.

[45] M. Leonova, "Mice spectrometer solenoid magnetic field measurements," *MICE Note 414*, Jun. 2013.

[46] U. Bravar *et al.*, "MICE: the Muon Ionization Cooling Experiment. Step I: First Measurement of Emittance with Particle Physics Detectors," in *Particles and fields. Proceedings, Meeting of the Division of the American Physical Society, DPF 2011, Providence, USA, August 9-13, 2011*, 2011.

[47] D. Adams *et al.*, "Electron-Muon Ranger: performance in the MICE Muon Beam," *JINST*, vol. 10, no. 12, p. P12012, 2015.

[48] e. a. M. Ellis, "The design, construction and performance of the mice scintillating fibre trackers," *Nuclear Instruments and Methods in Physics Research Section A: Accelerators, Spectrometers, Detectors and Associated Equipment*, vol. 659, no. 1, pp. 136 – 153, 2011.

[49] C. Tunnell and C. Rogers, "Maus: Mice analysis user software.," in *Proc. Int. Particle Accelerator Conf.*, (San Sebastian, Spain), 2011.

[50] J. Dean and S. Ghemawat, "Mapreduce: Simplified data processing on large clusters," in *Proceedings of the 6th Conference on Symposium on Opearting Systems Design & Implementation - Volume 6*, OSDI'04, (Berkeley, CA, USA), pp. 10–10, USENIX Association, 2004.

[51] R. Brun and F. Rademakers, "ROOT An object oriented data analysis framework," *Nuclear Instruments and Methods in Physics Research A*, vol. 389, pp. 81–86, Feb. 1997.

[52] A. Dobbs, C. Hunt, K. Long, E. Santos, M. A. Uchida, P. Kyberd, C. Heidt, S. Blot, and E. Overton, "The reconstruction software for the MICE scintillating fibre trackers," *JINST*, vol. 11, no. 12, p. T12001, 2016.

[53] MAUS Software Group, *MAUS Analysis User System User Guide*. MICE Collaboration.

[54] S. A. et al., "Geant4a simulation toolkit," *Nuclear Instruments and Methods in Physics Research Section A: Accelerators, Spectrometers, Detectors and Associated Equipment*, vol. 506, no. 3, pp. 250 – 303, 2003.

[55] R. Frhwirth, "Application of kalman filtering to track and vertex fitting," *Nuclear Instruments and Methods in Physics Research Section A: Accelerators, Spectrometers, Detectors and Associated Equipment*, vol. 262, no. 2, pp. 444 – 450, 1987.

[56] P. Billoir, "Track fitting with multiple scattering: A new method," *Nuclear Instruments and Methods in Physics Research*, vol. 225, no. 2, pp. 352 – 366, 1984.

[57] F. Pedregosa, G. Varoquaux, A. Gramfort, V. Michel, B. Thirion, O. Grisel, M. Blondel, P. Prettenhofer, R. Weiss, V. Dubourg, J. Vanderplas, A. Passos, D. Cournapeau, M. Brucher, M. Perrot, and E. Duchesnay, "Scikit-learn: Machine learning in Python," *Journal of Machine Learning Research*, vol. 12, pp. 2825–2830, 2011.

[58] J. H. Cobb, "Statistical errors on emittance and optical functions," *MICE Note 341*, Apr. 2011.

[59] T. D. Lee and C. N. Yang, "Question of parity conservation in weak interactions," *Phys. Rev.*, vol. 104, pp. 254–258, Oct 1956.